

**Diffusion Weighted Magnetic Resonance Imaging Assessment
of Blood Flow in the Microvasculature of Abdominal Organs**

by

Loredana Sorina Truica

M Sc (University of Bucharest) 2001

A thesis submitted to the
Faculty of Graduate Studies and Postdoctoral Affairs
in partial fulfillment of the requirements
for the degree of
Doctor of Philosophy
(Physics)

Ottawa-Carleton Institute for Physics

Department of Physics

Carleton University

January, 2011

© 2011, Loredana Sorina Truica



Library and Archives
Canada

Published Heritage
Branch

395 Wellington Street
Ottawa ON K1A 0N4
Canada

Bibliothèque et
Archives Canada

Direction du
Patrimoine de l'édition

395, rue Wellington
Ottawa ON K1A 0N4
Canada

Your file *Votre référence*
ISBN 978-0-494-79622-1
Our file *Notre référence*
ISBN 978-0-494-79622-1

NOTICE

The author has granted a non-exclusive license allowing Library and Archives Canada to reproduce, publish, archive, preserve, conserve, communicate to the public by telecommunication or on the Internet, loan, distribute and sell theses worldwide, for commercial or non-commercial purposes, in microform, paper, electronic and/or any other formats

The author retains copyright ownership and moral rights in this thesis. Neither the thesis nor substantial extracts from it may be printed or otherwise reproduced without the author's permission.

In compliance with the Canadian Privacy Act some supporting forms may have been removed from this thesis.

While these forms may be included in the document page count, their removal does not represent any loss of content from the thesis.

AVIS

L'auteur a accordé une licence non exclusive permettant à la Bibliothèque et Archives Canada de reproduire, publier, archiver, sauvegarder, conserver, transmettre au public par télécommunication ou par l'Internet, prêter, distribuer et vendre des thèses partout dans le monde, à des fins commerciales ou autres, sur support microforme, papier, électronique et/ou autres formats.

L'auteur conserve la propriété du droit d'auteur et des droits moraux qui protègent cette thèse. Ni la thèse ni des extraits substantiels de celle-ci ne doivent être imprimés ou autrement reproduits sans son autorisation.

Conformément à la loi canadienne sur la protection de la vie privée, quelques formulaires secondaires ont été enlevés de cette thèse.

Bien que ces formulaires aient inclus dans la pagination, il n'y aura aucun contenu manquant.

■+■
Canada

Abstract

In this thesis, water diffusion in human liver and placenta is studied using diffusion weighted magnetic resonance imaging. For short, randomly oriented vascular segments, intravascular water motion is diffusion-like. For tissues with large vascular compartments the diffusion decay is bi-exponential with one component corresponding to diffusing water and the other to water in the microvasculature. This model, known as the intravoxel incoherent motion (IVIM) model, is seldom used with abdominal organs because of motion artifacts. This limitation was overcome for the experiments reported here by introducing 1) parallel imaging, 2) navigator echo respiratory triggering (NRT), 3) a double echo diffusion sequence that inherently compensates for eddy current effects, 4) SPAIR fat suppression and 5) a superior approach to image analysis. In particular, the use of NRT allowed us to use a free breathing protocol instead of the previously required breath hold protocol. The resulting DWI images were of high quality and motion artifact free. Diffusion decays were measured over a larger portion of the decay than had previously been reported and the results are considerably better than those previously reported.

For both studies, reliable measurements of the diffusion coefficient (D), pseudo-diffusion coefficient (D^*) and perfusion fraction (f), were obtained using a region of

interest analysis as well as a pixel-by-pixel approach. To within experimental error, all patients had the same values of D ($1.10 \mu\text{m}^2/\text{ms} \pm 0.16 \mu\text{m}^2/\text{ms}$), D^* ($46 \mu\text{m}^2/\text{ms} \pm 17 \mu\text{m}^2/\text{ms}$) and f ($44.0\% \pm 6.9\%$) in liver and D ($1.8 \mu\text{m}^2/\text{ms} \pm 0.2 \mu\text{m}^2/\text{ms}$), D^* ($30 \mu\text{m}^2/\text{ms} \pm 12 \mu\text{m}^2/\text{ms}$), and f ($40\% \pm 6\%$) in the placenta. No dependence on gestational age was found for the placental study. Parametric maps of f and D^* were consistent with blood flow patterns in both systems. The model worked well for both investigated organs even though their anatomical structures are quite different.

A method for removing rectified noise bias from low intensity magnitude MR images measured with phased array coils is also presented. This algorithm has significance for diffusion decay measurements since it permits the use of low intensity data points which could, for example, allow the acquisition of high resolution parametric maps.

Acknowledgements

I would like to express my sincere gratitude to my supervisor, Dr Ian Cameron for the guidance and constant support provided throughout the course of this work. This thesis would not appear in its present form without his kind assistance and valuable suggestions. I would like to thank my professors at Carleton University for sharing their knowledge and especially professor Paul Johns for great teaching, guidance and support.

I'm grateful to all members of the Diagnostic Imaging – Magnetic Resonance Lab. I had the pleasure to know and work with Ian Cameron, Greg Cron, Claire Footitt, Elena Olariu, Fakhreh Mirrashed, Andra Smith and Ewan Hill. They were not only colleagues, they were “a great family” as well.

I would like to acknowledge Drs Andre Gruslin, Len Avruch and Felipe Moretti for their valuable input and assistance in the Placenta project. In particular, I would like to thank the technologists for their help in the acquisition of the data and the gentle and attentive handling of the volunteers involved in the above mentioned project. I would also like to thank all the volunteers from the liver study.

My parents, mama Anitza and my sister have shown me unconditional love and support and whispered guidance throughout the years of my life. I love, miss and thank

them from my heart My gratitude and warm thoughts go towards all my friends around this blue planet Especially Corina, Marius and Cristina, an invisible and constant presence, thank you for an additional “proof” that time and distance are relative

To my closest friends here, Mihai, Maria and Elena and my adopted “family” Miriam and Jonathan, great thanks for their love, support and wonderful memories together

Heartfelt thanks go to much missed, Ticu and Nenea Nicu for being “my other parents” and to Nic for showing me the way to dreams and life Their presence from somewhere between the stars has been always felt

Thank you all

Table of Contents

Abstract	ii
Acknowledgements	iv
Table of Contents	vi
List of Tables	xi
List of Figures	xiii
List of Abbreviations	xviii
1. Introduction	1
1 1 Historical Introduction	2
1 2 Introduction to Diffusion in Magnetic Resonance	2
1 2 1 Intravoxel Incoherent Motion	6
1 3 Abdominal Imaging Literature Review	7
1 3 1 IVIM Perfusion versus Classical Perfusion	9
1 4 Thesis Outline	10

2. Theory and Background	13
2 1 Introduction	14
2 2 Principles of Nuclear Magnetic Resonance	14
2 2 1 The Nuclear Magnetic Moment in a Static Magnetic Field	14
2 2 2 Nuclear Spin Energy Level Population in a Static Magnetic Field	17
2 2 3 Effect of RF Pulses and Magnetic Field Gradients on M	19
2 2 4 The Bloch Equations and Relaxation	20
2 3 Diffusion	25
2 3 1 Diffusion Theory	25
2 3 1 1 Fick's law and Einstein's equation	25
2 3 1 2 Diffusion and NMR	27
2 3 1 3 Eddy Currents	32
2 3 1 4 Equations governing the diffusive transport of magnetization	34
2 3 2 Apparent Diffusion in Biological Tissues	36
2 3 3 Intravoxel Incoherent Motion Imaging	38
2 3 3 1 Intravoxel Motion and MR Imaging	38
2 4 Motion Tracking with Prospective Acquisition Correction (PACE)	45
2 5 Human Placenta	49
2 5 1 Placenta Development	50
2 5 2 Blood Circulation in the Placenta	52
2 6 Human Liver	53

2 6 1	Structural Anatomy of the Liver	54
2 6 2	Functional Anatomy of the Liver	54
3.	Using an IVIM Model to Assess Liver Microvasculature	57
3 1	Introduction	58
3 2	Materials and Methods	61
3 2 1	Subject Population	61
3 2 2	MR Technique	62
3 2 2 1	Breath hold protocol	63
3 2 2 2	Navigator echo respiratory triggered free breathing protocol	64
3 2 3	Image Analysis	65
3 3	Results	69
3 3 1	Perfusion Fraction	72
3 3 2	Diffusion Coefficient	76
3 3 3	Pseudo-Diffusion Coefficient	79
3 4	Discussion	82
3 4 1	Comparison of the IVIM Parameters for Different ROIs	85
3 4 2	Breath Hold Protocol versus Free Breathing Protocol	87
3 4 3	Comparison with IVIM Parameter Values in the Literature	92
3 4 3 1	The IVIM study of Yamada et al	94
3 4 3 2	The IVIM study of Luciani et al	95
3 5	Conclusions	100

4.	Using an IVIM Model to Assess Blood Flow in the Placenta	102
4 1	Introduction	103
4 2	Materials and Methods	104
4 2 1	Subject Population	104
4 2 2	MR Technique	105
4 2 3	Image Analysis	107
4 3	Results	110
4 3 1	IVIM Parametric Maps	111
4 3 2	IVIM Parameters for Different ROIs	111
4 3 3	IVIM Parameters Versus Gestational Age	119
4 3 4	IVIM Parameters for ROI _{in} and ROI _{out}	123
4 4	Discussion	126
4 4 1	Placental IVIM Studies in the Literature	131
4 4 2	Comparison of our IVIM Parameters with the Literature	134
4 4 2 1	Diffusion Coefficient	135
4 4 2 2	Pseudo-Diffusion Coefficient	136
4 4 2 3	Perfusion Fraction	136
4 4 3	WP-ROI versus U-ROI	137
4 4 4	ROI _{in} versus ROI _{out}	138
4 4 5	Coefficients of Variation for the IVIM Parameters	140
4 4 6	Discussion of IVIM Parameters	142
4 5	Conclusions	147

5. Rectified Noise Bias Correction	150
5 1 Introduction	151
5 2 Theory of Rectified Noise Bias Correction	153
5 2 1 Background Theory	153
5 2 2 Extension of the Rectified Noise Bias Correction Algorithm	156
5 3 Methods	158
5 4 Results	161
5 5 Discussion	165
5 6 Conclusions	168
6 General Conclusions.....	169
Appendix A Liver Statistics	173
Appendix B Placenta Statistics	178
Appendix C $\tilde{\theta}$ as a Function of θ and N Calculated Using μ_χ and σ_g	183
Appendix D $\tilde{\theta}$ as a Function of θ and N Calculated Using $\langle M_N \rangle_{\chi^2}$ and σ_g	185
Appendix E Simulated PDFs Before and After the RNBC Calculated Using $\langle M_N \rangle_{\chi^2}$ and σ_g for Different N Element Coils	187
References	190

List of Tables

3 1	Mean D , D^* , and f values for the right side of the liver for the FB-protocol	72
3 2	Mean D , D^* , and f values for the right side of the liver for the BH-protocol	72
3 3	Mean D , D^* , and f values for the right side of the liver for the FB-protocol when a t -test was performed, and a two tailed p -value is reported	72
3 4	IVIM parameter values for the right side of the liver measured with our FB-protocol compared with those obtained by Luciani et al [9] with a pneumatic belt RT sequence	93
3 5	IVIM parameter values for the right side of the liver measured with our BH-protocol compared with those obtained by Yamada et al [12] with their BH-protocol	93
3 6	Mean IVIM parameter values averaged over the right side of the liver (Ottawa) and the Luciani [9] data, when a t -test was performed, and a two tailed p -value is reported	93
3 7	IVIM parameter values for the right side of the liver measured with our FB-protocol compared with those obtained by Patel et al [95] using an NRT sequence	93
4 1	Slopes for the IVIM parameters vs gestational age	121
4 2	Mean IVIM parameter values averaged over GA = 18 to 35 weeks	121
4 3	Mean IVIM parameter values averaged over GA = 18 to 35 weeks (Ottawa) and the Notthingam data, when a t -test was performed, and a two tailed p -value is reported	122
4 4	Mean IVIM parameter values averaged over all subjects	124
5 1	Computed estimates of θ_N as a function A and N for the case where the	163

exact values of μ_χ and σ_g are used

Appendix A Liver statistics	173
Appendix B Placenta Statistics	178
Appendix C $\tilde{\theta}$ as a function of θ calculated using μ_χ and σ_g for $N = 1, 2, 4, 8, 16$	160
Appendix D $\tilde{\theta}$ as a function of θ calculated using $\langle M_N \rangle_{\chi^9}$ and σ_g for $N = 1, 2, 4, 8, 16$	162

List of Figures

- 2 1 Precession of μ about B_0 at the Larmor angular frequency $\omega_0 = \gamma B_0$
 The angle θ represents the phase of the precession 16
- 2 2 Energy level diagram for a nuclear spin with $I = 1/2$ in a static
 magnetic field, B_0 . $\Delta E = \gamma \hbar B_0$ represents the energy difference
 between levels separated by $\Delta m = \pm 1$. The bold line schematically
 represents the relative population in each state for an ensemble of
 spins at thermal equilibrium 17
- 2 3 (a) The total magnetic field, B_{total} , in the laboratory frame (x, y, z)
 (b) The effective field, B_{eff} , in the RRF (x', y', z') which rotates at
 angular frequency ω 20
- 2 4 (a) The trajectory of M in the laboratory frame (x, y, z) in the
 presence of both 1) a longitudinal static magnetic field, B_0 , and 2) a
 transverse rotating field B_1 . On resonance ($\omega = \omega_0$), M precesses
 simultaneously about both B_0 , at frequency ω_0 , and B_1 , at frequency
 ω_1 , where $\omega_0 \gg \omega_1$. (b) The trajectory of M in the RRF (x', y', z')
 on resonance. For this case the longitudinal effective magnetic field
 will be zero 21
- 2 5 Diagrams of (a) longitudinal magnetization M_z and (b) transverse

	magnetization M_{xy} relaxation as a function of time, t	22
2 6a	The Stejskal-Tanner Pulsed-Gradient Spin Echo (PGSE) sequence where δ is the pulse duration, Δ is the diffusion time, G is the gradient amplitude and TE is the time to the echo	28
2 6b	The twice-refocussed spin echo sequence [82] Gradient timings are adjusted to minimize the effect of magnetic fields generated by eddy currents	29
2 7	(a) A gradient waveform, $G_x(t)$ (b) The first derivative of the gradient waveform, $dG_x(t)/dt$ (c) One of the induced eddy current terms, $g_x(t)$ (d) The intended and the actual gradient waveforms [98]	32
2 8	The figure contains a screen capture from the MR scanner showing the location of the navigator echo ROI (i.e. the blue box) positioned over the diaphragm for the 2D-PACE navigator echo respiratory triggering technique. The yellow box indicates the volume that is to be imaged	46
2 9	The motion of the diaphragm during free breathing is represented by the green line. The red boxes depict the acceptance windows that the respiratory algorithm has set for the training period	48
2 10	The green line represents the motion of the diaphragm during free breathing in this screen capture from the MR scanner. The yellow boxes represent the acceptance windows for image acquisition at the end of expiration	48
3 1	An image of a healthy liver (slice 11, volunteer 16). A HASTE sequence was used for this acquisition	63
3 2	The whole right side of the liver (WRL) ROI is shown in red and the periphery of the right side of the liver (PRL) ROI is shown in blue. All ROIs have been drawn on anatomical images for a normal liver (volunteer 16)	66
3 3	Typical diffusion decays for the WRL-ROI (black) and the PRL-ROI (red) (volunteer 16)	67
3 4	An anatomical image for a normal liver (slice 19, volunteer 16) is shown on the lower left and f (upper left), D (upper right) and D^* (lower right)-maps color overlaid onto the anatomical image, are shown as indicated. The color table ranges for the maps are 1) 0 – 100% for the f -map, 2) $(0 - 2) \mu\text{m}^2/\text{ms}$ for the D -map and 3) $(0 - 200) \mu\text{m}^2/\text{ms}$ for the D^* -map	68

- 3 5 *f* values (mean \pm SD) are shown for the WRL-ROI, the three 100-pixel ROIs and the PRL-ROI, averaged over all slices in each case. The BH-protocol was used for volunteers 1 to 3 and the FB-protocol was used for volunteers 4 to 11. The horizontal lines show the mean over all volunteers for the PRL-ROI (red) and the WRL-ROI (black). For clarity, error bars are shown in a) for ROI1 only 75
- 3 6 *D* values (mean \pm SD) are shown for the WRL-ROI, the three 100-pixel ROIs and the PRL-ROI, averaged over all slices in each case. The BH-protocol was used for volunteers 1 to 3 and the FB-protocol was used for volunteers 4 to 11. The horizontal lines show the mean over all volunteers for the PRL-ROI (red) and the WRL-ROI (black). For clarity, error bars are shown in a) for ROI1 only 78
- 3 7 *D** values (mean \pm SD) for the WRL-ROI, the three 100-pixel ROIs and the PRL-ROI, averaged over all slices in each case. The BH-protocol was used for volunteers 1 to 3 and the FB-protocol was used for volunteers 4 to 11. The horizontal lines show the mean over all volunteers for the PRL-ROI (red) and the WRL-ROI (black). For clarity, error bars are shown in a) for ROI1 only 81
- 4 1 MRI image showing the anatomy of a healthy placenta (slice 19, patient 2). This image was acquired with a diffusion weighted echo planar sequence with $b = 0$ 105
- 4 2 The WP-ROI (red) and the three 100-pixel rectangular ROIs (blue) are shown on the image on the left and the ROIs drawn around the outer (red) and inner (blue) parts of the placenta are shown on the image on the right 110
- 4 3 Typical diffusion decays for the WP-ROI and a 100 pixel-ROI. The decays shown are for the WP-ROI (black) and for one of the 100 pixel ROIs (red) shown in (slice 19, patient 2) 111
- 4 4 An anatomical image as well as *D*, *D** and *f*-maps, color overlaid onto an anatomical image, are shown for a healthy pregnancy (slice 19, patient 2). Two areas of blood movement can be seen on the *D**-map (shades of blue and green, respectively) and the *f*-map. Areas where maternal blood enters the placenta from the spiral arteries can be seen and are indicated by the arrows on the *D** map. The color table ranges for the maps are a) 0 – 100% for the *f*-map, b) (0 – 2) $\mu\text{m}^2/\text{ms}$ for the *D*-map and c) (0 – 200) $\mu\text{m}^2/\text{ms}$ for the *D**-map 112
- 4 5 Perfusion fraction, *f* (%), values plotted for each volunteer for 1) the 100-pixel ROIs, 2) the whole placenta ROI (WP-ROI) and 3) the combined 100-pixel ROIs (U-ROI), averaged over all slices in each case. For clarity, error bars are shown for ROI1 only. The error bars

	correspond to the mean \pm SD	115
4 6	f values for each volunteer for the WP-ROI and the U-ROI, averaged over all slices in each case. The error bars correspond to mean \pm SD	115
4 7	Diffusion coefficient values plotted for each volunteer for 1) the 100-pixel ROIs, 2) the WP-ROI and 3) the U-ROI, averaged over all slices in each case. For clarity, error bars are shown for ROI1 only. The error bars correspond to the mean \pm SD	116
4 8	D values plotted for each volunteer for the WP-ROI and the U-ROI, averaged over all slices in each case. The error bars correspond to the mean \pm SD	116
4 9	Pseudo-diffusion coefficient values plotted for each volunteer for 1) the 100-pixel ROIs, 2) the WP-ROI and 3) the U-ROI, averaged over all slices in each case. For clarity, error bars are shown for ROI1 only. The error bars correspond to the mean \pm SD	117
4 10	D^* values plotted for each volunteer for the WP-ROI and the U-ROI, averaged over all slices in each case. The error bars correspond to the mean \pm SD	117
4 11	Typical behaviour for f plotted as a function of slice number for the WP-ROI and the U-ROI. The data are from patient 9. The error bars correspond to the mean \pm SD	118
4 12	Typical behaviour for D plotted as a function of slice number for the WP-ROI and the U-ROI. The data are from patient 9. The error bars correspond to the mean \pm SD	118
4 13	Typical behaviour for D^* plotted as a function of slice number for the WP-ROI and the U-ROI. The data are from patient 9. The error bars correspond to the mean \pm SD	119
4 14	f -values for the WP-ROI and the U-ROI plotted as a function of gestational age (GA). The error bars correspond to the mean \pm SD. The black line shows the linear least squares fit to the WP-ROI data	120
4 15	D -values for the WP-ROI and the U-ROI plotted as a function of gestational age (GA). The error bars correspond to the mean \pm SD. The black line shows the linear least squares fit to the WP-ROI data	120
4 16	D^* -values for the WP-ROI and the U-ROI plotted as a function of gestational age (GA). The error bars correspond to the mean \pm SD. The black line shows the linear least squares fit to the WP-ROI data	121

4 17	Signal attenuation versus b -value for inner (i.e. fetal side) and outer (i.e. maternal side) placental regions for subject 1, acquired using a breath hold technique. The bi-exponential nature of the decays can clearly be seen.	123
4 18	$f_{out} - f_{in}$ values for each volunteer (mean \pm SD). $f_{out} = f_{in}$ is indicated by a solid line and negative values are shown in red.	124
4 19	$D_{out} - D_{in}$ values for each volunteer (mean \pm SD). $D_{out} = D_{in}$ is indicated by a solid red line.	125
4 20	$D_{out}^* - D_{in}^*$ values for each volunteer (mean \pm SD). $D_{out}^* = D_{in}^*$ is indicated by a solid red line.	125
5 1	Uncorrected simulated NCDs for several values of $\theta_N = A_N/\sigma_g$ for a 4-element phased array and $\sigma_g = 1$. The black, red, blue, green, purple and dark blue curves correspond to $A = 0.0, 0.5, 1.0, 2.0, 3.0, 4.0$, respectively.	162
5 2	Simulated PDFs before (\blacktriangle) and after (\blacksquare) the RB correction computed using exact values for μ_χ and σ_g , for $N = 1$ (red), $N = 2$ (black) and $N = 4$ (olive) elements and $\theta = 0.5$. The vertical lines show the corresponding PDF means for the corrected (dashed) and uncorrected (solid) PDFs for $N = 2$. Note that, for this case, the mean of the corrected PDF is very close to the expected value of 0.707.	164
Appendix E	Simulated PDFs before and after the RNBC calculated using $\langle M_N \rangle_{\chi^2}$ and σ_g for different N element coils with $N = 1, 2, 4, 8$, and 16.	187

List of Abbreviations

<i>ADC</i>	Apparent Diffusion Coefficient
BH	Breath Hold
CV	Coefficient of Variation
CPMG	Car Purcell Meiboom Gill
DW	Diffusion Weighted
DWI	Diffusion Weighted Imaging
DTI	Diffusion Tensor Imaging
<i>D</i>	Free diffusion coefficient
EPI	Echo Planar Imaging

FB	Free Breathing
FGR	Fetal Growth Restriction
FID	Free Induction Decay
FOV	Field of View
GA	Gestational Age
GRAPPA	Generalized Autocalibrating Partially Parallel Acquisition - a Parallel Imaging technique performed in k-space
HASTE	Half-Fourier Acquisition Single-shot Turbo Spin Echo
IDEA	Integrated Development Environment and Application – Siemens sequence programming software package
iPAT	integrated Parallel Acquisition Techniques
IVIM	IntraVoxel Incoherent Motion
LS	Least-Squares
MR	Magnetic Resonance
MRI	Magnetic Resonance Imaging
NCD	Non-central Chi Distribution
NMR	Nuclear Magnetic Resonance
NRT	Navigator echo Respiratory Triggering
PDF	Probability Density Function
PGSE	Pulsed Gradient Spin Echo
PACE	Prospective Acquisition Correction
PI	Parallel Imaging
PRL-ROI	Periphery Right Liver Region of Interest
QMR	Quantitative Magnetic Resonance
RNB	Rectified Noise Bias
RNBC	Rectified Noise Bias Correction

RBF	Rectified Noise Floor
RF	Radiofrequency
RRF	Rotating reference Frame
ROI	Region of Interest
SD	Standard Deviation
SS	Single Shot
SNR	Signal-to-Noise Ratio
SPAIR	Spectral Adiabatic Inversion Recovery – a fat suppression technique
STIR	Short Time Inversion Recovery
TE	Echo Time
TR	Repetition Time
T_1	spin-lattice relaxation time
T_2	spin-spin relaxation time
T	absolute temperature
TRSE	Twice Refocusing Spin Echo
US	Ultrasound
U-ROI	United Region of Interest
WP-ROI	Whole Placenta Region of Interest
WRL-ROI	Whole Right Liver Region of Interest

Chapter 1

Introduction

1.1 Historical Introduction

The phenomenon of nuclear magnetic resonance (NMR) was first discovered in 1946 by Bloch and Purcell who were awarded the Nobel Prize in physics in 1952 for their important discovery. Between 1950 and 1970 NMR was used in physical and chemical molecular analysis. Magnetic resonance imaging (MRI) began in 1973 when the research groups lead by Sir Peter Mansfield and Paul Lauterbur independently introduced the use of magnetic field gradients into the NMR procedure to obtain signal localization [1,2]. In the beginning, back projection reconstruction methods, which were already well established in other areas of medical imaging (e.g. Computer Assisted Tomography), were used to compute the MRI images. In 1975 Ernst introduced the concepts of phase and frequency encoding and the use of the Fourier transform into MRI [3]. This is the approach most commonly used today. With continuous developments in MRI hardware and information technology, fast dynamic MR acquisition has become possible, opening up new diagnostic and interventional possibilities for MRI. The 2003 Nobel Prize in medicine was awarded jointly to Sir Peter Mansfield and Paul Lauterbur for their important contributions to MRI and to medicine.

1.2 Introduction to Diffusion in Magnetic Resonance

The method for sensitizing the magnetic resonance (MR) signal to the diffusion of water molecules was developed for NMR in 1965 by Stejskal and Tanner [4] and for MRI in 1985 by Le Bihan et al. [5], who used essentially the same approach for sensitizing MR images to diffusion as was proposed by Stejskal and Tanner.

With the introduction of diffusion weighted (DW) MRI, studies of water transport in biological tissues *in vivo* became more popular. Studies of molecular displacements over distances comparable to the cell size are expected to give insight into the geometry and spatial organization of the tissue as well as water exchange processes in each compartment in both normal and diseased tissue.

Diffusion weighted MRI (DWI) has been very successful for the past twenty years. Its main application has been in the evaluation of intracranial diseases such as cerebrovascular disease, depression, neurotoxicity and especially detecting early changes within the brain for patients with acute stroke, before any abnormality can be seen with other imaging techniques. Although the first clinical images of the brain were obtained in the 1980s, it was not possible to use DWI clinically until the 1990s when the major technological obstacles were overcome by a series of hardware improvements.

In the early days of MRI, most scanners operated at relatively low magnetic field strengths in the range of 0.5 to 1.0 Tesla. As a result, the signal intensity obtained was weak. At that time, gradient strengths could not go beyond 10 mT/m due to hardware limitations and eddy currents caused image quality to be poor, at least by today's standards. These weak gradients also meant that the MR signal could only be weakly sensitized to diffusion. The absence of echo planar imaging (EPI), a very fast method for generating MR images, also made acquisition times for DWI unreasonably long and the acquired DW images were unreliable since they were very sensitive to macroscopic motion. As for MR

imaging of the body, since there was no respiratory gating, the motion artifacts were atrocious and the images were worthless

These days much faster protocols are available and the entire brain can be imaged in a second DWI of extracranial sites, including the abdomen and the pelvis, is now possible. A full set of DW measurements can be acquired in 1 to 5 minutes and no contrast agent is required. The possibility of obtaining both qualitative and quantitative diffusion information as well as much higher quality DW images of the abdomen increased the interest in using DWI as an application for tumour assessment and/or disease diagnosis.

Water diffusion in tissue is a very complex process. The DW signal comes from the motion of water molecules in the extracellular space, the intracellular space and the intravascular space. In the diffusion process, molecules move due to their thermal energy and collide with each other and with other structures in their local environment (e.g. cell membranes). These collisions cause the direction of motion for the molecules to change in a random fashion resulting in a molecular random translational motion on a microscopic scale which is well described as a random walk process. Einstein was the first to correctly explain Brownian motion in terms of the random motion of particles due to their thermal energy in 1905 [6], thereby confirming the existence of atoms. In a homogeneous liquid, the root mean square displacement, Δr , of the molecules over a given diffusion time, t_d , can be determined from the Einstein equation

$$\Delta r = \sqrt{2dDt_d} \quad (1.1)$$

where $d = 1, 2$ or 3 when diffusion takes place in 1, 2 or 3-dimensions, respectively, and D is a physical constant, called the self-diffusion coefficient, which characterizes the diffusion. The root mean square displacement of water molecules that occurs during a diffusion measurement is estimated to be about $10 \mu\text{m}$, which is comparable to the mean size of cells in the human body. Thus, the information obtained from DWI can be expected to give information about the structure of the tissue at the cellular scale. This is one of the reasons why DWI has been seen as a potential tool for imaging tumour microcirculation (before and after treatment) in the abdomen.

The MR signal is sensitized to diffusion in a specific direction by inserting appropriate magnetic field gradient pulses into an MR pulse sequence. Images with different degrees of diffusion weighting can be obtained if various gradient pulse amplitudes are applied. The direction in which the MR sequence is sensitive to diffusion is determined by the orientation of the applied gradient pulses. In pure liquids, the signal decay, as a function of the diffusion weighting, is exponential and can be expressed as

$$S(b)/S_0 = \exp(-bD) \quad (1.2)$$

where b is a measure of diffusion sensitization and S and S_0 are the signals at b and $b = 0$, respectively. The b -value depends on both the amplitude and the duration of the diffusion gradients. The overall diffusion signal measured across an image voxel results from the integration of all of the microscopic displacements of the water molecules present in the voxel.

1.2.1 Intravoxel Incoherent Motion

“I had a fuzzy intuition that perhaps molecular diffusion measurement would result in low values in solid tumors because of molecular movement restriction while diffusion would be somewhat enhanced in flowing blood ” Denis Le Bihan [7]

In the mid 1980s, Le Bihan proposed that, in addition to diffusion, the flow of water molecules in blood in capillary segments that are oriented in a pseudorandom manner can also be treated as a random walk process and he presented a mathematical model based on diffusion theory to explain his results. This is known as the IntraVoxel Incoherent Motion (IVIM) model. The corresponding diffusion and pseudo-diffusion coefficients differ only by about one order of magnitude (D , the molecular diffusion coefficient of water in tissues, is about $1 \mu^2/\text{ms}$, while D^* , the pseudo-diffusion coefficient associated with capillary blood flow, is about $10 \mu^2/\text{ms}$ in the brain [8] and $70 \mu^2/\text{s}$ in the liver [9]). The proximity of these values allows D and D^* to be evaluated together with the same diffusion MRI sequence. It also means that DWI images are prone to contamination by blood microcirculation effects.

The IVIM model is considered in substantially more detail in Chapter 2

1.3 Abdominal Imaging Literature Review

The “*ADC* concept” has been generally adopted in the medical MR literature because it was obvious that the diffusion coefficient, D , should be replaced for tissue studies by a “global” parameter, known in the MR literature, as the apparent diffusion coefficient or the *ADC*. The measured diffusion coefficient is not a true measure of ‘intrinsic’ diffusion, it represents the complex molecular displacements that occur in biological tissues due to interactions of water molecules with cellular structures and processes over a given diffusion time. In a voxel that contains thousands of cells and tissue components, the diffusion signal is given by the average of many different effects and microscopic environments. With the IVIM model discussed above the measured diffusion decay is considered to be bi-exponential, with one component corresponding to diffusion and the other to the pseudo-diffusion process associated with the water in the microvasculature. When the *ADC* approach is used, the decay is inherently assumed to be mono-exponential where the *ADC* is the decay constant. In practice, the measured diffusion decay fits very well to a bi-exponential. However, for some tissues, such as the brain, the contribution from the second process is quite small and the deviation from exponentiality is relatively minor. For these tissues the *ADC* values can be quite useful. For more vascular organs, such as the liver or the placenta, the diffusion decay is strongly bi-exponential and, if the *ADC* approach is used, it must be done with caution. For such tissues the IVIM model is preferable.

Numerous studies of DWI for liver have recently emerged, including for liver lesion detection and characterization [10-28], for the diagnosis of liver fibrosis or cirrhosis [29-33] and for liver tumour treatment response [34-41]. Unfortunately, the reported *ADC* values vary over a very wide range (300% variation) for both normal liver and for focal hepatic lesions [42,43]. This variation is probably related to different sets of *b*-values used in the protocol (since the decay deviates strongly from the assumed exponential decay), different algorithms used for image analysis, the stage of the tumour when investigated [43] and different experimental set-ups used for image acquisition. Most of these studies mentioned above have used breath hold single shot (SS) EPI to acquire DW images, using various *b*-values. These sequences are fast but they suffer from poor image quality when higher *b*-values are used. These results demonstrate that there is a need for the implementation and validation of more reliable data acquisition techniques and image analysis tools for DWI in the abdomen.

The development of parallel imaging has been very important for abdominal and pelvic MRI because it enables the use of shorter echo times and reduced echo train length, resulting in a faster acquisition of images with a good signal to noise ratio (SNR) that are relatively undegraded by motion and other artifacts. Parallel imaging [44,45] and pulse triggering [46] have been proposed to improve diffusion image quality and the precision of *ADC* measurements.

Respiratory triggering is another method that has been used to improve DW image quality, it is a technique that avoids motion artifacts by synchronizing image acquisition with the patient's breathing cycle and by doing the data

acquisition at the end of the expiration phase [47-55] Various techniques have been used for respiratory triggering bellow systems in combination with a strain gauge, temperature monitoring using face masks, and elastic breathing belts, as well as navigator echoes The major advantages of navigator echoes are that no additional hardware is needed, patient set up is easier and this technique works much better than the others

A few recent studies have reported the use of respiratory triggered liver DWI [47-49] where the triggering was done without using navigator echoes Gourtsoyianni et al [48] assessed the utility of the *ADC* values obtained with a non-navigator echo respiratory triggered SS EPI DWI sequence (n = 38) for characterization of liver lesions and found sensitivity and specificity values of 100% for the diagnosis of malignancy

There are only a few studies in the literature that use the IVIM model for either of the organs investigated for this thesis, there are two for the liver [9,12] and two for the placenta [56-58] Detailed comparisons of these results with ours are found in Chapter 3 for the liver and Chapter 4 for the placenta

1.3.1 IVIM Perfusion versus Classical Perfusion

Throughout this thesis the terms perfusion, perfusion coefficient and perfusion fraction are used In the classical physiology literature perfusion refers to the delivery of nutrients and the removal of waste products from a tissue and is expressed in millilitres per minute per 100 grams of tissue The “perfusion” measurements reported in this thesis do not measure perfusion in this classical

sense, although they are closely related [59]. Classical perfusion in a given tissue is determined primarily by blood flow to the tissue and in the microvasculature of the tissue. The “perfusion” parameters reported here are determined by the microcirculation in the tissue of interest and are thus very closely related to classical perfusion but are not exactly the same. By “perfusion”, we are really referring to the microcirculation of blood in the tissue. The “perfusion coefficient”, which is equated with the pseudo-diffusion coefficient introduced above, is an indirect measure of the movement of the blood in the tissue microvasculature and has units of a diffusion coefficient (i.e. μ^2/ms). The “perfusion fraction” refers to the fraction of the MR signal that is associated with the “perfusion coefficient”. In other words, it gives the fraction of the MR signal associated with blood moving in the microvasculature of the tissue. See Section 2.3.3 for further details. The decision to use this terminology was made for consistency with related work in the MRI literature.

1.4 Thesis Outline

DWI is sensitive to microscopic motion in biological tissues, including self-diffusion of water molecules and the microcirculation of blood in the capillary network of the tissue. It is overly simplistic to assume that the attenuation of the diffusion signal intensity as the b -value increases is a simple exponential decay in tissue, particularly in highly vascular tissues such as the liver or the placenta. In this thesis the aim was to investigate water diffusion in these two highly vascular

organs using the IVIM model, a model that more closely represents the hemodynamics in the tissue of interest. Organs such as the placenta and the liver have not been properly investigated in the past due in part to hardware limitations and/or poor analysis tools. With new advancements in the hardware technology, a re-evaluation of the models used to describe the DWI decay data is required.

To increase the image quality of the acquired DWI images as well as the precision and accuracy of the diffusion measurements relative to previously reported studies for both organs, the experimental procedure was enhanced by using 1) parallel imaging, 2) navigator echo respiratory triggering, 3) a double echo diffusion sequence that inherently compensates for the effects of eddy currents 4) SPAIR fat suppression and 5) a superior approach to image analysis. The experiments reported here represent the first studies to give results for abdominal DWI performed with these enhancements and analyzed using the IVIM model [60,61]. We believe that, for both of these organs, the IVIM parameters reported here are considerably more reliable than those previously reported in the literature.

The IVIM parameters discussed in this thesis are presented for 1) a region of interest (ROI) covering the whole right side of the liver or the entire placenta, 2) 3 separate 100-pixel square ROIs located around the periphery of the right side of the liver or placed carefully across the placenta to avoid big blood vessels or turbulent flow, 3) an ROI corresponding to the union of the three 100-pixel ROIs and 4) a pixel-by-pixel analysis from which parametric maps were generated.

The information obtained from these different choices and their relative merits and importance are discussed

In Chapter 2, a review of all of the relevant background for the thesis is given. In Chapters 3 and 4, diffusion decay measurements for normal liver and healthy placenta in human volunteers *in vivo* are presented and discussed. The experimental results are explained using the bi-exponential IVIM model. One potential limitation of the IVIM approach, where the full diffusion decay must be measured, is that rectified noise bias can distort the decay for large b -values where the SNR can sometimes be quite low (e.g. when the voxel size is small). In Chapter 5 a useful technique for removing this noise bias from the pixel intensities of magnitude MR images is presented for images acquired using phased array coils. The thesis is finalized with Chapter 6, General Conclusion.

Chapter 2

Theory and Background

2.1 Introduction

In this chapter, the basic physical principles of nuclear magnetic resonance (NMR) and diffusion are explained in order to facilitate a better understanding of the studies presented in the following chapters. Section 2.2 is dedicated to the presentation of NMR phenomenology. Section 2.3 describes diffusion in magnetic resonance imaging (MRI) with particular emphasis on the Intravoxel Incoherent Motion (IVIM) model. The PACE respiratory triggering technique is explained in section 2.4. In the two final sections of this chapter, introductions to the anatomy and physiology of the placenta and the liver are given. The principles behind the MR imaging experimental methodology used in the placenta and liver studies are also introduced in section 2.3 and 2.4.

2.2 Principles of Nuclear Magnetic Resonance

2.2.1 The Nuclear Magnetic Moment in a Static Magnetic Field

Magnetic resonance (MR) phenomena can be observed in isotopes with non-zero nuclear spin as a result of the fact that they inherently possess both a magnetic moment and angular momentum [62]. Nuclei are composed of nucleons (i.e. protons and neutrons), each of which has a spin of $\frac{1}{2}$. The coupling of the spins of the nucleons that form a particular nucleus determine the nuclear spin, I , where I may be integral or half-integral (i.e. $I = n/2$ with n being an integer). As a result, the total angular momentum of the nucleus, J , can be written as [63]

$$J = \hbar I, \quad (2.1)$$

where \hbar is Dirac's constant and I is the dimensionless nuclear spin angular momentum operator I^2 has eigenvalues $I(I+1)$ and for ^1H , $I = 1/2$. Note that throughout this thesis, a bold font will be used to indicate vector quantities

The total nuclear magnetic moment, $\boldsymbol{\mu}$, and \boldsymbol{J} are parallel vectors that are related by γ , a scalar known as the gyromagnetic ratio, which is a constant for a given nucleus

$$\boldsymbol{\mu} = \gamma \boldsymbol{J} \quad (2.2)$$

The gyromagnetic ratio for hydrogen, $\gamma_{^1\text{H}}$ is equal to $2.675 \times 10^8 \text{ rad T}^{-1} \text{ s}^{-1}$ [64]

The interaction of $\boldsymbol{\mu}$ with $\boldsymbol{B}_0 = B_0 \boldsymbol{k}$ causes a splitting of the ground state energy level. This is known as the Zeeman effect and is described by the Hamiltonian [64]

$$H = -\boldsymbol{\mu} \cdot \boldsymbol{B}_0 = -\gamma \hbar I_z B_0 \quad (2.3)$$

The allowed energies, which correspond to the eigenvalues of this Hamiltonian, are given by

$$E = -\gamma \hbar B_0 m, \quad (2.4)$$

where $m = -I, -I+1, \dots, I-1, I$ are the eigenvalues of I_z [64]. The energy difference between adjacent levels is

$$\Delta E = \gamma \hbar B_0 \quad (2.5)$$

An externally applied static magnetic field, \boldsymbol{B}_0 , will exert a torque on $\boldsymbol{\mu}$. As a result, $\boldsymbol{\mu}$ will change, in a short time dt , by an amount $d\boldsymbol{\mu}$ corresponding to a rotation through an angle $d\theta$ in the plane perpendicular to \boldsymbol{B}_0 (see Fig. 2.1). This precessional motion of $\boldsymbol{\mu}$ represents the dynamics of any isolated magnetic

moment in a static magnetic field in both classical and quantum mechanical approaches to NMR [64] The frequency of precession, ω_0 , is known as the Larmor frequency and is directly proportional to B_0

$$\omega_0 = -\gamma B_0 \quad (2.6)$$

This is a fundamental concept in MRI For most clinical MRI scanners $\nu_0 = \omega_0 / 2\pi$ is between about 40 and 130 MHz, corresponding to magnetic field strengths of 1 T to 3 T [64] If Eq (2.6) is inserted into Eq (2.5) the energy separation between adjacent Zeeman energy levels, ΔE , becomes

$$\Delta E = \hbar \omega_0 \quad (2.7)$$

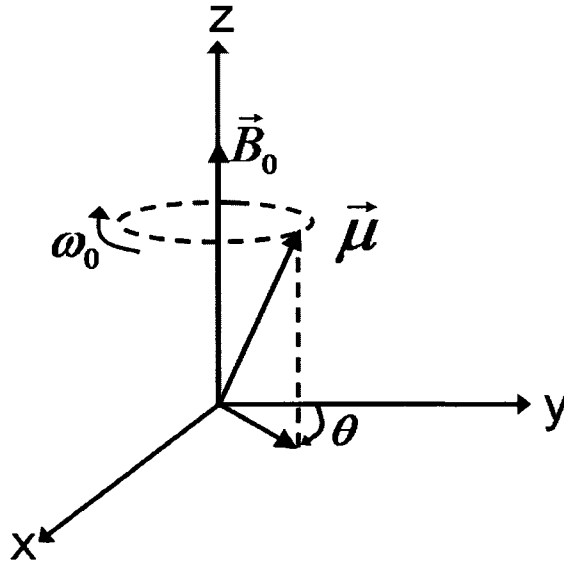


Fig. 2.1. Precession of μ about B_0 at the Larmor angular frequency $\omega_0 = \gamma B_0$. The angle θ represents the phase of the precession

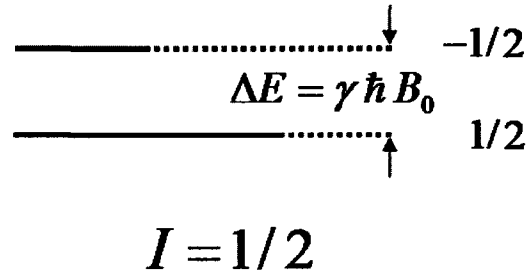


Fig. 2.2. Energy level diagram for a nuclear spin with $I = 1/2$ in a static magnetic field, B_0 . $\Delta E = \gamma \hbar B_0$ represents the energy difference between levels separated by $\Delta m = \pm 1$. The bold line schematically represents the relative population in each state for an ensemble of spins at thermal equilibrium.

2.2.2 Nuclear Spin Energy Level Population in a Static Magnetic Field

For the case of a population of nuclear spins in the presence of a static magnetic field, B_0 , at thermal equilibrium, one can use Boltzmann statistics to find the ratio between the number of nuclei in the lower energy state, n_- , and the number of nuclei in the upper energy state, n_+ [63]

$$\frac{n_-}{n_+} = \exp\left(\frac{\Delta E}{kT}\right), \quad (2.8)$$

where k is the Boltzmann constant, T is the absolute temperature of the spin system and ΔE represents the energy difference between Zeeman levels defined by Eq (2.5). A Zeeman energy level diagram for $I = 1/2$ nuclear spins and the relative population of each state is shown schematically in Fig 2.2.

For a population of N nuclei with spin $I = 1/2$, the polarization P is represented by the fractional excess of nuclei in the lower energy state [63]

$$P = \frac{n_- - n_+}{N} = \frac{n_- - n_+}{n_- + n_+} \quad (2.9)$$

Using Eq (2.8) the polarization P can be rewritten as

$$P = \tanh\left(\frac{\Delta E}{2kT}\right) \quad (2.10)$$

The alignment of the spins in a static magnetic field can also be expressed in terms of the magnetization, \mathbf{M} , which is defined as

$$\mathbf{M} = \sum_{i=1}^N \boldsymbol{\mu}_i, \quad (2.11)$$

where the $\boldsymbol{\mu}_i$ represent the magnetic moments of individual nuclei. In equilibrium, there is a small surplus of nuclear magnetic moments with z-components aligned parallel to \mathbf{B}_0 as opposed to anti-parallel. However, the sum of all magnetic moment projections onto the plane perpendicular to \mathbf{B}_0 (i.e. the transverse plane) is zero. Therefore, the magnitude of the magnetization, M , for spin-1/2 nuclei, can be expressed as

$$M = |\mathbf{M}| = \left| \sum_{i=1}^N \boldsymbol{\mu}_i \right| = \frac{1}{2} N \gamma \hbar P \quad (2.12)$$

The measured signal in MR is proportional to M

The equation of motion of the macroscopic magnetization is obtained by equating the torque exerted on \mathbf{M} by \mathbf{B} with the rate of change of the magnetization [64]

$$\frac{d\mathbf{M}}{dt} = \gamma \mathbf{M} \times \mathbf{B} \quad (2.13)$$

2.2.3 Effect of RF Pulses and Magnetic Field Gradients on M

The concept of the rotating reference frame (RRF) [63] can be used to better understand the effect of a radio frequency (RF) magnetic field on the bulk magnetization of the spin population. Since, in the presence of a static magnetic field, Larmor precession always occurs, the use of a RRF which rotates in the transverse plane at the same angular frequency, ω , as the RF magnetic field, simplifies the analysis.

By applying a time-varying magnetic field, B_1 , with RF carrier frequency $\omega \approx \omega_0$ in a direction perpendicular to B_0 (most efficient excitation), the nuclear spins are excited and the magnetic resonance effect can be measured [63]. The effective magnetic field, B_{eff} , experienced by the spins in the RRF is given by [63]

$$B_{eff} = B_1 + B_0 - \omega/\gamma \quad (2.14)$$

Fig. 2.3 shows the difference between the effect of the total magnetic field in the laboratory frame (B_{total}) and in the RRF (B_{eff}).

In MRI, B_1 is applied as an RF pulse of duration t_p . Magnetization initially aligned along the direction of B_0 will change its orientation due to the RF pulse (see Fig. 2.4). In the RRF (x', y', z'), on resonance (i.e. $\omega = \omega_0$), the magnetization, M , is tipped towards the $x'y'$ -plane, the plane perpendicular to B_0 , by the RF pulse [63]. The angle of rotation or the tip angle, α , depends on the duration of the pulse, t_p , B_1 and γ .

$$\alpha = \gamma \int_0^{t_p} B_1(t) dt \quad (2.15)$$

If B_1 is uniform in the region of interest, α can be calculated using Eq (2.15)

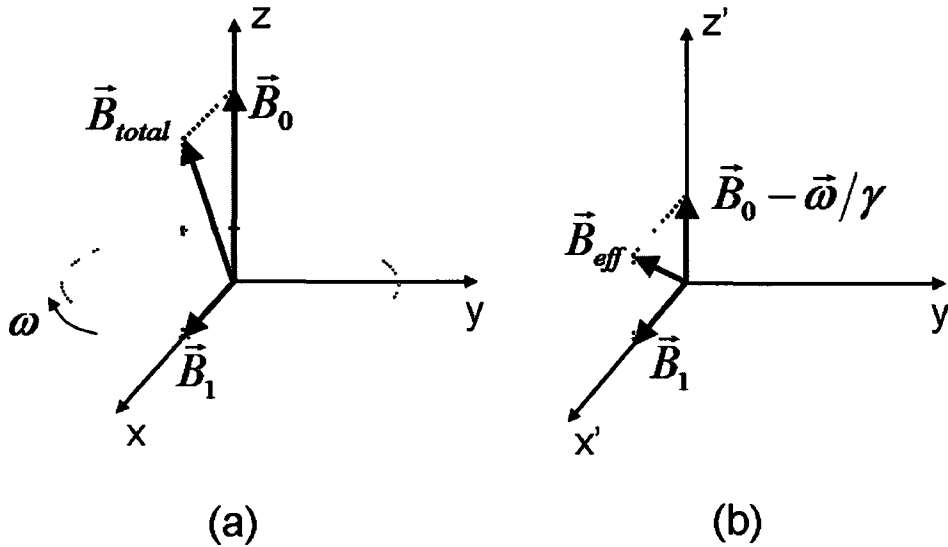


Fig. 2.3. (a) The total magnetic field, \vec{B}_{total} , in the laboratory frame (x, y, z) (b) The effective field, \vec{B}_{eff} , in the RRF (x', y', z') which rotates at angular frequency ω

2.2.4 The Bloch Equations and Relaxation

There are two types of relaxation involved in the return to the “thermal” equilibrium state of a spin population that was previously excited by a resonant RF pulse. The first relaxation process is called longitudinal or spin-lattice relaxation. In this process there is an exchange of energy between the spin system and the *lattice* (i.e. the surrounding thermal reservoir). The return of the longitudinal magnetization, M_z , to its equilibrium value, M_0 , is shown graphically in Fig. 2.5 (a) as an exponential growth and can be described using the

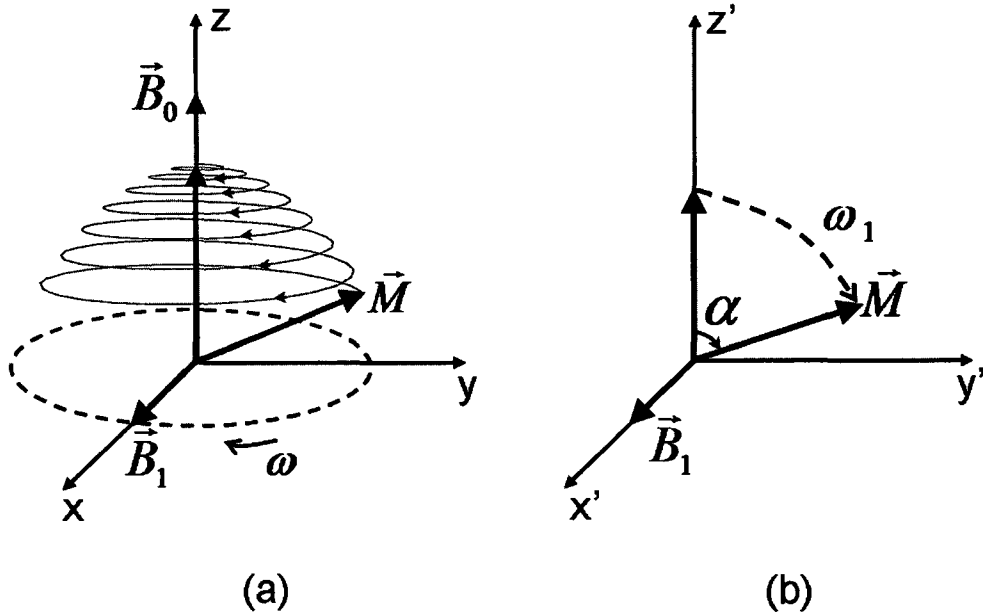


Fig. 2.4. (a) The trajectory of \vec{M} in the laboratory frame (x, y, z) in the presence of both 1) a longitudinal static magnetic field, \vec{B}_0 , and 2) a transverse rotating field \vec{B}_1 . On resonance ($\omega = \omega_0$), \vec{M} precesses simultaneously about both \vec{B}_0 , at frequency ω_0 , and \vec{B}_1 , at frequency ω_1 , where $\omega_0 \gg \omega_1$. (b) The trajectory of \vec{M} in the RRF (x', y', z') on resonance. For this case the longitudinal effective magnetic field will be zero.

equation [64]

$$\frac{dM_z}{dt} = -\frac{M_z - M_0}{T_1}, \quad (2.16)$$

which has the solution

$$M_z(t) = M_z(0) \exp(-t/T_1) + M_0 (1 - \exp(-t/T_1)) \quad (2.17)$$

T_1 , which is referred to as the longitudinal, or spin-lattice, relaxation time, is typically in the range 0.1 to about 3s for water protons in tissues at clinical MRI field strengths.

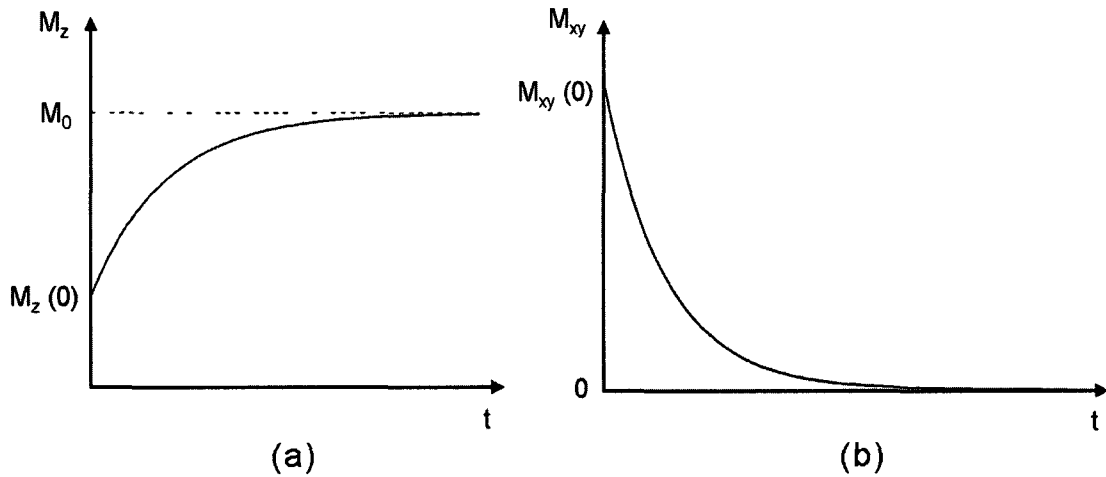


Fig. 2.5. Diagrams of (a) longitudinal magnetization M_z and (b) transverse magnetization M_{xy} relaxation as a function of time, t

The return of the longitudinal magnetization to thermal equilibrium is a dissipative process with part of the absorbed energy being transferred to the lattice in the form of heat

The second form of relaxation is the transverse, or spin-spin, relaxation process which is represented graphically in Fig 2 5 (b) as an exponential decay. In the transverse magnetization there is phase coherence among the nuclear spin states immediately after the RF pulse. Interactions among the spins disturb this spin coherence and the transverse magnetization decays as a result [64]. The equation describing this phenomenon, in the rotating reference frame (on resonance), is

$$\frac{dM_{x'y'}}{dt} = \frac{-M_{x'y'}}{T_2} \quad (2.18)$$

which has the solution

$$M_{x'y'}(t) = M_{x'y'}(0) \exp(-t/T_2) \quad (2.19)$$

T_2 is called the transverse or spin-spin relaxation time

The loss of coherence is observed not only due to spin-spin interactions. In the frequency domain, the resonance peaks will broaden if the local static field varies with position. In this case, the signal in the time domain decays with the apparent transverse relaxation time, T_2^* . Diffusion and chemical exchange can also influence transverse relaxation [64].

The local static field experienced by a nuclear spin is affected by 1) B_0 inhomogeneities related to the magnet design, 2) magnetic susceptibility differences related to the sample's intrinsic magnetic properties, and 3) electronic shielding effects. The use of active or passive shimming can diminish the effect of B_0 inhomogeneity. The magnetic field around the nucleus depends on the surrounding environment (i.e. electronic shells, chemical bonds, etc.). This is why, for a specific static field, B_0 , different substances have slightly different resonance frequencies. In MR, the resonance frequency for a particular substance, ν_S , is often expressed as the difference between ν_S and the resonance frequency, ν_R , of a reference material. This frequency difference is an intrinsic property of the material known as its chemical shift, δ , and it is normally given in parts per million (ppm) to eliminate the dependence on the static magnetic field [64].

$$\delta = \frac{\nu_S - \nu_R}{\nu_0} \cdot 10^6, \quad (2.20)$$

where ν_0 is the operating frequency of the scanner

In practice, measurements of T_2 are traditionally performed using a Carr-Purcell-Meiboom-Gill (CPMG) pulse sequence [65,66] which consists of a 90° RF pulse followed by a set of equally spaced 180° RF pulses that are phase shifted by 90° with respect to the 90° pulse to avoid complications resulting from inaccurate refocusing pulse flip angles [64]

The effects of chemical exchange, diffusion, chemical shift and susceptibility differences can be only partially corrected using pulse sequences such as CPMG. These effects represent some of the challenges faced in the MR experimental world and at the same time they limit the resolution and signal-to-noise ratio (SNR) in MRI [64]

In the rotating reference frame, a single vector equation which describes the time dependence of the magnetization vector

$$\frac{d\mathbf{M}}{dt} = \mathbf{M} \times \gamma \mathbf{B}_{eff} - \frac{M_x \mathbf{x}' + M_y \mathbf{y}'}{T_2} - \frac{(M_z - M_0) \mathbf{z}'}{T_1}, \quad (2.21)$$

can be generated by combining Eqs (2.13), (2.16) and (2.18), where \mathbf{x}' , \mathbf{y}' and \mathbf{z}' are the unit vectors in the x' , y' and z' directions, respectively. This equation, known as Bloch's equation, gives a simplified way of understanding the relaxation effects and is very important in describing MR phenomena. By combining this equation with the classical diffusion equation the Bloch-Torrey equation can be formed [73]

2.3 Diffusion

2.3.1 Diffusion Theory

2.3.1.1 Fick's law and Einstein's equation

MRI provides a good, noninvasive method for the measurement of the translational motion of water molecules in tissue. In 1905, Einstein showed that the random motion of spherical particles suspended in a fluid, a phenomenon known as Brownian motion, was the result of the particles' thermal energy [6]. This microscopic random translational motion is also known as molecular diffusion.

The net displacement, $\mathbf{r}(t) - \mathbf{r}_0$, of a particle (e.g. a water molecule) from its initial position, \mathbf{r}_0 , due to Brownian motion, is time dependent. The particle flux, $\mathbf{J}(\mathbf{r}, t)$, in an isotropic medium is, according to Fick's first law of diffusion, proportional to the particle concentration gradient [67]

$$\mathbf{J}(\mathbf{r}, t) = -D \nabla c(\mathbf{r}, t), \quad (2.22)$$

where D is the diffusion coefficient and the concentration, $c(\mathbf{r}, t)$, is the number of particles per unit volume at a given position, \mathbf{r} , and time is represented by t . The negative sign indicates that the direction of the net motion is from a larger to a smaller concentration.

The continuity theorem [67]

$$\nabla \cdot \mathbf{J}(\mathbf{r}, t) + \frac{\partial c(\mathbf{r}, t)}{\partial t} = 0, \quad (2.23)$$

also applies to this situation from conservation of mass considerations [67]

Combining Eqs (2 22) and (2 23) gives Fick's second law of diffusion

$$\nabla^2 c(\mathbf{r},t) - \frac{1}{D} \frac{\partial c(\mathbf{r},t)}{\partial t} = 0 \quad (2 24)$$

This equation is also known as the diffusion equation The solution of the diffusion equation in an unbounded isotropic medium is [67]

$$c(\mathbf{r}, t) = \frac{N}{(4\pi Dt)^{3/2}} \exp\left[\frac{-(\mathbf{r} - \mathbf{r}_0)^2}{4Dt}\right], \quad (2 25)$$

where N is the total number of particles in the system It can be seen from Eq (2 25) that the particle concentration at time t , $c(\mathbf{r}, t)$, depends only on the net displacement $\mathbf{r}(t) - \mathbf{r}_0$, at time t and not its actual position at time t This is an intrinsic property of Brownian motion Such a displacement causes an attenuation of the MR signal Therefore, if the attenuation of the MR signal can be measured, the mean displacement of the particles (i e the nuclear spins) can be evaluated

Einstein showed that, for an ensemble of particles, the diffusion coefficient measured in the non-equilibrium experiment described above is proportional to the variance of $P(\mathbf{r}_0 | \mathbf{r}, t)$, the conditional probability for a diffusing particle, initially at position \mathbf{r}_0 , to be found at position \mathbf{r} at time t For free diffusion, this conditional probability distribution follows the same diffusion equation as the particle concentration and it can be shown that [67]

$$\langle (\mathbf{r} - \mathbf{r}_0)^2 \rangle = 2dDt_d, \quad (2 26)$$

where $d = 1, 2$ or 3 represents the dimensionality of the system and t_d is called the diffusion time Eq (2 26), known as Einstein's equation, shows that the mean-squared displacement of the diffusing molecules increases linearly with t_d

So far the mathematical description of diffusion presented here assumes that the diffusion process is isotropic and can therefore be described by the isotropic diffusion coefficient D , which is a scalar. For water it can be shown that [6, 66]

$$D = \mu_p k_B T, \quad (2.27)$$

where D describes the rate at which molecules spread out in a fluid medium, μ_p is the mobility of the particles (related to particle size and viscosity), k_B is the Boltzmann constant and T is the absolute temperature.

It can also be shown that D is given by [69]

$$D = \frac{1}{6} \bar{l} \bar{v} = \frac{1}{6} \bar{l}^2 / \bar{t}, \quad (2.28)$$

where \bar{l} , \bar{v} and \bar{t} are the average displacement, average speed and average duration, respectively, for the steps of the random walk process.

2.3.1.2 Diffusion and NMR

Fifty years after Einstein's discovery, Hahn [70] and Carr and Purcell [71] developed a method to measure the self-diffusion coefficient, D , using NMR. Stejskal and Tanner modified this approach by introducing pulsed magnetic field gradients to achieve a more accurate measurement [4]. This method is still widely used in diffusion-weighted MRI to measure the average displacement of water molecules in tissue.

The Pulsed-Gradient Spin Echo (PGSE) sequence, sometimes also referred to as the Stejskal Tanner sequence, is shown schematically in Fig. 2.6a. It consists of a standard spin echo sequence with two additional identical diffusion-

weighting gradient pulses added, one before the 180° RF refocusing pulse and one after it

For the purposes of this discussion the gradient pulses will be assumed to be very short, such that 1) the particle motion during each gradient pulse is negligible and 2) their duration, δ , is much smaller than their separation, Δ . This last condition is known as the narrow pulse approximation [4]

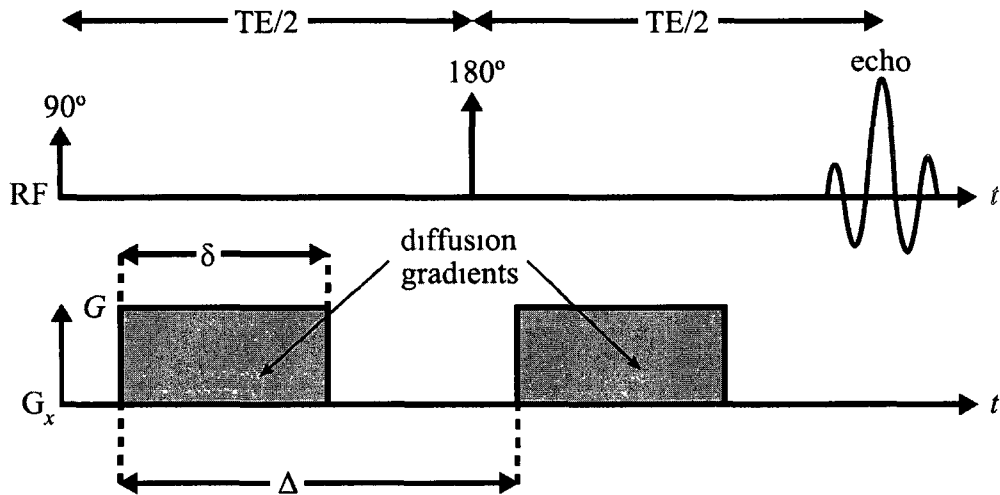


Fig. 2.6a. A schematic diagram of the Stejskal-Tanner Pulsed-Gradient Spin Echo (PGSE) sequence where δ is the pulse duration, Δ is the diffusion time, G is the gradient pulse amplitude and TE is the time to the echo

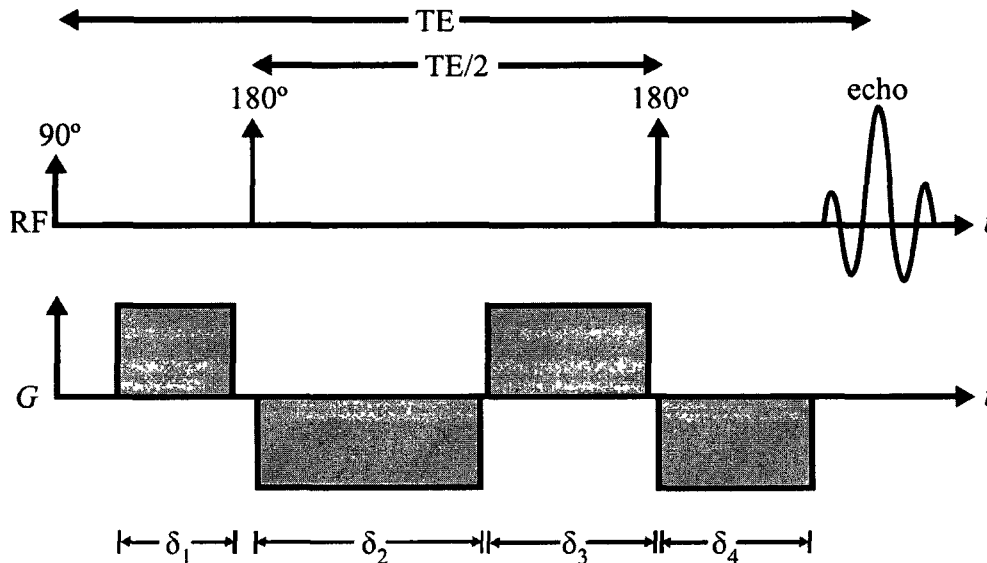


Fig. 2.6b. A schematic diagram of the twice-refocussed spin echo sequence [82] Gradient timings are adjusted to minimize the effect of magnetic fields generated by eddy currents Note that the timings are not drawn to scale

The first gradient pulse causes each spin to accumulate a phase shift that depends on the strength of the applied gradient and the spin's position along the axis of measurement, which will be considered to be the x-axis in this discussion [85] After the gradient is turned off, each spin will have accumulated a phase shift given by

$$\varphi_1 = \int_0^{\delta} \omega dt = \gamma \int_0^{\delta} G_x x_1 dt = \gamma G_x x_1 \delta, \quad (2.29)$$

where γ is the gyromagnetic ratio, G_x is the gradient amplitude and x_1 is the position of the spin along the x-axis at the time the gradient pulse is applied This phase shift will then be inverted by the 180° RF pulse such that φ_1 becomes $-\varphi_1$.

The second gradient pulse causes each spin to accumulate the phase shift

$$\varphi_2 = \gamma \int_{\Delta}^{\delta+\Delta} G_x x dt = \gamma G_x x_2 \delta, \quad (2.30)$$

where x_2 is the position of the spin along the x -axis at the time of the second gradient pulse. The total phase accumulated by the spin, due to the pair of gradient pulses (and the 180° RF pulse), is therefore

$$\varphi = \varphi_2 - \varphi_1 = \gamma G_x (x_2 - x_1) \delta, \quad (2.31)$$

which is proportional to the spin displacement along the x -axis that occurs between the two gradient pulses. If during this time a spin remains stationary (i.e. $x_2 = x_1$), the echo amplitude will be unaffected because the net phase accumulation is zero. Conversely, if during the diffusion time $t_d = \Delta$, the particles move in the x -direction, then the phase accumulation due to this displacement causes an attenuation of the MR signal. The quantitative measurement of the spin displacement is made by comparison of the measured signal to a reference signal acquired without diffusion gradient pulses.

It is not possible to measure the signal for a single spin, the total measured signal represents the net magnetization for all spins in the imaging voxel. If the spins remain stationary throughout the experiment or if no diffusion gradients are used, the signal is given by

$$S_0 = K \left| \sum_{j=1}^N \mu_j \exp(i\varphi_j) \right|, \quad (2.32)$$

where K is a constant that incorporates various instrumental considerations (e.g. amplifier gain), φ_j is the phase of spin j in the transverse plane, μ_j is its

magnetic moment and the sum is over all spins in the voxel. The net *diffusion weighted* signal therefore becomes (see Eq (2.31))

$$S = K \left| \sum_{j=1}^N \boldsymbol{\mu}_j \exp(i\varphi_j) \exp(i\boldsymbol{\gamma}\mathbf{G} \cdot (\mathbf{r}_j - \mathbf{r}_{0j})\delta) \right|, \quad (2.33)$$

where the vector $\mathbf{r}_j - \mathbf{r}_{0j}$ is the displacement of spin j .

Alternatively, the signal at time Δ can be described in terms of the conditional probability function, $P(\mathbf{r}_0 | \mathbf{r}, \Delta)$, introduced in the previous section, as [64]

$$S(\Delta) = S_0 \int_{-\infty}^{\infty} \int_{-\infty}^{\infty} \rho(\mathbf{r}) P(\mathbf{r}_0 | \mathbf{r}, \Delta) \exp(i\boldsymbol{\gamma}\mathbf{G} \cdot (\mathbf{r} - \mathbf{r}_0)\delta) d\mathbf{r} d\mathbf{r}_0, \quad (2.34)$$

where S_0 represents the initial signal with no diffusion gradients applied and $\rho(\mathbf{r})$ is the spin density. This can also be expressed in q -space formalism as

$$S(\Delta) = S_0 \int_{-\infty}^{\infty} \int_{-\infty}^{\infty} \rho(\mathbf{r}) P(\mathbf{r}_0 | \mathbf{r}, \Delta) \exp(i2\pi \mathbf{q} \cdot (\mathbf{r} - \mathbf{r}_0)) d\mathbf{r} d\mathbf{r}_0, \quad (2.35)$$

where $\mathbf{q} \equiv \boldsymbol{\gamma}\mathbf{G}\delta/2\pi$. For the case of free diffusion $P(\mathbf{r}_0 | \mathbf{r}, \Delta)$ is Gaussian and the net signal loss due to the diffusing spins [64] is given by

$$S(\Delta)/S_0 = \exp(-4\pi^2 \mathbf{q}^2 D\Delta) = \exp[-(\boldsymbol{\gamma}\mathbf{G}\delta)^2 D\Delta] \quad (2.36)$$

In the discussion leading to Eq (2.36) it has been assumed that $\delta \ll \Delta$, however, this condition is seldom realized in practice. Tanner [72] has shown that, for the PGSE sequence, the diffusion time, t_d , (i.e. the time between tagging and detection during which the spins diffuse) is given by $t_d = \Delta - \delta/3$, which clearly reduces to $t_d \approx \Delta$ when $\delta \ll \Delta$. To take into account the diffusion that

occurs during a known finite pulse width, Δ in Eq (2 36) can be replaced by the effective diffusion time $\Delta - \delta/3$ to give [72]

$$S(\Delta) = S_0 \exp\left[-(\gamma G \delta)^2 D \left(\Delta - \frac{\delta}{3}\right)\right] \quad (2 37)$$

Eq (2 36) can be simplified by introducing b which is given by [72]

$$b = (\gamma G \delta)^2 \left(\Delta - \frac{\delta}{3}\right) \quad (2 38)$$

In terms of b , the signal equation becomes

$$S = S_0 \exp[-bD] \quad (2 39)$$

A more general expression for b is derived in the next section

2.3.1.3 Eddy Currents

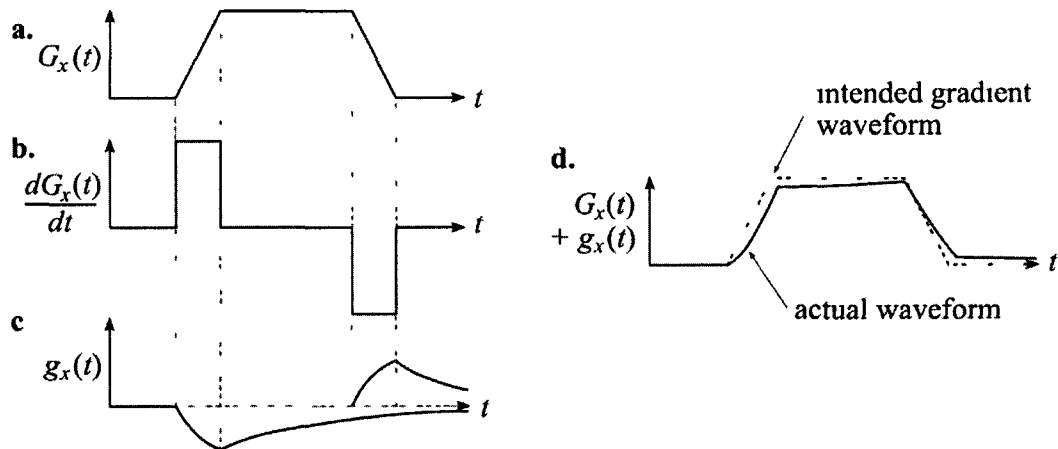


Fig. 2.7. (a) A gradient waveform, $G_x(t)$ (b) The first derivative of the gradient waveform, $dG_x(t)/dt$ (c) One of the induced eddy current terms, $g_x(t)$ (d) The intended and the actual gradient waveforms [98]

Due to the rapidly switching gradients in an MR sequence, the magnetic field in the scanner is constantly changing. These changing magnetic fields induce electrical currents in conducting materials within the scanner. The induced currents are called eddy currents, and result in magnetic field gradients whose direction is opposite to the change in field [82] (see also Figs 2.7b and c). Eddy currents build up during the ramp up and ramp down times of the gradients and decay during stationary phases. The resulting waveform resembles a low-pass filter (Fig 2.7d). B_0 eddy current gradients are spatially constant over the imaging volume.

In our case, diffusion-weighting gradients are very large relative to most gradients used in other imaging sequences. In combination with the EPI readout, which has a low bandwidth in the phase-encoding direction, DWI becomes easily susceptible to eddy current artifacts [82]. Any translation or deformation of the imaging volume can cause the voxel measurements to originate from different physical locations, which sometimes results in unusable images.

By adding an additional refocusing RF pulse into the sequence and adjusting the durations and amplitudes of the gradient pulses appropriately to minimize eddy-current effects, Reese et al [82] were able to develop a sequence that substantially reduces image distortion caused by eddy currents relative to the PGSE sequence.

2.3.1.4 Equations governing the diffusive transport of magnetization

In the laboratory frame of reference Bloch's equation for the magnetization, \mathbf{M} , in a magnetic field \mathbf{B} , with an extra term added to account for isotropic diffusion is [73]

$$\frac{d\mathbf{M}}{dt} = \gamma\mathbf{M} \times \mathbf{B} - \left(\frac{M_x}{T_2} \mathbf{x} + \frac{M_y}{T_2} \mathbf{y} \right) + \frac{(M_0 - M_z)}{T_1} \mathbf{z} + D\nabla^2 \mathbf{M} \quad (2.40)$$

This equation is often referred to as the Bloch-Torrey equation

For the Stejskal and Tanner experiment the spins will be affected by both the static field \mathbf{B}_0 and a linear magnetic field gradient \mathbf{G} . The resulting total field will be

$$\mathbf{B}(\mathbf{r}, t) = \mathbf{B}_0 + \mathbf{G} \cdot \mathbf{r} \quad (2.41)$$

The Bloch-Torrey equation for the complex transverse magnetization m , defined as

$$m(\mathbf{r}, t) = M_x(\mathbf{r}, t) + iM_y(\mathbf{r}, t), \quad (2.42)$$

is given by

$$\frac{dm}{dt} = -i\omega_0 m - \frac{m}{T_2} - i\gamma \mathbf{G} \cdot \mathbf{r} m + D\nabla^2 m, \quad (2.43)$$

where $\gamma B_0 = \omega_0$. The quantity $m(\mathbf{r}, t)$ is not itself a directly observable quantity but rather it is a complex function constructed from the two experimentally determined values, $M_x(\mathbf{r}, t)$ and $M_y(\mathbf{r}, t)$. This complex function is very useful and is used frequently in MRI.

The following substitution is used to formally eliminate the transverse relaxation and signal modulation [73]

$$m(\mathbf{r}, t) = \psi(\mathbf{r}, t) \exp\left(-\left(i\omega_0 + \frac{1}{T_2}\right)t\right), \quad (2.44)$$

resulting in

$$\frac{d\psi}{dt} = -i\gamma \mathbf{r} \cdot \mathbf{G}(t)\psi + D\nabla^2\psi \quad (2.45)$$

If the diffusion term is ignored for the moment, Eq (2.45) is easily solved to give

$$\psi(\mathbf{r}, t) = C \exp(-i\mathbf{r} \cdot \mathbf{k}(t)), \quad (2.46)$$

where C is a constant of integration and

$$\mathbf{k}(t) \equiv \gamma \int_0^t \mathbf{G}(t') dt' \quad (2.47)$$

At $t = 0$, $C = \psi(\mathbf{r}, 0) = m(\mathbf{r}, 0) = M_x(\mathbf{r}, 0) + iM_y(\mathbf{r}, 0)$. But since the reference phase in the rotating frame can be chosen arbitrarily, it can be assumed, without loss of generality, that $M_y(\mathbf{r}, 0) = 0$ and $M_x(\mathbf{r}, 0) = M_0$, which means that $C = M_0$.

If the diffusion term in Eq (2.45) is considered to cause an attenuation of the signal without affecting the phase, a trial solution can be generated from Eq (2.46) by replacing the constant $C = M_0$ with a time dependant function, $M(t)$, which is constructed as the product of M_0 and a real attenuation term. By substituting this trial solution back into Eq (2.45) it can be shown that [73]

$$\begin{aligned} \frac{dM(t)}{dt} &= M(t)D\nabla^2[\exp(-i\mathbf{r} \cdot \mathbf{k}(t))] \\ &= -M(t)Dk(t) \cdot \mathbf{k}(t) \end{aligned} \quad (2.48)$$

The solution to Eq (2.48) at the echo time $t = TE$ is given by

$$M(TE) = M_0 \exp \left[-D \int_0^{TE} k(t) k(t) dt \right] \quad (2.49)$$

$$= M_0 \exp \left[-D \gamma^2 \int_0^{TE} \left(\int_0^{t'} G(t') dt' \right)^2 dt \right] \quad (2.50)$$

To describe the sensitivity of MR sequences to diffusion, a very important quantity, b , the gradient factor, or b -value is defined as

$$b = \gamma^2 \int_0^{TE} \left(\int_0^{t'} G(t') dt' \right)^2 dt' \quad (2.51)$$

By combining Eqs (2.50) and (2.51) the signal attenuation equation becomes

$$S(TE) = S_0 \exp[-bD], \quad (2.52)$$

which is the same as Eq (2.39) derived in the previous section for the PGSE sequence in the limit where $\delta \ll \Delta$ with b given by Eq (2.38). If the diffusion weighting involves a more complicated diffusion gradient design, then Eq (2.51) can sometimes be difficult to evaluate analytically and numerical methods may have to be used. It is important to emphasize that Eq (2.50) is strictly valid only when diffusion takes place in a homogeneous, infinite and isotropic medium. To be rigorous the signal attenuation has to be calculated differently when diffusion is restricted by impermeable barriers or if it is anisotropic.

2.3.2 Apparent Diffusion in Biological Tissues

Discussion to this point has been limited to the case of isotropic free diffusion where water molecules can move equally freely in any direction. The displacement probability in this case depends only on the temperature and

mobility of the molecules and the signal attenuation caused by the diffusing spins is exponential

In biological tissue diffusion is complicated by various interactions and barriers to water movement, including organelle and cell membranes. The water self-diffusion coefficient, D , may be the same in both cases but the measured diffusion coefficient is reduced in tissue. The difference provides information about the cellular microstructure in the vicinity of the water molecules and its ability to hinder and/or restrict the movement of water. To distinguish between these two situations, the term Apparent Diffusion Coefficient (ADC) [74] is typically used to refer to the measured diffusion coefficient in tissues. The ADC describes the mobility of water molecules in tissue and this information can be used to develop insight into tissue microstructure. A further implication of diffusion in tissue is that the displacement probability function can no longer be considered to be Gaussian. The result is that the diffusion signal in biological tissue is not monoexponential, although, for the range of b -values used with DWI in most clinical applications, it is still often a reasonable approximation [75].

Diffusion in the majority of tissue types is reasonably isotropic and measuring the ADC along a single direction is usually sufficient. However, in highly organized tissues such as muscle and white matter, a scalar is no longer adequate to fully characterize the diffusion process. Although some of the early research on diffusion-weighted MRI recognized differences in the ADC along the x , y and z -axes in white matter, these three measurements do not provide enough information to completely describe the diffusion process. Instead of a scalar

diffusion coefficient, a diffusion tensor is required for these anisotropic cases and it becomes necessary to sample the ADC along at least 6 different non-collinear directions to fully characterize this symmetric diffusion tensor

2.3.3 Intravoxel Incoherent Motion Imaging

The structure of the microvasculature of some organs in the body is such that, on the scale of a typical imaging voxel, the flow of blood through the microvasculature (i.e. arterioles, capillaries and venules) can be viewed as being incoherent, pseudo-random motion. A voxel typically contains several thousand capillaries which can be considered to be made up of multiple 'straight' segments oriented at many different angles [74]. Blood flowing through the capillaries can thus be modeled as random, diffusion-like motion characterized by a pseudo-diffusion coefficient, D^* . Blood flow in the microvasculature, viewed in this way, is sometimes referred to in the MR literature as IntraVoxel Incoherent Motion (IVIM) [74]. The value of D^* depends on the vascular geometry of the tissue as well as the rate at which blood flows through the microvasculature of the tissue being investigated and is generally at least an order of magnitude higher than the ADC of the tissue water [74].

2.3.3.1 Intravoxel Motion and MR Imaging

Considering a population, j , of spins in the same voxel moving with an instantaneous velocity, $v_j(t)$, in a magnetic field gradient, $\mathbf{G}(t)$, over a time interval

T , one can define the dephasing, $\delta\phi_j$, for this group of spins as (see also Eq (2 29)) [74,76]

$$\delta\phi_j = \gamma \int_0^T \mathbf{v}_j(t) \cdot \mathbf{G}(t) dt \quad (2 53)$$

An expression for the complex transverse magnetization for the voxel can then be written quite generally in terms of the overall flow related dephasing, Φ , and the amplitude, F , as

$$F \exp(i\Phi) = F \sum_j p(\delta\phi_j) \exp(i\delta\phi_j), \quad (2 54)$$

where $p(\delta\phi_j)$ is the distribution of the dephasings within the voxel of interest

In order to simplify Eq (2 54) it is necessary to introduce some assumptions about the geometry of the microvasculature of the tissue in the voxel and the motion of the spins in the vessels. There are two different microcirculation models to be investigated. Both consider the blood flow in the microvasculature to be microscopically incoherent.

The first model [76] assumes that each $\mathbf{v}_j(t)$ changes many times in the time interval T , such that the displacement for each group of spins in the voxel can be seen as a random walk process. The motion is completely incoherent, in this case, and there is no net dephasing for the voxel but the signal amplitude will be attenuated. This is very much analogous to the diffusion process discussed in section 2 3 1. If the motion is such that $p(\delta\phi_j)$ is Gaussian then, as is the case with diffusion, the motion causes the magnitude of the transverse magnetization to be attenuated by the factor F given by

$$F = \exp(-b D^*), \quad (2 55)$$

where b is the gradient factor defined in section 2.3.1.3. The pseudo-diffusion coefficient, D^* , associated with this process is analogous to the diffusion coefficient for the thermal random motion of the molecules and, it can be shown that (see also Eq (2.28)) [76]

$$D^* = \frac{1}{6} \bar{l}_m \bar{v}_m = \frac{1}{6} \bar{l}_m^2 / \bar{t}_m, \quad (2.56)$$

where \bar{l}_m , \bar{v}_m and \bar{t}_m are the average displacement, average speed and average duration, respectively, for the steps of the random walk process used in the model presented here to represent the motion of the spins in the microvasculature of the voxel. D^* has the same dimensions as a diffusion coefficient (e.g. $\mu\text{m}^2/\text{ms}$) but is usually at least an order of magnitude larger than the ADC for the tissue. The similarities between diffusion and microvascular flow make it possible to use diffusion imaging methods to measure microvascular flow in the tissue as well.

The second model of incoherent microcirculation [76] assumes that the diffusion time is short enough that the spins move with a constant speed and direction in a straight vascular segment during the measurement.

Under these conditions Eq (2.53) becomes

$$\delta\phi_j = \mathbf{v}_j \cdot \mathbf{c} = v_j c \cos \theta_j, \quad (2.57)$$

where

$$\mathbf{c} = \gamma \int_0^T \mathbf{G}(t) dt \quad (2.58)$$

and θ_j is the angle between \mathbf{v}_j and \mathbf{c} (which is parallel to $\mathbf{G}(t)$). The overall effect of these de-phrasings on the MR signal for the voxel can be computed as [76]

$$F \exp(i\Phi) = \int_0^\infty \int_0^{2\pi} \int_0^\pi p(\theta)q(v) \exp(ic v \cos \theta) v^2 \sin \theta d\theta d\varphi dv, \quad (2 59)$$

where θ and v are independent variables and $p(\theta)$ and $q(v)$ are their respective distributions within the voxel F and Φ are defined as the magnitude and phase of this voxel averaged function, which in general will be complex For the special case where the vascular segments are isotropically oriented Eq (2 59) simplifies to

$$F \exp(i\Phi) = 4\pi \int_0^\infty q(v) \frac{\sin(cv)}{cv} v^2 dv \quad (2 60)$$

Note that, since the expression on the right hand side of this equation is real, the signal amplitude is attenuated but there is no overall de-phasing The order of magnitude of the attenuated signal can be estimated by performing numerical calculations using Eq (2 60), assuming $q(v)$ is a Gaussian distribution

When cv is small, Eq (2 60) can be simplified further by using the Taylor expansion to first order for the sinc function to obtain [76]

$$F \approx 1 - \frac{1}{6} c^2 \langle v^2 \rangle, \quad (2 61)$$

where $\langle v^2 \rangle$ is the variance of $q(v)$ defined by

$$\langle v^2 \rangle = 4\pi \int_0^\infty q(v) v^2 dv \quad (2 62)$$

Equating Eq (2 61) with

$$F = \exp(-b D^*) \approx 1 - b D^* \quad (2 63)$$

gives

$$D^* \equiv \frac{1}{6} \langle v^2 \rangle (c^2 / b) \quad (2 64)$$

for the pseudo-diffusion coefficient for the second model

This model of incoherent microcirculation assumes only that the spins move with a constant speed and direction in straight microvascular segments during the measurement and that these segments are isotropically oriented. Note that D^* , as given by Eq (2.64), not only depends on the dynamic properties of the microvascular network (i.e. on v), but it also depends on sequence parameters in a complicated way through the factor c^2/b . Even so, the determination of D^* can give very important insight into properties of the microvascular circulation.

One important consideration when using IVIM is that the flowing component normally represents only a small fraction of the total volume of the voxel (e.g. in the brain). This fraction is expressed as f , the fractional volume of microvascular blood flowing in each voxel and it is equal to the ratio of V_d , the volume of water flowing in the microvascular compartment (i.e. both inside blood cells and in the plasma) to the total volume of water in the voxel, V_{H_2O} .

$$f = V_d / V_{H_2O} \quad (2.65)$$

This quantity is called the active capillary fractional volume or the perfusion fraction.

Inherent to the IVIM model are the following assumptions: 1) there is one voxel compartment where the water molecules diffuse only, 2) there is a second compartment where the water molecules flow and diffuse inside the capillaries and 3) there is no (or at least very slow) exchange between these two compartments. Under these conditions the following expression for the transverse magnetization in the voxel can be used

$$M_{xy} = (1 - f)M(T_{1d}, T_{2d})\exp(-bD) + fM(T_{1c}, T_{2c})\exp(-b(D + D^*)), \quad (2.66)$$

where the subscripts d and c stand for the diffusing only and the circulating components, respectively

The discussion of IVIM presented above suggests that DWI techniques can be made sensitive to blood flowing in the microvasculature of the tissue. When this microcirculation is present, the attenuation of DW images is larger than would be expected from diffusion alone. The effect of microvascular flow is observed as a pseudo-diffusion process and, in this case, the decay is bi-exponential instead of mono-exponential. With the IVIM approach the bi-exponential nature of the decay curve is recognized. This allows for the determination of D , D^* and f , three important fundamental tissue parameters. These IVIM parameters can give more information about the tissue than can the ADC , which is effectively just an average decay constant for the measured diffusion decay which is inherently assumed to be exponential even though this is seldom the case in tissues. The ADC , therefore, has no direct intrinsic physical meaning. The ADC values obtained clinically often depend on the b -values used and either over or underestimate the true diffusion coefficient for water, depending on which part of the diffusion decay that is sampled.

In order to precisely determine the IVIM parameters, acquisitions with many b -values are necessary. The higher range of b -values is related exclusively to diffusion as the signal from the circulating spins has decayed to zero for this part of the decay due to the large amplitude gradients employed and the relatively large displacements involved. The lower range of b -values corresponds to smaller

amplitude gradients and the acquired images for these b -values contain contributions from both diffusion and the microcirculation

Difficulties may arise when IVIM measurements are performed on tissues, such as the brain, where f is small. In this case the diffusion decay must be measured very carefully in order for the regression analysis to be able to reliably determine all three IVIM parameters. Sometimes, when this is the case, a region of interest (ROI) based analysis is preferable to a pixel-by-pixel approach. This, however, is not a problem for either the placenta or the liver studies presented in this thesis since f is relatively large for both of these tissues.

The IVIM model considers the water in the system to be in two distinct compartments, these being the intravascular and extravascular compartments. It also assumes that the water molecules stay in the same compartment for the full duration of the experiment. In this case, the measured diffusion decay will be bi-exponential with the decay constants corresponding to the intrinsic diffusion coefficients of these two compartments. This is known as the slow exchange limit.

However, if the water molecules in fact can move freely between these two compartments and this exchange is very fast on the time scale of the experiment, the spins, on average, will spend an equal amount of time in each of these environments. In this case, the system decays monoexponentially with a rate that represents the weighted average of the intrinsic intravascular and extravascular rates. This is known as the fast exchange limit.

When exchange exists but it cannot be considered either fast or slow for the experiment being considered, this is referred to as intermediate exchange. The

diffusion decay for this case is much more complicated. If this decay is fit to a bi-exponential decay (as is often the case), a quality fit to the data can frequently be found but the two decay constants obtained, in this intermediate exchange case, do not correspond to the intrinsic diffusion coefficients for the two compartments.

2.4. Motion Tracking with Prospective Acquisition Correction (PACE)

For most MRI applications, motion can adversely affect image quality. Some types of motion effects can be corrected for in post processing but ideally the acquisition of data in real time, with good image quality, in spite of motion of (or within) the subject, is preferable. The latest strategy offered on Siemens MR scanners to deal with motion are the inline techniques called 1D-PACE, 2D-PACE, and 3D-PACE. 1D-PACE is ideal for cardiac imaging because it is very fast (30 ms). 2D-PACE is commonly used for abdominal imaging when breathing motion can be problematic. The small flip-angles used in 2D-PACE leave the magnetization in the imaging volume of interest practically undisturbed. 3D-PACE can detect and correct, linear translational and/or rotational rigid body motion in 6 degrees of freedom in real time and is used primarily for motion correction in neurological studies.

In 2D-PACE, the technique used for most of the data acquisition presented in this thesis, a navigator echo module precedes the imaging sequence [77,78]. This module acquires a navigator echo MR signal from a small area defined by an ROI placed on a localizer image by the scanner operator over the object whose motion is to be tracked (see blue box in Fig. 2.8). From this

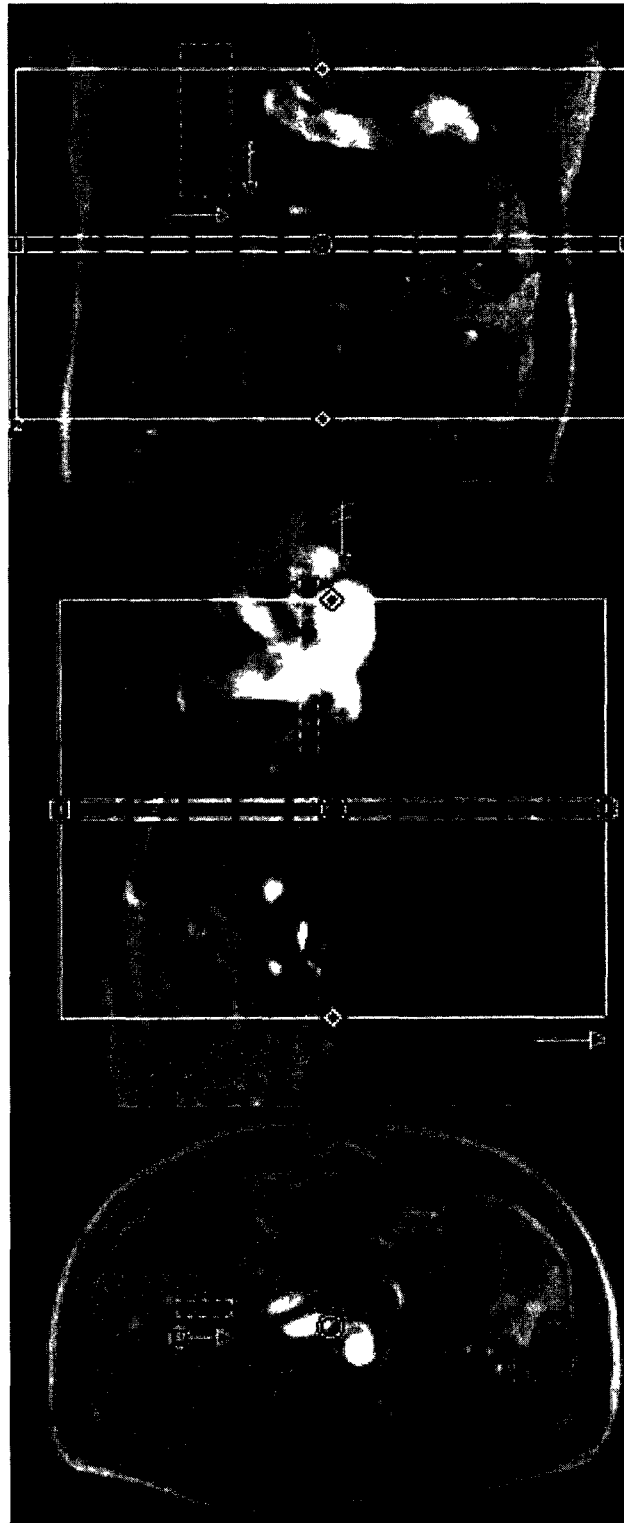


Fig. 2.8. The figure contains a screen capture from the MR scanner showing the location of the navigator echo ROI (i.e. the blue box) positioned over the diaphragm for the 2D-PACE navigator echo respiratory triggering technique. The yellow box indicates the volume that is to be imaged.

signal a 1D projection along the length of the ROI (i.e. the blue box) is generated. Normally, for abdominal imaging, the tracked object is the diaphragm since the weak signal from the lung above and the relatively strong signal from the liver below provide good contrast for tracking the motion of this interface.

The first step in performing image acquisition with 2D-PACE is a training period where the breathing cycle is recorded (Fig. 2.9). No image acquisition is done during this time. The position of the diaphragm is determined by the change in signal intensity along the axis of the ROI. The interface contrast needed between the diaphragm and the lung has to be high in order to allow easy automatic detection.

Once the triggering algorithm has the necessary information, image acquisition begins. 1D projections through the diaphragm are continuously acquired and sent to a respiratory triggering algorithm. When this routine determines that the diaphragm is in the desired location, the imaging sequence acquires the desired number of slices (see Fig. 2.10). However, the image data are only accepted if the position of the diaphragm is found to have been within the acceptance window (set to be ± 2 mm in our protocols) when the data were acquired. The sequence design and the trigger algorithm allow one trigger event per respiratory cycle, with the image acquisition occurring during the end expiration phase.

A low resolution gradient echo sequence (FLASH) with a flip angle of 3° is used in the 2D-PACE navigator echo module. The small flip angle ensures that

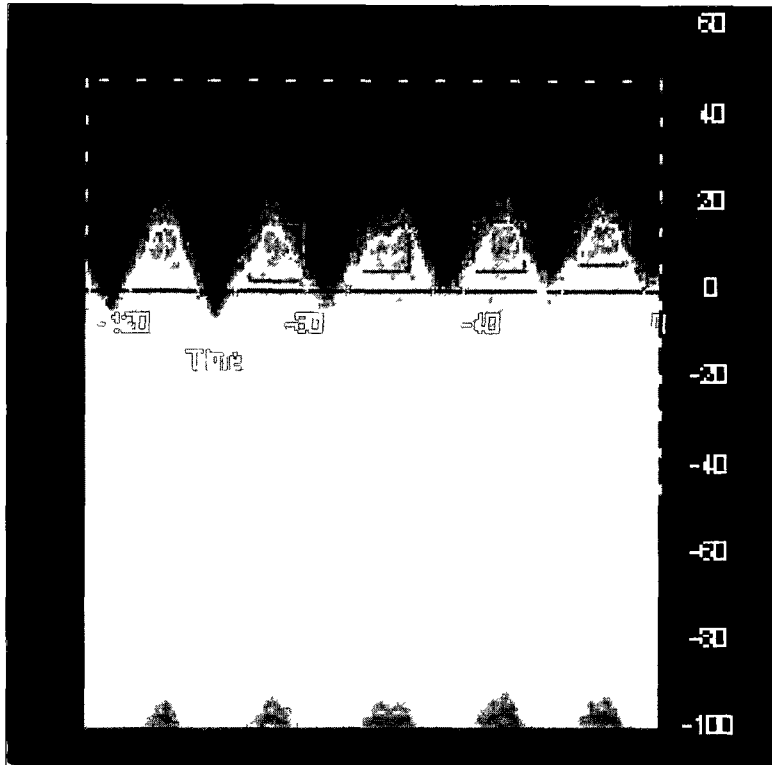


Fig. 2.9. The motion of the diaphragm during free breathing is represented by the green line in this screen capture from the MR scanner. The red boxes depict the acceptance windows that the respiratory algorithm has set for the training period.



Fig. 2.10. The green line represents the motion of the diaphragm during free breathing in this screen capture from the MR scanner. The yellow boxes represent the acceptance windows for image acquisition at the end of expiration.

no magnetization saturation of the tissue of interest occurs (i.e. no saturation stripes from the navigator echo module can be seen in the anatomical images)

The time needed to acquire a navigator echo for 2D-PACE is around 100 ms

The 2D-PACE method, which is unique to Siemens, is very robust and is making free-breathing abdominal MR imaging with very good image quality a clinical reality. The advantages of PACE can be exploited in numerous ways. This technique has greater accuracy than any other form of respiratory gating and no additional hardware is necessary for the imaging protocol.

2.5 Human Placenta

The placenta [79,93,94] is a unique organ that connects the fetus to the uterine wall, plays a vital role in the nutritive, respiratory, and excretory functions of the fetus. The placenta is the one organ that supplies the fetus with oxygen and nutrients and allows fetal residues to be disposed of through the maternal kidneys.

The mature placenta is about 22 cm long and its thickness, which varies from one subject to another, is usually greatest at the center and smaller peripherally. The color is dark reddish-blue or maroon since it contains a lot of blood from both the fetal and maternal hemodynamic systems. Its weight varies as well but, on average, it weighs about 500 g.

The umbilical cord, another very important component of the fetomaternal system, is approximately 55–60 cm in length and contains two arteries and one vein. The umbilical cord connects the placenta to the fetus. The two arteries in the umbilical cord radiate in opposite directions from the attachment of

the cord on the inner surface of the placenta and divide into smaller arteries that go into the depths of the placenta through hundreds of branching and interlacing strands of tissue known as villi. Although there is only one vein in the umbilical cord, it divides into two branches at the surface of the placenta and these branches, like the umbilical arteries, lead to a network of vessels and microvessels that permeates the placenta.

2.5.1 Placenta Development

The development of a new human being begins at fertilization when a sperm cell fuses with an ovum. During the first five days after conception a structure called a blastocyst, which is made up of 70-100 cells, is formed. The blastocyst consists of 1) an aggregation of cells known as the embryoblast that eventually forms the embryo, 2) a fluid-filled cavity and 3) an outer layer of cells known as the trophoblast which surrounds the embryoblast and the fluid-filled cavity. It is the trophoblast that eventually develops into the placenta. As the pregnancy evolves, another layer of cells called the mesoderm forms on the inside surface of the trophoblast. The trophoblast and the mesoderm together form the chorion.

The development of the placenta begins upon implantation of the blastocyst to the uterine wall, the endometrium, and it continues to grow throughout the pregnancy. The outer layer of the placenta forms from the trophoblast which is the outer layer of the blastocyst. This trophoblastic layer of the chorion develops numerous tree-like structures, called chorionic villi, on all

parts of its surface. At the site of implantation, the villi invade and destroy the decidua, a layer of cells lining the uterus, and eventually deeper layers of the endometrium as well. This trophoblastic invasion also disrupts the spiral arteries of the decidua causing blood to flow into the intervillous space of what will become the placenta. Development of the maternal blood supply to the placenta is thought to be complete by the end of the first trimester of pregnancy which is approximately 12–13 weeks after conception. Villi associated with parts of the decidua away from the implantation site degenerate and leave behind smooth chorion. However, the villi at the decidua basalis, that part of the decidua located at the implantation site, increase in number and size. By week 18 of the pregnancy the decidua basalis represents 15-30% of the whole decidua. By the end of the pregnancy over 1 billion microvilli per square centimeter will have formed. Geometrically, the villi are very complex. The branches of the villi can be considered to contain many short randomly oriented capillary sections and blood motion in the villi can be viewed as a random walk process. By the end of the fourth month most, but not all, cells of the decidua basalis have been destroyed, however, the trophoblast continues to invade and erode deeper layers of the endometrium to enlarge the intervillous space. The remaining decidual tissue forms wedge-shaped areas called placental septa that subdivide the placenta into lobules called cotyledons. The mature human placenta consists of 15-20 of these cotyledons with each one containing numerous villi and their many branches. Because septa don't reach the chorionic plate, the fetal side of the

placenta from which the villi originate, the maternal blood in the intervillous spaces can flow between cotyledons

The growth of the placenta parallels fetal growth and, as a result, an approximately constant perfusion fraction is expected throughout the pregnancy. In the third trimester of pregnancy the volume of a single cotyledon, including both the villous and the intervillous space, would typically be about $1 \times 1 \times 2 \text{ cm}^3$. The fractional volume of intervillous space relative to the total villous plus intervillous volume is approximately 0.5.

2.5.2 Blood Circulation in the Placenta

Both fetal and maternal blood flow in the placenta at the same time. The fetal blood passes through blood vessels of placental villi and maternal blood moves through the intervillous spaces. Maternal and fetal blood are separated from each other in the placenta by the villi walls so they do not mix.

There are about 80 to 100 places in the decidua basalis where maternal blood spurts from the spiral arteries into the intervillous space. The maternal blood enters the intervillous space with relatively high pressure and creates a relatively high velocity flow at this entry location. The blood then continues to flow around the villi in the intervillous spaces at a much lower speed, bathing the villi in nutrient rich maternal blood that eventually returns, via the endometrial veins, to the maternal circulation. There is a drop in pressure between the maternal blood entering the intervillous spaces and the blood returning to the venous network which induces the circulation of maternal blood around the villi.

There are about 150 ml of maternal blood in the intervillous spaces, which is exchanged 3 or 4 times a minute. Maternal blood flow is approximately 600–700 ml/min at term.

The fetal blood flows through the microvasculature of the villi. The smallest of these microvessels are capillaries which are only microns in diameter. The fetal blood absorbs oxygen and nutrients from the maternal blood through the walls of the villi, and gives up its waste products in the same manner. This purified, nutrient-enriched blood is carried to the umbilical cord by a network of fetal veins in the placenta, which unite on the surface of the placenta, at the attachment of the cord to form the umbilical vein. In a similar fashion, two umbilical arteries take waste products such as carbon dioxide from the fetus back to the placenta where they are picked up by the maternal blood, the circuit to and from the placenta being thus complete.

Geometrically, the villi are very complex. The branches of the villi are composed of very many short randomly oriented microvascular segments. Consequently, the blood motion in the villi can be viewed as a random walk. This highly vascular structure of the placenta allows the assessment of perfusion in the placenta by use of the IVIM model.

2.6 Human Liver

The liver [79,94] is the largest glandular organ in the body and has many metabolic and secretory functions. It is located in the superior part of the abdominal cavity beneath the diaphragm. Its largest transverse measurement is

from 20.0 to 22.5 cm and weighs about 1.2 to 1.8 kg for an adult liver, depending on the overall body size. Its consistency is that of a soft solid. It is easily lacerated and it has a dark reddish brown color due to its high vascularity.

2.6.1 Structural Anatomy of the Liver

Anatomically, the liver consists of the right, left, caudate, and quadrate lobes. The right lobe accounts for one half to two thirds of the total liver volume. The right and left lobes have equal functionality, even though their sizes may differ significantly. These lobes are divided by a line extending from the inferior vena cava superiorly to the middle of the gallbladder fossa inferiorly. Anteriorly, the right lobe is separated from the smaller left lobe by the falciform ligament. Inferiorly, the caudate lobe is positioned near the inferior vena cava, and the quadrate lobe is adjacent to the gallbladder. The falciform ligament attaches the liver anteriorly to the abdominal wall and superiorly to the diaphragm. The ligamentum teres extends from the falciform ligament to the umbilicus.

2.6.2 Functional Anatomy of the Liver

The liver secretes up to 1,000 ml of bile, a fluid necessary for digestion, every day. A duct system carries bile to the common hepatic duct which connects with both the duodenum of the small intestine, via the common bile duct, and with the gallbladder, via the cystic duct, where it is concentrated and stored. The presence of fat in the duodenum stimulates the flow of bile out of the gallbladder into the small intestine.

Blood is carried to the liver via two large vessels called the hepatic artery and the hepatic portal vein. The hepatic artery carries blood containing oxygen from the aorta. The hepatic portal vein carries blood containing nutrients and xenobiotics extracted from digested food in the small intestine. These blood vessels subdivide in the liver in a tree-like manner, terminating in very small capillaries. Each capillary leads to a lobule. Liver tissue contains thousands of lobules made of hepatic cells called hepatocytes, the basic metabolic unit of the liver. *Microscopically*, each lobule consists of a group of hepatocytes that are approximately polyhedral in shape. They vary in diameter from 12 to 25 μm and contain one, or sometimes two, distinct nuclei. The hepatic cells are arranged in irregular radiating columns between which the blood channels, called sinusoids, can be found. The blood goes through the sinusoids, from the circumference to the center of the lobule, and ends up in the intralobular vein that goes through the center of the lobule. The lobular base is connected to the sublobular vein into which the intralobular vein opens directly. The sublobular veins unite to form larger and larger trunks which end finally in the hepatic veins. There are three large hepatic trunks that unite and open into the inferior vena cava.

Between the hepatocytes there are minute channels called bile canaliculi. These passages are little spaces left between the contiguous surfaces of the cells, and they are always separated from the blood capillaries by at least half the width of a liver cell. The bile, which is secreted by the hepatocytes, is collected in these bile canaliculi. Following the same model as for the blood vessels, the biliary ducts form two main trunks, leave the liver at the transverse fissure and their

union forms the common hepatic duct. The lobules of the liver contain all of the essential components of a secreting gland: cells where the secretion is formed, blood vessels in close proximity to the secreting cells and ducts that collect the secretion and carry it away.

Hepatocytes represent about 60% of the tissue in the liver and perform more metabolic functions than any other cells in the body. The Kupffer cells, also present in the lobule, line the smallest vascular channels and have an important role in blood formation, antibody production and the breakdown and disposal of cellular debris. The liver secretes bile, it stores vitamins, glycogen and other substances, it synthesizes blood-clotting factors, it removes toxins and waste from the blood and it also regulates blood volume and destroys old red blood cells.

The highly vascular structure of the liver, as presented above, allows IVIM to be used to assess perfusion in the liver.

Chapter 3

Using an IVIM Model to Assess the Liver Microvasculature

3.1 Introduction

In this chapter, *in vivo* diffusion weighted (DW) MR measurements on human liver are presented which are sensitive to microscopic motion in biological tissues, including the self diffusion of water molecules and microcirculation of blood in the capillary network of the tissue

Motion related artifacts have limited the usefulness of diffusion weighted imaging (DWI) of abdominal organs and for the evaluation of abdominal pathology in the past. Since DW sequences are designed to be very sensitive to motion, it is challenging to perform artifact-free DWI in the presence of bulk motion due to respiration, peristalsis and blood flow. Nevertheless, a few recent clinical studies have shown that DWI can be successfully used for the diagnosis of liver fibrosis and cirrhosis [9], the detection and characterization of liver lesions [10-28], and the assessment of liver tumor treatment response [34-41]. Most of these studies have used the mono-exponential apparent diffusion coefficient (ADC) model, even though the decay is clearly bi-exponential. Unfortunately, the reported ADC values vary over a very wide range (300% variation) for both normal liver and focal hepatic lesions [42]. There is thus a need for the implementation and validation of more reliable data acquisition techniques and image analysis tools for DWI in the abdomen and, in particular in the liver, the organ that is the subject of this chapter.

It is overly simplistic to assume that the attenuation of the diffusion signal intensity as the *b*-value increases is a simple exponential decay in tissue, particularly in highly vascular tissues such as the liver. Molecular motion causes

a reduction in the signal intensity which is proportional to the displacement of the signal inducing molecules during the measurement. The signal initially (i.e. at low b -values) decays quickly, due to the microcirculation, followed by a slower attenuation, corresponding to diffusion, as the b -value increases. The bi-exponential Intra Voxel Incoherent Motion (IVIM) model is a more realistic approach for vascular tissues and it is the model that will be used in this study to take into account the part of the decay that is sensitive to blood motion in the microvasculature.

To our knowledge there are only two reported IVIM studies of the liver. One of these used a breath hold (BH) protocol [12]. The other employed a free breathing (FB) protocol using a respiratory triggered (RT) sequence where a pneumatic belt was used to generate the trigger pulse [9]. There are no reports of IVIM studies of the liver that used a navigator echo respiratory triggered sequence such as the one used for the work presented in this chapter.

Parallel imaging [44,45] and respiratory triggering [46] have been proposed to improve the image quality and precision of diffusion measurements in the abdomen. Parallel imaging is a relatively new technique for MR signal acquisition that takes advantage of the multiple coil elements in state-of-the-art phased array rf receiver coils. This technology can be used to reduce the acquisition time or increase the number of measurements performed in the same time or a combination of the two. The use of parallel imaging in combination with modern phased array coils leads to a considerable improvement in the quality of the data.

Respiratory triggering synchronizes image acquisition with the patient's breathing cycle in order to avoid motion artifacts and to ensure that the anatomy of interest is at the same location within the FOV for each repetition of the sequence. The use of respiratory triggering allows the acquisition time to be as long as required (i.e. it is not limited to a single breath hold) and removes the patient discomfort associated with breath holding. Respiratory triggering was initially implemented in MRI using respiratory bellows or pneumatic belts which transmit a trigger pulse to the scanner to start image acquisition at the appropriate part of the respiratory cycle and to ensure that, for multi-acquisition protocols, the signals are all acquired for the same part of the respiratory cycle. These methods have largely been replaced by techniques that use navigator echoes to monitor the respiratory cycle by tracking the motion of the diaphragm.

On the Siemens scanner used for the research reported here, Navigator echo Respiratory Triggering (NRT) is referred to as Prospective Acquisition Correction or 2D-PACE. This technique requires no additional hardware and patient set up is much easier. Furthermore, using NRT sequences ensures that the measurement is done with the abdominal organs in the same location for each respiratory cycle. With 2D-PACE, a navigator echo, which is acquired from a small region of interest (ROI) placed perpendicular to the diaphragm, allows the position of the diaphragm to be accurately tracked. The measured diaphragm positions are then passed to a respiratory triggering algorithm. Image acquisition is triggered when the diaphragm is within ± 2 mm of a prescribed location. Image

acquisition is done at the end of expiration and there is one trigger event per breathing cycle. For more details about 2D-PACE see Section 2.4.

The primary aims of the work reported in this chapter were to improve the methodology used for measuring DW images in the liver and to determine the true values for the IVIM parameters (i.e. the diffusion and pseudo-diffusion coefficients and the perfusion fraction) for normal liver tissue *in vivo*. BH and FB protocols were investigated and the obtained IVIM parameters are compared.

For the BH-protocol it was only possible to report on 3 subjects, even though 10 subjects were scanned with this protocol, because of strong chemical shift and/or motion artifacts on many of the images. In spite of the small number of subjects, the results for the BH-protocol were included here for the sake of comparison with the results obtained with the FB-protocol. Although the FB-protocol is far superior, as the results in this chapter clearly show, one potential advantage of the BH-protocol used here is that the initial part of the bi-exponential diffusion decay is better defined since more small b -values were used. Whether or not this is a true advantage will be considered.

3.2 Materials and Methods

3.2.1 Subject Population

This study was approved by the Ottawa Hospital Research Ethics Board. Written informed consent was obtained from all participants. Eighteen volunteers (8 women and 10 men), ranging in age from 17 to 61 years old, were recruited. The analysis presented in this chapter is for 11 volunteers. The first 3 of these subjects

were investigated with a BH-protocol while for the next 8 a FB-protocol, which included a NRT 2D-PACE DW sequence, was used. See Sections 2.4 for a more detailed discussion of 2D-PACE. Images for the other 7 volunteers, all acquired with the BH-protocol, could not be considered for analysis as they were affected either by artifacts or by sudden involuntary motion of the subject. None of the subjects were patients at the hospital, all were volunteers in apparent good health. At the time of imaging, all volunteers were considered to have a normal liver.

3.2.2 MR Technique

MR imaging was performed at the General Campus of The Ottawa Hospital using a 1.5 Tesla (T) Siemens Magnetom Symphony TIM® (Siemens Medical Solutions, Erlangen, Germany) MR system with a maximum gradient strength of 30 mT/m. The first group of subjects were imaged with the BH-protocol on the Siemens Magnetom Symphony Quantum® – Maestro Class system using the torso phased array coil placed anteriorly and elements of the spine phased array coil posteriorly. The second group of subjects were imaged after a significant upgrade to the Siemens scanner which took it from a Maestro Class system to a TIM system. For this second group, the FB-protocol was used. Signal acquisition was done with the torso phased array matrix coil anteriorly and elements of the spine phased array matrix coil posteriorly. For all volunteers, the full protocol consisted of The Ottawa Hospital's routine clinical liver protocol with additional DWI sequences added. An example of an image of a typical healthy liver can be seen in Fig. 3.1.



Fig. 3.1. An image of a healthy liver (slice 11, volunteer 16) A HASTE sequence was used for this acquisition

3.2.2.1 Breath hold protocol

DW images for all b -values and all slices were acquired during a single 30 to 35 s breath hold using a DW single-shot echo-planar-imaging (DW SS EPI) sequence called *ep2d_diff*, with the following parameter settings TR = 2500 ms, TE = 91 ms, 4 to 6 axial 10 mm thick slices were acquired with an interslice gap of 2.5 mm, NEX = 1, FOV = 380 mm, phase FOV = 75%, matrix size = 128x96 and the voxel volume was $3 \times 3 \times 10 \text{ mm}^3 = 90 \text{ mm}^3$. The total imaging time for these DW sequences was 30 to 35 s, depending on the number of slices acquired. Spectral fat saturation was used to suppress chemical shift artifacts. For each slice DW images were obtained for the following 10 b -values 0, 10, 20, 30, 50, 90, 150, 300, 500 and 800 s/mm^2 . The diffusion gradients were applied in the slice selection direction (head-to-foot) in all cases. With this protocol the number of

slices that could be acquired was limited by the subject's ability to hold his or her breath resulting in incomplete liver coverage

The DW SS EPI sequence provided by Siemens with the scanner is restricted to b -value increments of 50 s/mm^2 . To make the sequence more appropriate for IVIM measurements, the sequence was modified to allow for smaller b -values by changing the increment from 50 s/mm^2 to 10 s/mm^2 . This was done using source code and the IDEA sequence programming environment, both provided by Siemens under a research agreement

A water phantom at room temperature was used to validate the IVIM DW imaging sequence used with the BH-protocol. A monoexponential signal decay with a decay constant of $D = 2.00 \pm 0.06 \text{ } \mu\text{m}^2/\text{ms}$ was obtained. This result is in very good agreement with the reference diffusion coefficient for water of $D = 2.0 \text{ } \mu\text{m}^2/\text{ms}$ at 22°C [80]

3.2.2.2 Navigator echo respiratory triggered free breathing protocol

With the FB-protocol it was possible to image the entire liver. DW images were acquired with a DW SS EPI sequence called *ep2d_diff_p2_trigg*, using 2D-PACE and the following parameter settings: TR varied from 3,267 to 4,209 ms (depending on the respiratory cycle of each subject), TE = 94 ms, eighteen 10 mm thick axial slices were acquired with an interslice gap of 2.5 mm, NEX = 1, FOV = 380/400 mm (women/men), phase FOV = 75%, matrix size = 144x192, iPAT-GRAPPA reduction factor = 2, and the imaging time required for the 13 b -values and 18 slices was 124 s (note that GRAPPA is Siemens acronym for parallel

imaging performed in k-space) The total image acquisition time was between 3 and 4 minutes depending on each volunteer's respiratory cycle With this protocol the voxel volume was $2 \times 2 \times 10 \text{ mm}^3 = 40 \text{ mm}^3$ and $2 \times 1 \times 2 \times 1 \times 10 \text{ mm}^3 = 44 \text{ mm}^3$ for women and men, respectively, and the number of slices that could be acquired was not limited by the subject's ability to hold his or her breath which allowed for complete liver coverage For each slice, 13 DW images were obtained with b -values of 0, 50, 100, 150, 200, 250, 300, 350, 400, 450, 500, 650 and 800 s/mm^2 The diffusion gradients were applied in the slice selection direction (head-to-foot) in all cases Spectral Adiabatic Inversion Recovery (SPAIR) fat suppression was used to avoid chemical shift artifacts

3.2.3 Image Analysis

Data analysis was based on the IVIM model [76], which considers water diffusion and blood microcirculation to be separate processes with slow exchange between these two compartments (see also Section 2.3.3) The signal decay for this model is biexponential

$$S / S_0 = (1 - f) \exp(-bD) + f \exp(-bD^*) \quad (3.1)$$

where S is the measured DW signal, S_0 is the $b = 0$ signal, D and D^* are the diffusion and pseudo-diffusion coefficients, respectively, and f is the perfusion fraction, which represents the fractional volume occupied in the voxel by MR visible spins moving in the capillaries of the tissue D^* , which is sometimes also called the perfusion coefficient, is related to the displacement of water molecules in the microvasculature of the tissue during the measurement

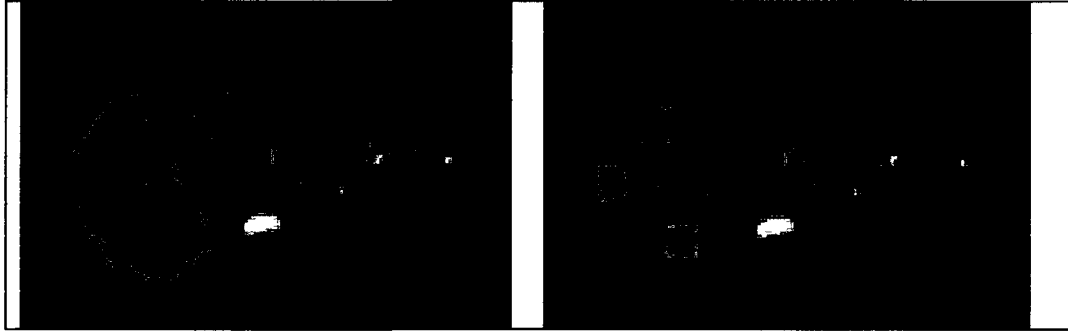


Fig. 3.2. The whole right side of the liver (WRL) ROI is shown in red and the periphery of the right side of the liver (PRL) ROIs are shown in blue. All ROIs have been drawn on anatomical images for a healthy liver (volunteer 16)

Analysis was performed in the same manner for both the BH and FB protocols. Three square 100-pixel ROIs were investigated for each slice of the liver (see Fig. 3.2). The mean and standard deviation (SD) of the pixel intensities was computed for each ROI and the mean values were used to generate the diffusion decays. The ROIs were drawn peripherally in anterior, mediolateral and posterior regions of the right lobe of the liver, with larger blood vessels being avoided as much as possible. The decay was biexponential for all ROIs investigated for both protocols (see, for example, Fig. 3.3). The Levenberg-Marquardt nonlinear least-squares method was used to fit the decays to Eq. 3.1 to obtain values for the IVIM parameters, D , f and D^* . The values plotted in the graphs represent the parameter values obtained for each ROI averaged over all slices for each volunteer.

Another ROI, which we call the periphery of the right lobe (PRL) ROI is generated from the union of these three square 100-pixel ROIs. The inclusion of this ROI is justified and discussed further below.

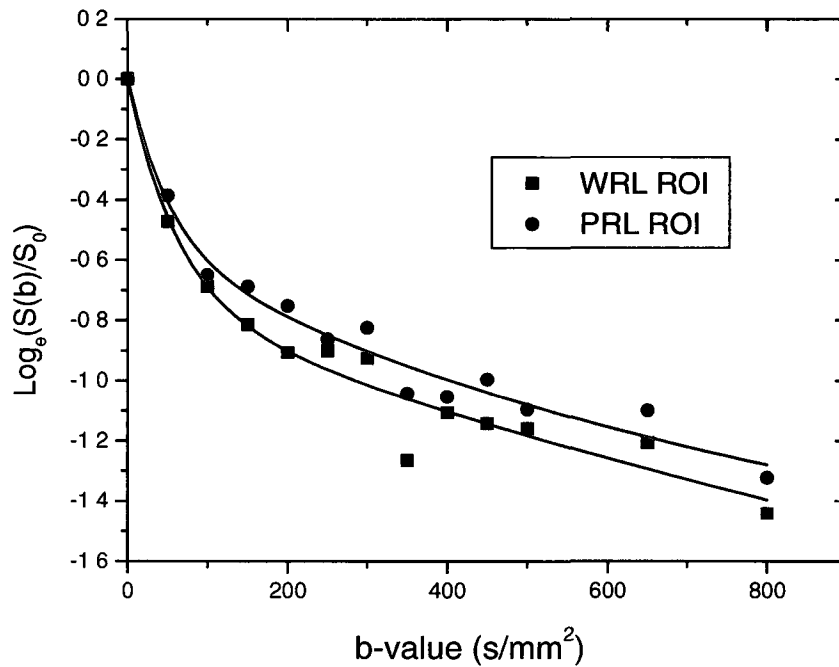


Fig. 3.3. Typical diffusion decays for the WRL-ROI (black) and the PRL-ROI (red) (volunteer 16)

Separately, for each slice, a large ROI was drawn to encompass as much of the right lobe of the liver as possible (see Fig 3 2) The mean and SD of the pixel intensities were computed for this whole right liver (WRL) ROI and the mean values were used to generate diffusion decays which were again bi-exponential The Levenberg-Marquardt nonlinear least-squares method was used to fit the decays to Eq 3 1 to obtain values for D , f and D^* The graphs in Figs 3 5 to 3 7 show the IVIM parameter values obtained for each WRL-ROI averaged over all slices for each subject D , D^* and f maps were also calculated on a pixel-by-pixel basis for this WRL-ROI using a Levenberg-Marquardt fit to Eq 3 1

These maps were overlaid in colour onto the corresponding $b = 0 \text{ s/mm}^2$ anatomical images (see Fig 3 4)

All image analysis was performed using software written in the MRI lab at the Ottawa Hospital using IDL (ITT Visual Information Solutions, Boulder, CO)

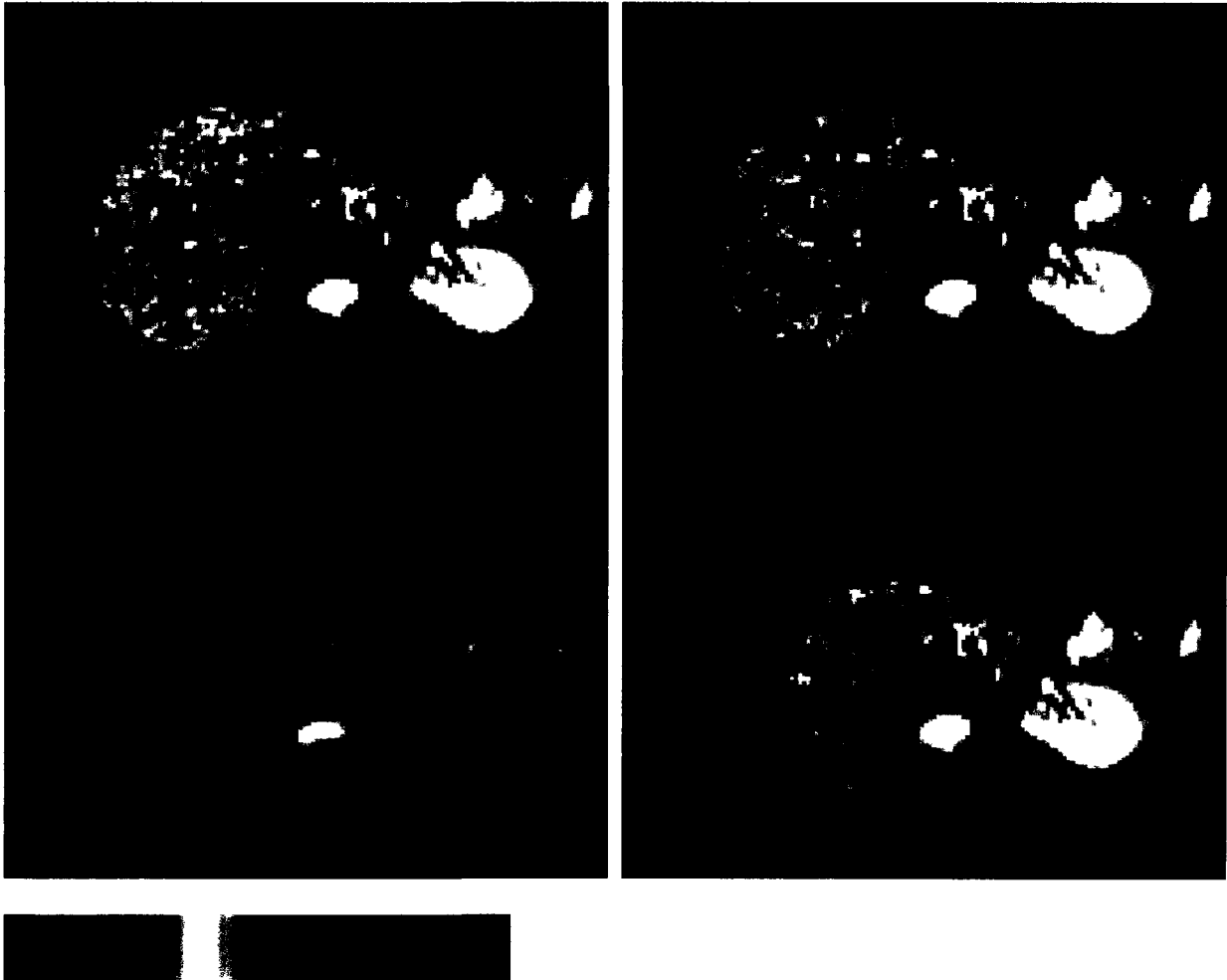


Fig. 3.4. An anatomical image for a normal liver (slice 19, volunteer 16) is shown on the lower left and f (upper left), D (upper right) and D^* (lower right)-maps color overlaid onto the anatomical image, are shown as indicated. The color table ranges for the maps are 1) 0 – 100% for the f -map, 2) (0 – 2) $\mu\text{m}^2/\text{ms}$ for the D -map and 3) (0 – 200) $\mu\text{m}^2/\text{ms}$ for the D^* -map

3.3 Results

DW images were obtained for 11 volunteers 3 with the BH-protocol and 8 with the FB-protocol using a NRT-DW sequence Only the right hepatic lobe was evaluated It was not possible to perform reliable analyses of the other lobes due to motion artifacts caused by cardiac motion

The presence in the images of chemical shift artifacts from fat in the abdominal wall was a significant problem for the BH-protocol, even though spectral fat saturation was used to suppress the fat signal These artifacts were observed in all BH-subjects and this precluded quantitative investigation for most of the slices In total 10 subjects were scanned with this protocol but only 3 data sets could be used Furthermore, the analysis had to be limited to 4 slices for each of these 3 subjects due to the presence of artifacts in the outer slices

With the NRT-DW sequence, fat signal suppression was done using the SPAIR technique with far better results compared to the fat saturation technique used with the BH-protocol Chemical shift artifacts and/or motion artifacts were observed in just a few of the subjects investigated, however, these artifacts, if they were seen at all, were not problematic since they were present only on the first slices of the acquisition - slices that did not contain any of the liver

Diffusion decays were generated using the mean values calculated over the corresponding ROI for each b -value In all cases the diffusion decay was clearly bi-exponential The decays did not need rectified noise bias correction since the signal-to-noise ratio (SNR) for the highest b -values (i.e. lowest signal) was always greater than 3:1 for the images obtained with the BH-protocol and

greater than 7.1 for the FB-protocol. For the $b = 0$ images the SNR was typically about 9.1 or higher for the BH-protocol and 24.1 for the FB-protocol. The decays were fit to Eq. 3.1 as described above for both breathing protocols and the values of D , f , and D^* were obtained for 3 square 100-pixel ROIs located in anterior, mediolateral and posterior positions of the liver's right lobe and for the WRL-ROI.

All statistical analyses were done using ROIs. SPSS software was used for statistical computations. All ROI distributions were assumed to be normal for these initial analyses and therefore the means and standard deviations of the data were reported. A t -test was used to compare the means between WRL-ROI and PRL-ROI as well as with values reported in the literature. Not having the literature data in our possession, we could not be sure of the form of the distributions but we made the assumption that their data are also normally distributed. Mean comparison tests were performed and a two-sided asymptotically significant p -value was reported in all cases. Statistical significance was defined as $p < 0.05$. However the assumption of normality was re-examined in a secondary analysis by calculating the skewness and kurtosis for the data sets and by performing a Shapiro-Wilk test of normality. With this secondary analysis, it was found that the D^* parameter distributions did not obey the condition of normality and a Mann-Whitney non-parametric test was therefore used in these cases. These results are found in Appendix A.

No consistent systematic changes of the IVIM parameters were observed with slice position for any of the subjects or ROIs considered. For some of the

subjects there was an indication of an interslice variation for some of the parameters but this trend could not be discerned beyond experimental error. Therefore, the values in all of the tables and figures of this chapter are averaged over all slices.

The IVIM parameter values for the three 100-pixel ROIs showed excellent intra-subject agreement, both within the same slice and across slices, for each subject and for both breathing protocols (see Figs 3.5 to 3.7 and Tables 3.1 to 3.3). The scatter for D^* was a little bit larger but no systematic changes were observed. This good agreement suggests that the IVIM parameters are the same for the regions of the right lobe investigated with the square 100-pixel ROIs and, by extension, to all peripheral areas of the right lobe. With this result as justification, the IVIM parameters were also computed as the mean over the 3 intra-slice 100-pixel ROIs and over all slices. These mean values are labeled as the PRL-ROI values in the figures and tables of this section where PRL stands for Periphery of the Right Lobe.

The results obtained with the WRL-ROI also showed excellent intra-subject agreement for each slice and for both breathing protocols. Thus, the values reported here are again averaged over all slices. The results for the WRL-ROI also agree very well with the results from the 100-pixel ROIs and the PRL-ROI.

Table 3.1. Mean D , D^* , and f values for the right side of the liver for the FB-protocol

IVIM Parameter	WRL-ROI	CV	PRL-ROI	CV
D ($\mu\text{m}^2/\text{ms}$)	1.10 ± 0.16	0.15	1.06 ± 0.22	0.21
D^* ($\mu\text{m}^2/\text{ms}$)	46 ± 17	0.37	45 ± 19	0.42
f (%)	44.0 ± 6.9	0.16	42.3 ± 8.8	0.21

Note: Data are reported as mean \pm SD and CV, the coefficient of variation, is defined as SD/mean

Table 3.2. Mean D , D^* , and f values for the right side of the liver for the BH-protocol

IVIM Parameter	WRL-ROI	CV	PRL-ROI	CV
D ($\mu\text{m}^2/\text{ms}$)	1.13 ± 0.22	0.19	1.04 ± 0.28	0.27
D^* ($\mu\text{m}^2/\text{ms}$)	70 ± 19	0.27	67 ± 50	0.75
f (%)	34 ± 11	0.32	29 ± 12	0.41

Note: Data are reported as mean \pm SD and CV, the coefficient of variation, is defined as SD/mean

Table 3.3 Mean D , D^* , and f values for the right side of the liver for the FB-protocol when a t -test was performed, and a two tailed p -value is reported

IVIM Parameter	WP-ROI (N = 8)	PRL-ROI (N = 8)	p -value
D ($\mu\text{m}^2/\text{ms}$)	1.10 ± 0.16	1.06 ± 0.22	0.238
D^* ($\mu\text{m}^2/\text{ms}$)	46 ± 17	45 ± 19	0.937
f (%)	44.0 ± 6.9	42.3 ± 8.8	0.437

Note: Data are reported as mean \pm SD (if p -value < 0.05 , then results are statistically different)

3.3.1 Perfusion Fraction

The variation of f for the 100-pixel ROIs, the PRL-ROI and the WRL-ROI, averaged over all slices in each case, is shown in Fig. 3.5. For both breathing protocols there is very good intra-subject agreement. For the FB-protocol there is also very good inter-subject agreement for the f values for all ROI types. The mean f value, averaged over all FB subjects, for the WRL-ROI, $f = (44.0 \pm 6.9)\%$, is in very good agreement with the mean value calculated for the PRL-ROI, $f = (42.3 \pm 8.8)\%$. For the FB-protocol, all but one value fell within one SD of the

mean calculated for this group of subjects, the exception being the WRL-ROI value for volunteer 7. Since all subjects were apparently healthy, it is not clear why this one value was lower than the rest. Results in the literature have shown that exercise and/or fasting changes the blood volume in liver, exercise actually decreasing it [96]. We did not record if the subjects were fasting or have exercised before the scan, so we cannot make any assumption on this matter.

Although there is very good inter-subject agreement for the FB-protocol, this is not the case for the BH-protocol where the f value for volunteer 2 is considerably higher than it is for the other two, especially for the WRL-ROI. However, the value obtained for volunteer 2 appears to be in better agreement with the FB-protocol results than the other two, suggesting that this may be the more reliable value. The mean f -value calculated for the PRL-ROI (29 ± 12)% is in good agreement with the value calculated for the WRL-ROI (34 ± 11)% with the BH-protocol. The observed variation is within the reported measurement error although, since only 3 subjects were scanned for this data set, the standard deviation calculated over the group of 3 subjects may not be a good representation of the true experimental error.

There is an appreciable difference between the f values obtained with the two breathing techniques under investigation (see Tables 3.1 and 3.2). The f values obtained with the FB-protocol are much larger than the f values obtained for volunteers 1 and 3 with the BH-protocol, however, the value obtained for volunteer 2 is in good agreement with the other two subjects. The variance is also much lower for the FB-protocol. For the WRL-ROI, the coefficient of variation

(CV) is 0.32 for the BH-protocol whereas it is only 0.16 for the FB-protocol – showing more precise results. The situation for the PRL-ROI is similar, with CV values of 0.41 and 0.21 for the BH and FB protocols, respectively.

It should also be noted that the inclusion of smaller b -values for the BH-protocol does not appear to have improved the precision of the f values obtained with this technique. This is not surprising since f is determined primarily by the large b -value part of the decay.

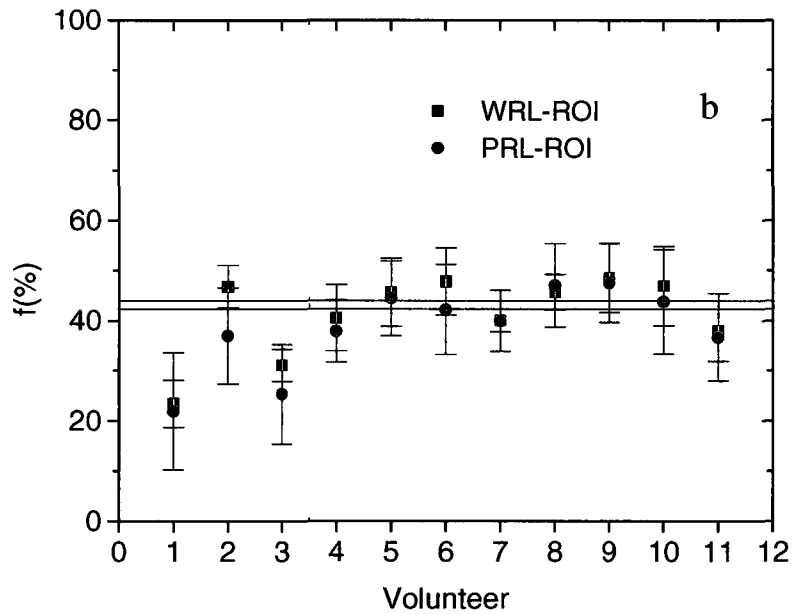
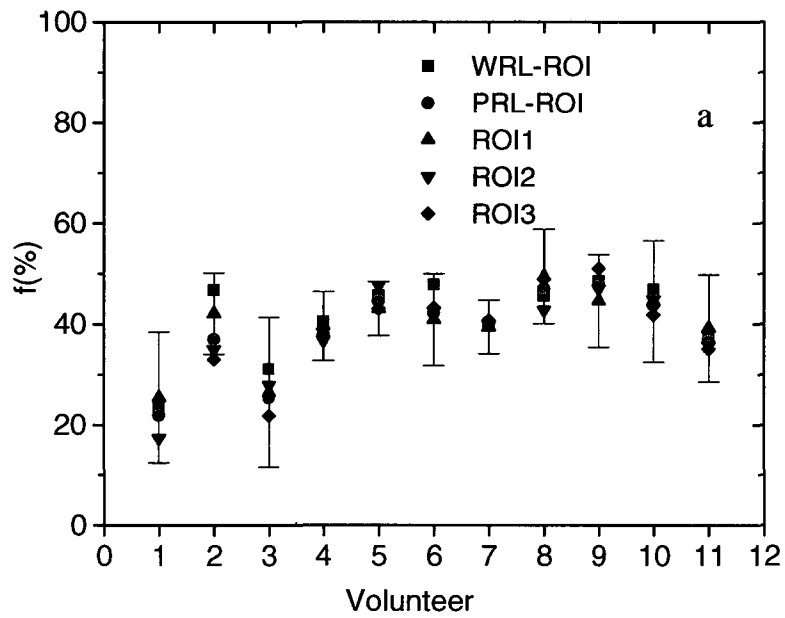


Fig. 3.5. f values (mean \pm SD) are shown for the WRL-ROI, the three 100-pixel ROIs and the PRL-ROI, averaged over all slices in each case. The BH-protocol was used for volunteers 1 to 3 and the FB-protocol was used for volunteers 4 to 11. The horizontal lines show the mean over all volunteers scanned with the FB-protocol for the PRL-ROI (red) and the WRL-ROI (black). For clarity, error bars are shown in a) for ROI1 only.

3.3.2 Diffusion Coefficient

The variation of D for the 100-pixel ROIs, the PRL-ROI and the WRL-ROI, averaged over all slices in each case, is shown in Fig 3 6 For both breathing protocols there is very good intra-subject agreement The average over all subjects for the BH-protocol gave a mean diffusion coefficient of $D = (1.13 \pm 0.22) \mu\text{m}^2/\text{ms}$ for the WRL-ROI and $D = (1.04 \pm 0.28) \mu\text{m}^2/\text{ms}$ for the PRL-ROI For the FB-protocol we obtained $D = (1.10 \pm 0.16) \mu\text{m}^2/\text{ms}$ for the WRL-ROI and $D = (1.06 \pm 0.22) \mu\text{m}^2/\text{ms}$ for the PRL-ROI The data also showed good inter-subject agreement for both breathing protocols The values for all but one subject fell within one SD of the mean for the protocol, the exception being the WRL-ROI value for volunteer 5 Since all subjects were apparently healthy, it is not clear why this one value was higher than the rest

No significant difference was observed between the D values for the WRL-ROI and the PRL-ROI with the FB protocol and a similar behaviour was observed for BH breathing protocol (see p -values in Table 3 3) The WRL value was higher than the PRL value for all subjects, however, the D values for these two ROIs were all within one SD of each other (Fig 3 6b) While the D values obtained with the two breathing protocols are in very good agreement, it should be noted that there is a 25-30% improvement in the precision when the FB-protocol is used (see Tables 3 1 and 3 2) For the WRL-ROI, CV equals 0.19 for the BH-protocol whereas it is only 0.15 for the FB-protocol The situation for the PRL-ROI is very similar with CV values of 0.27 and 0.21 for the BH and FB protocols, respectively

The 100-pixel ROI analysis showed that D does not vary significantly within a slice as long as the ROI positioning is carefully done so as to avoid large blood vessels. This conclusion is supported, for both breathing protocols, by the D -maps, an example of which is shown in Fig. 3.4 (upper right). This is the expected behaviour since D is not related to the microcirculation in the tissue, D is governed by tissue structure. Diffusion dominates the higher range of b -values on the decay, where capillary blood flow effects do not contribute.

The inclusion of smaller b -values for the BH-protocol does not appear to have improved the precision of the D values obtained with this technique. This is not surprising since D is determined primarily by the large b -value part of the decay.

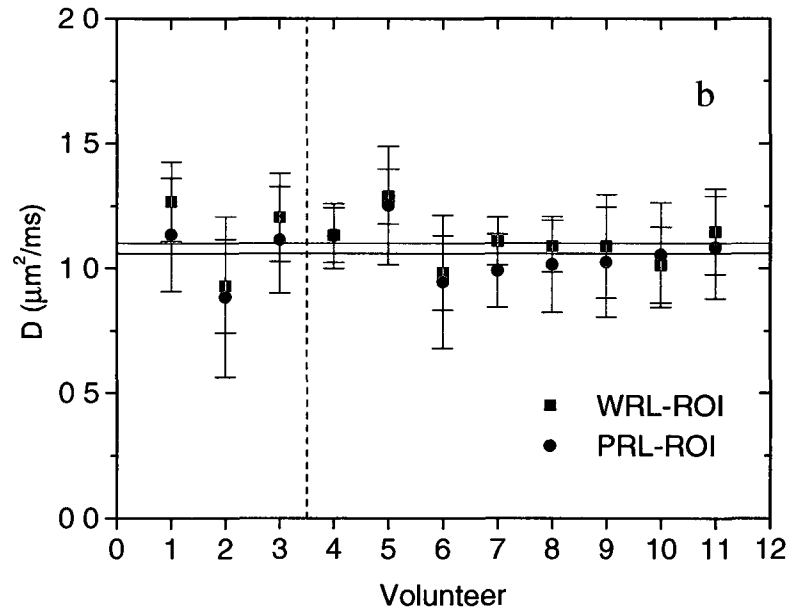
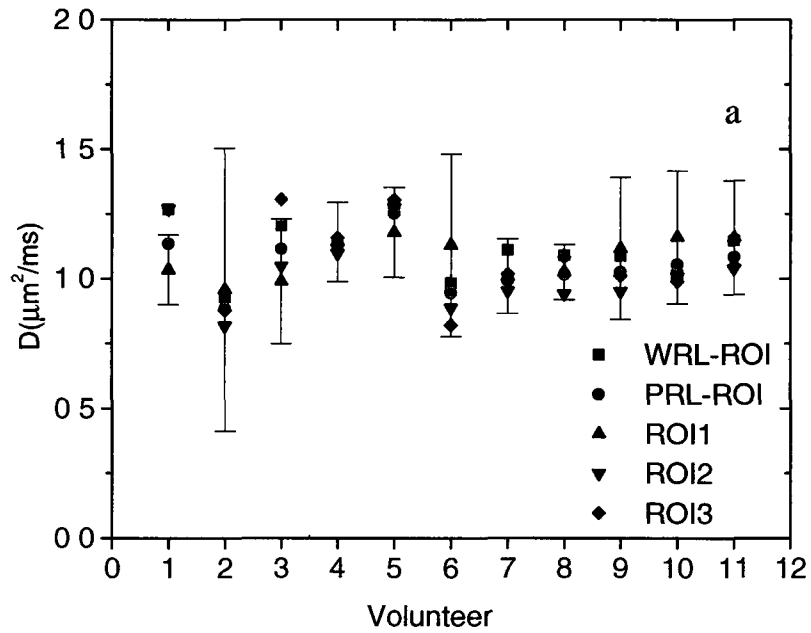


Fig. 3.6. D values (mean \pm SD) are shown for the WRL-ROI, the three 100-pixel ROIs and the PRL-ROI, averaged over all slices in each case. The BH-protocol was used for volunteers 1 to 3 and the FB-protocol was used for volunteers 4 to 11. The horizontal lines show the mean over all volunteers scanned with the FB-protocol for the PRL-ROI (red) and the WRL-ROI (black). For clarity, error bars are shown in a) for ROI1 only.

3.3.3 Pseudo-Diffusion Coefficient

The variation of D^* for the 100-pixel ROIs, the PRL-ROI and the WRL-ROI, averaged over all slices in each case, is shown in Fig 3 7 For both breathing protocols there is good intra-subject agreement For the FB-protocol, the values of D^* , averaged over all subjects, were $D^* = (46 \pm 17) \mu\text{m}^2/\text{ms}$ and $D^* = (45 \pm 19) \mu\text{m}^2/\text{ms}$ for the WRL-ROI and the PRL-ROI, respectively The corresponding values for the BH-protocol were $D^* = (70 \pm 19) \mu\text{m}^2/\text{ms}$ and $D^* = (67 \pm 50) \mu\text{m}^2/\text{ms}$, respectively The values obtained with these two ROIs are in very good agreement for the same breathing protocol

The data showed good inter-subject agreement for both breathing protocols, particularly for the FB-protocol (see p -values in Table 3 3) All but one value fell within one SD of the group mean, the exception being volunteer 1 for the BH-protocol when the PRL-ROI was considered Since all volunteers were apparently healthy, it is not clear why this one value was higher than the rest

There is a notable difference between the D^* values obtained with the two breathing techniques (see Tables 3 1 and 3 2) The three D^* values for the BH-protocol are all higher than the D^* values for the FB-protocol The variance is also much higher for the BH-protocol For the PRL-ROI, the coefficient of variation (CV) is 0 75 for the BH-protocol whereas it is only 0 42 for the FB-protocol – a very significant improvement The situation for the WRL-ROI, however, is reversed with CV values of 0 27 and 0 37 for the BH and FB protocols, respectively The elevated CV value for the FB-protocol, in this case,

may reflect the expected variation in the microvascular blood flow pattern across the liver rather than increased experimental error

The inclusion of smaller b -values for the BH-protocol does not appear to have improved the precision of the D^* values obtained with this technique. This is a bit surprising since D^* is determined primarily from the low b -value part of the decay. Presumably, errors due to other problems with the BH-protocol cancel out any gain in precision from these additional low b -value points

The variation of D^* across the liver on the color parametric maps (Fig 3 4d) is consistent with the anatomy of the liver. Areas with higher D^* values can be seen around larger blood vessels ~ brighter areas on Fig 3 4 (lower left), where, since they are collecting or spreading blood, a higher blood flow is expected (see Section 2 6 for a review of the anatomy of the liver and its hemodynamic hierarchy) and a constant behaviour is observed for the rest of the liver

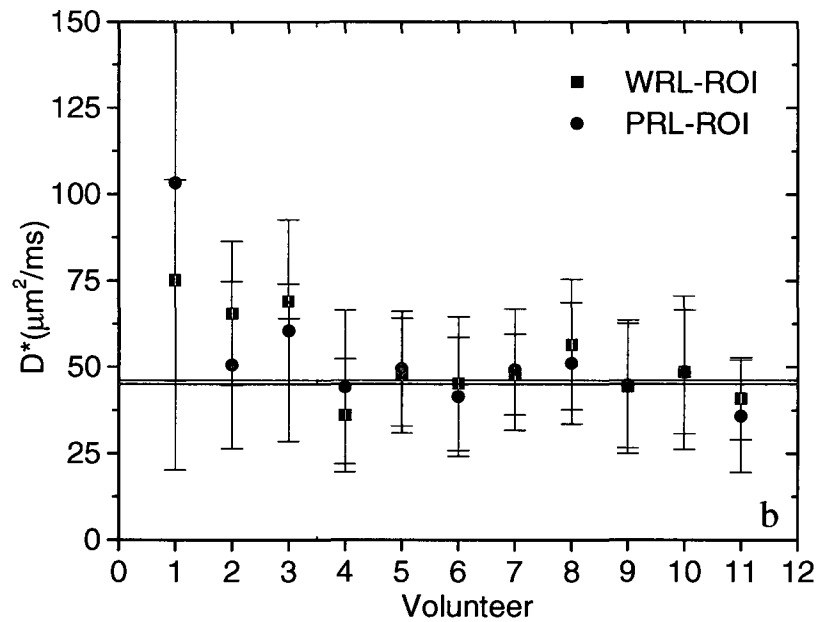
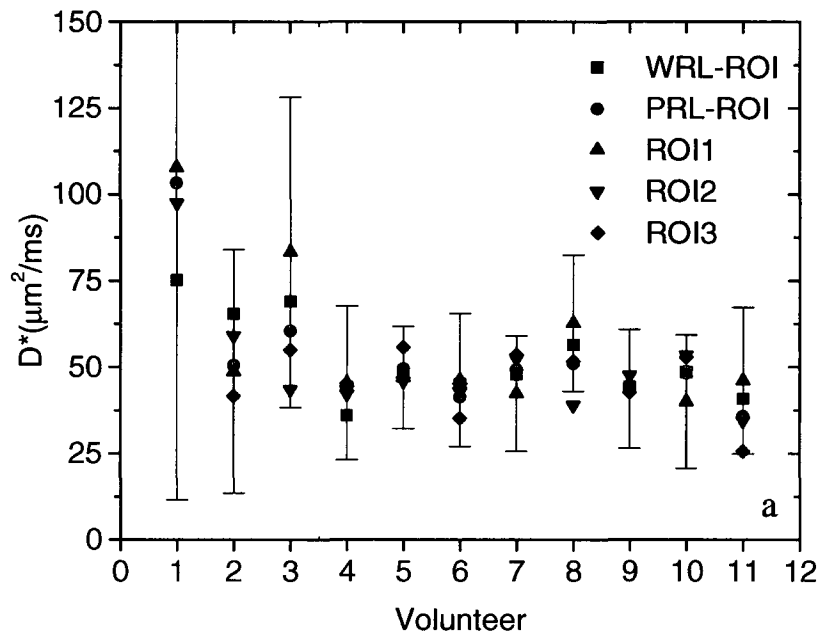


Fig. 3.7. D^* values (mean \pm SD) for the WRL-ROI, the three 100-pixel ROIs and the PRL-ROI, averaged over all slices in each case. The BH-protocol was used for volunteers 1 to 3 and the FB-protocol was used for volunteers 4 to 11. The horizontal lines show the mean over all volunteers scanned with the FB-protocol for the PRL-ROI (red) and the WRL-ROI (black). For clarity, error bars are shown in a) for ROI1 only.

3.4 Discussion

In this chapter the movement of blood in the microvasculature of the liver, including arterioles, capillaries and venules, was investigated using the IVIM model [5] and an assessment of the values of the fit parameters f , D and D^* was made. The active microvascular fractional volume, f , also known as the perfusion fraction, represents the ratio of the volume of MR visible water moving in the microvascular compartment (e.g. water in blood cells, plasma, etc.) to the total volume of MR visible water present in the voxel. The pseudo-diffusion coefficient, D^* , is the exponential decay constant for the MR signal attenuation induced by the displacement of water in the microvasculature. The capillaries in the liver are assumed to follow a pseudo-random course such that motion of the microvascular water can be described in terms of a random walk model. Macroscopically (i.e. on the scale of a typical voxel), this motion appears very much like a diffusion process. Thus, f is a measure of how much water is present in the microvasculature of the tissue and D^* is related to the speed of the circulating blood and the length of the randomly oriented capillary segments [76]. For the size of the voxel investigated in our studies (90 mm^3 with the BH-protocol and 40 mm^3 and 44 mm^3 for women and men, respectively, with the FB-protocol) a very large number of randomly oriented arterioles, venules and capillary segments are to be expected to exist in a single voxel (see Section 2.6 for a review of liver anatomy and physiology).

Many hepatic pathologies cause changes to the microvasculature of the liver. With fibrotic disease the vascularity of the tissue decreases whereas with

cancer, angiogenesis causes increased vascularity at the site of the lesion. The values of f and D^* can be expected to change accordingly and should be sensitive indicators of these forms of hepatic pathology. Moreover, accurate values of these IVIM parameters should indicate the degree to which the microvasculature has been affected by the pathology and could be specific for certain hepatic pathologies [95]. In this thesis we present values of these parameters for healthy liver tissue. Deviations from these values in patients can be expected to be an indication of the presence of disease. Further study is required to determine the sensitivity and specificity of the IVIM parameters but the work presented here is an important first step.

The diffusion coefficient, D , is not related to microcirculation in the tissue. It is related to the ability of the extravascular water (i.e. intracellular and interstitial water) to diffuse [66]. This, in turn, is determined primarily by the cellularity of the tissue. The diffusion coefficient can be expected to decrease, relative to normal liver, in fibrotic tissue, where the fibres presumably inhibit diffusion, and in cancerous lesions where cell crowding restricts diffusion. Reliable quantitative values for D should be sensitive to the presence of pathology in hepatic tissue but it is unclear if it will be a useful parameter for discriminating between different pathologies. Further study is required to answer this question.

In the work presented here, two different breathing protocols (breath hold and free breathing) were used and the obtained IVIM parameter values were compared. For each of these methods, ROIs were chosen in three distinct ways: 1) three 100-pixel square ROIs were placed at locations around the periphery of

the right hepatic lobe (anteriorly, mediolaterally and posteriorly) to sample different locations within the liver, 2) a ROI which we call the periphery of the right lobe (PRL) ROI was formed from the union of the 3 100-pixel ROIs (see Section 3.3 for justification) and 3) a large ROI was selected to cover as much of the right hepatic lobe as possible. The diffusion decays were generated from the means of these ROIs for each b -value. Components of the signal decay corresponding to water that is diffusing only and water that is both circulating and diffusing in the microvasculature were identified for all ROI choices and both breathing protocols. These DWI measurements provide noninvasive quantification of water diffusion and blood circulation in the microvascular network of liver tissue *in vivo*.

Parametric maps were also generated for the WRL-ROI for each of the IVIM parameters. The distribution of the parameter values across these maps was, in general, rather uniform, however, there was a recognizable pattern with both f and D^* which is consistent with the composition of the liver tissue. The f -maps (see Fig. 3.4 upper left) show a clear gradient from smaller values near larger blood vessels (which can be seen as brighter areas in Fig. 3.4 lower left), to larger values in peripheral regions where capillary density is higher. Major blood vessels are consistently depicted in the f -maps as either a small blue region or a blue ring around a white spot. The D^* -maps (see Fig. 3.4 lower right) showed elevated values at locations in and around larger blood vessels where blood flow is expected to be higher. The D -maps (see Fig. 3.4 upper right) showed a small variation of values across the liver but this variation does not appear to be

correlated with liver anatomy or physiology. It is more likely simply a reflection of the range of D values that can be expected for such a measurement.

These parametric maps show great promise as visual tools for the radiologist but they do not lend themselves to easy quantitative analysis so they will not be considered further in this chapter. Instead we decided to concentrate our efforts on region of interest analyses.

One potential deficiency of the study is that the diffusion sensitivity gradients were only applied in the inferior-superior direction. It would have been nice to measure the diffusion in other directions as well. However this would have extended the exam time considerably and, given the composition of the liver, a directional dependence of the IVIM parameters was not anticipated.

3.4.1 Comparison of the IVIM Parameters for Different ROIs

The results obtained with the WRL-ROI for different slices were in good agreement, both within the same slice and across slices (i.e. low intra-subject variation), for both breathing protocols. Thus, the values reported here are the average over all slices. This behavior is also apparent in the IVIM parametric maps, as noted above. The intra-subject agreement for each subject with the three 100-pixel ROIs was also good, for both breathing protocols and all three IVIM parameters. This suggests that the IVIM parameters are the same for the peripheral regions of the right lobe of the liver investigated and, by extension, to all peripheral areas of the right lobe. This observation validates our use of the PRL-ROI.

To within the experimental error of the measurements presented here, the same IVIM parameter values are obtained for the PRL-ROI and the WRL-ROI, even though the positioning of the three 100-pixel ROIs was done very carefully to avoid large vessels while no such precaution was taken for the ROI drawn to encompass the whole right lobe. Presumably the explanation for this is that in the larger WRL-ROI there is a relatively small proportion of the total number of voxels which contain large vessels, with the consequence that these vessels have a relatively small effect on the diffusion decay for this ROI. These vessels would likely have an important effect on smaller ROIs (e.g. 100 pixels), where fewer pixels are involved in the computation of the mean, but not on ROIs as large as the WRL-ROI.

It should be noted that the reported range of WRL-ROI IVIM values, particularly f and D^* , is determined partly by experimental error and partly by changes in the composition of the liver tissue at different locations within the ROI. The observed smaller SD found for all parameters with the WRL-ROI suggests that experimental error is the dominant contribution in each case since the number of pixels in the WRL-ROI from which the mean and SD were calculated is much larger than 300 pixels and the larger tissue variation across the WRL-ROI relative to the PRL-ROI would cause SD to increase, not decrease. For these reasons and the fact that, based on the measurements reported here, the IVIM parameters are the same (to within experimental error) for all parts of the right lobe of the liver, the WRL-ROI appears to be a better, more robust choice (See Table 3.3)

3.4.2 Breath Hold Protocol versus Free Breathing Protocol

The agreement between the results obtained with the two breathing protocols was acceptable in that the agreement was within experimental error. However, the BH-protocol and/or data set had numerous deficiencies. These include 1) strong chemical shift and motion artifacts on many of the source images, 2) a small sample size of only 3 subjects, 3) uncertainty regarding voxel position from one measurement to the next, 4) large variances for both individual experiments and across the group of subjects, 5) the number of slices acquired and the number of b -values used were both limited and signal averaging could not be employed since the image acquisition time was restricted to a single breath hold and 6) the scanner hardware used for the experiments was not state-of-the-art.

The images acquired with the FB-protocol, which were obtained after the scanner was upgraded to state-of-the-art equipment, were far superior to those acquired using the BH-protocol, all of which were obtained prior to the upgrade. Chemical shift and motion artifacts were not apparent on the images acquired on the upgraded scanner. It was also possible to use NRT sequences after the upgrade to give increased confidence that the voxels were at the same location for each measurement. This option was not available on the older system.

The intra-subject variance of the data was larger for the BH-protocol than it was for the FB-protocol mainly because the hardware used for the BH experiments was not as good and NRT sequences were not used. The upgraded scanner allowed us to use the SPAIR fat suppression technique which provides far

better fat suppression. This removed the chemical shift and motion artifact problem. We also obtained better SNR due to superior rf coil technology. Reasons for the small number of subjects for the BH-protocol include 1) this protocol had to be stopped after the MR scanner was upgraded and 2) the results for 7 of the 10 subjects scanned with this protocol had to be rejected due to strong chemical shift and motion artifacts in the images. It is gratifying that the results of these two protocols are in agreement to within experimental error but the FB-protocol is clearly far superior.

One of the disadvantages of performing the imaging during a breath hold is that it restricts the duration of the scan to about 30 s or less. This limits the number of slices that can be acquired and/or the number of averages and b -values that can be used. Furthermore, for the BH-protocol, even though the subject is holding his or her breath, this does not guarantee that the abdominal organs will remain stationary during a scan, particularly towards the end of the scan when it becomes more difficult for the subject to maintain the breath hold. Inaccurate reproducibility of the breath hold for successive scans may also lead to changes in the location of the abdominal organs from one measurement to the next. These issues are considerably reduced (if not completely eliminated) when a navigator echo is used to accurately track the motion of the diaphragm while the patient breathes normally and comfortably.

The BH-protocol used for the work reported in this chapter did, however, have one potential advantage over the FB-protocol since it was possible to use smaller b -values with the BH-protocol. The DWI product sequence provided by

Siemens allows an increment in the b -values of 50 s/mm^2 . Prior to the upgrade we were able to modify this increment to 10 s/mm^2 , under a research agreement with Siemens. This allowed the use of b -values between 0 and 100 s/mm^2 that were multiples of 10 s/mm^2 instead of 50 s/mm^2 . However, following the upgrade, a new research agreement with Siemens was not in place in time to allow the incorporation of this sequence modification into the FB-protocol used here. Such a change to the protocol should have little or no effect on the values of D and f obtained since these parameters are determined primarily by the behaviour of the large b -value part of the decay (i.e. they are related to the slope and y-intercept, respectively, of the long component when plotted on a semi-logarithmic plot). However, inclusion of smaller b -values into the protocol could improve the precision, of the D^* values obtained since this is the part of the decay that is most affected by the microcirculation.

The intra and inter-subject variability for all IVIM parameters, including D^* , is higher for the BH-protocol suggesting that the deficiencies of the protocol and the hardware used for these measurements outweigh the benefit of having small b -values. Another factor that contributed to the reduced intra-subject variance for the FB-protocol was the fact that, since it was possible to acquire more slices with this protocol, there were more slices available to include in the computation of the mean and SD. With the BH-protocol it was only possible to get 4 slices whereas with the FB-protocol the number of slices ranged from 6 to 10, depending on the size of the subject's liver. It seems reasonable that the

addition of more b -values between 0 and 100 s/mm^2 would improve the FB-protocol but the results presented here do not support or refute this assumption

The reduced number of slices for the BH-protocol also means that it was not possible to cover the whole right lobe of the liver. Thus, for the BH-protocol, the average over all slices gives, in principle, values that reflect the average for the slices measured and not necessarily the right lobe as a whole. Although variation of the IVIM parameters from slice to slice was found to be relatively small for healthy liver, this may not be the case with diseased tissue. In this case, coverage of the whole liver may be a vital requirement for the protocol.

Overall, the FB-protocol appears to be far superior to the BH-protocol. However, the mean D^* values obtained with the BH-protocol are in better agreement with values reported in the literature. This will be discussed in more detail below.

For the FB-protocol the results showed good inter-subject agreement for all parameters. All but two values fell within one SD of the mean for this group of subjects, the exceptions being the WRL-ROI D -value for volunteer 5 and the WRL-ROI f -value for volunteer 7. Since all subjects were apparently healthy, it is not clear why these values were higher and lower, respectively, than the rest. The inter-subject variability for the FB-protocol was considerably better than for the BH-protocol. This can be seen by inspection from the figures in Section 3.3 and from the CV values given in Tables 3.1 and 3.2. It should also be noted that the variation of the SD from subject to subject was much smaller for the FB-protocol than it was for the BH-protocol.

If the inter-subject variability for the BH-protocol is determined using the mean and SD for the group of 3 subjects then all parameters fell within one SD of the mean. However, this is probably not a fair test since, with such a small number of subjects, data points that should be outliers will have a strong enough effect on the computed SD that they may not be seen as outliers. If the average SD for the individual measurements is considered instead, then it can be seen, by inspection, that all of the PRL-ROI values are approximately within one SD. In other words, there is an overlap of the range of values determined by the error bars for the individual experiments (see Figs 3.5 to 3.7).

For the WRL-ROI values the ranges determined by the error bars for D and D^* again overlap for all three subjects but for the f values, where the error bars are much smaller, none of the values overlap.

These observations suggest that the inter-subject variability for the BH-protocol is acceptable for all parameters (except possibly f for the WRL-ROI) but this has to be tempered by the fact that the experimental errors for the BH measurements were relatively large for all values (except f for the WRL-ROI). The inter-subject variability for the BH-protocol is reasonable but it is considerably worse than for the FB-protocol.

From the accuracy point of view, the perfusion fraction values that we obtained are close to the blood volume in liver which is believed to represent about 30% of the total hepatic volume. The arterial system acts as a buffer in maintaining the intrahepatic pressures, but the blood volume will vary as a

function of these pressure gradients. The values we obtained for f for both breathing protocols are shown in Table 3.1 and Table 3.2 [96,97].

3.4.3 Comparison with IVIM Parameter Values in the Literature

To our knowledge, there are only two other studies that have investigated the IVIM parameters for the liver. These studies both used a SS EPI DW sequence but they used different breathing protocols. Yamada et al. [12] used a BH technique while Luciani et al. [9] used a FB technique with a pneumatic belt for respiratory triggering. There have been no reports of IVIM studies of the liver where an NRT sequence was used, and there were no studies that report IVIM parameters on whole right liver. During the writing of the thesis one paper [95] was published where an NRT sequence and a similar method were used. However, the data analysis and the fitting procedures are different from ours.

A comparison of the IVIM parameters from these studies with the values reported here is given in Tables 3.4 and 3.5. Unfortunately, neither of these reports provided values for all of their experimental parameters, making a direct comparison with our work difficult.

Table 3.4. IVIM parameter values for the right side of the liver measured with our FB-protocol compared with those obtained by Luciani et al [9] using a pneumatic belt RT sequence

IVIM Parameter	WRL-ROI (N = 8)	CV	PRL-ROI (N = 8)	CV	Luciani et al ~13-pixel ROI (N = 37)	CV
$D (\mu\text{m}^2/\text{ms})$	1.10 ± 0.16	0.15	1.06 ± 0.22	0.21	1.16 ± 0.9	0.78
$D^*(\mu\text{m}^2/\text{ms})$	46 ± 17	0.37	45 ± 19	0.42	85.1 ± 27	0.32
$f (\%)$	44.0 ± 6.9	0.16	42.3 ± 8.8	0.21	26 ± 7	0.27

Note: Data are mean \pm SD. Our mean values were obtained by averaging over all subjects for both the WRL-ROI and the PRL-ROI.

Table 3.5 IVIM parameter values for the right side of the liver measured with our BH-protocol compared with those obtained by Yamada et al [12] using their BH-protocol

IVIM Parameter	WRL-ROI (N = 3)	CV	PRL-ROI (N = 3)	CV	Yamada et al 100-pixel ROIs (N = 47)	CV
$D (\mu\text{m}^2/\text{ms})$	1.13 ± 0.22	0.19	1.04 ± 0.28	0.27	0.76 ± 0.27	0.36
$D^*(\mu\text{m}^2/\text{ms})$	70 ± 19	0.27	67 ± 50	0.75	Not reported	-
$f (\%)$	34 ± 11	0.32	29 ± 12	0.41	29 ± 14	0.48

Note: Data are mean \pm SD. Our mean values were obtained by averaging over all subjects for both the WRL-ROI and the PRL-ROI.

Table 3.6 Mean IVIM parameter values averaged over the right side of the liver (Ottawa) and the Luciani [9] data, when a t-test was performed, and a two tailed p -value is reported

IVIM Parameter	Luciani (N = 11)	WP-ROI (N = 8)	p -value (Luciani vs WP-ROI)	PRL-ROI (N = 8)	p -value (Luciani vs WP-ROI)
$D (\mu\text{m}^2/\text{ms})$	1.16 ± 0.9	1.10 ± 0.16	0.8554	1.06 ± 0.22	0.7637
$D^*(\mu\text{m}^2/\text{ms})$	85.1 ± 27	46 ± 17	0.0022	45 ± 19	0.0023
$f (\%)$	26 ± 7	44.0 ± 6.9	0.0001	42.3 ± 8.8	0.0003

Note: Data are reported as mean \pm SD (if p -value $<$ 0.05, then results are statistically different)

Table 3.7. IVIM parameter values for the right side of the liver measured with our FB-protocol compared with those obtained by Patel et al [95] using an NRT sequence

IVIM Parameter	WRL-ROI (N = 8)	CV	PRL-ROI (N = 8)	CV	Patel et al (N = 14)	CV
$D (\mu\text{m}^2/\text{ms})$	1.10 ± 0.16	0.15	1.06 ± 0.22	0.21	1.17 ± 0.21	0.18
$D^*(\mu\text{m}^2/\text{ms})$	46 ± 17	0.37	45 ± 19	0.42	39.61 ± 12.34	0.31
$f (\%)$	44.0 ± 6.9	0.16	42.3 ± 8.8	0.21	32.16 ± 8.13	0.25

Note: Data are mean \pm SD. Our mean values were obtained by averaging over all subjects for both the WRL-ROI and the PRL-ROI.

It is important to mention that, for both of the breathing techniques employed in our measurements, the precision of the f and D values (based on the CV values given in Tables 3.4 and 3.5) is significantly higher than for the previously reported studies and it is comparable for D^* . This significant improvement we believe to be due primarily to the superior methodology employed in our study.

3.4.3.1 The IVIM study of Yamada et al.

Yamada et al. [12] studied the application of the IVIM technique to several abdominal tissues including both normal liver and hepatic lesions. They used a breath hold SS EPI DW technique, with TE = 123 ms, a slice thickness of 8 mm and a set of only 4 b -values (0, 30, 300 and 900 s/mm²). The number of investigated slices was not reported. They obtained bi-exponential diffusion decays and used IVIM theory to analyse the results. The Levenberg-Marquardt nonlinear least-squares algorithm was used to fit the decay and obtain the IVIM parameters, f , D and D^* , although no D^* values were reported. The parameters for normal liver were evaluated as the average over 47 subjects and over 3 or 4 circular ROIs containing at least 100 pixels per subject. No information is given about the positioning of the ROIs so it is unclear if they attempted to avoid large vessels or if they restricted their investigation to a particular lobe of the liver.

The reported mean \pm SD values for their IVIM parameters for healthy subjects are $D = (0.76 \pm 0.27) \mu\text{m}^2/\text{ms}$ and $f = (29 \pm 14)\%$ where their reported SD values were calculated over the group of subjects and are considered by them

to be a measure of the inter-subject variability. These values are considerably lower than our values obtained with the FB-protocol but, given the large errors reported by Yamada et al, they are not inconsistent. Yamada's f value, however, agrees reasonably well with our BH-protocol f value.

There are several important deficiencies of the study reported by Yamada et al relative to our FB study. These include 1) the scanner hardware, although possibly state-of-the-art when the experiments were performed in about 1998, is considerably inferior to the state-of-the-art equipment used for our study, 2) they only used 4 b -values - this is not enough to properly characterize a noisy bi-exponential decay, 3) they used a BH-protocol instead of a protocol with a NRT sequence and 4) they report that the DW images used in the study were degraded by chemical shift and motion artifacts. Given these deficiencies and the large reported errors, the values reported by Yamada et al for the IVIM parameters are not considered to be reliable.

3.4.3.2 The IVIM study of Luciani et al.

Luciani et al [9] investigated the IVIM parameters with a respiratory triggered technique that uses a pneumatic belt to track the motion of the abdominal wall externally. The MR sequence is triggered to start image data acquisition when a specific pressure is detected by the belt. This is an outdated method for performing respiratory triggering that has largely been replaced by the use of navigator echoes at sites that have this capability. Triggering with the pneumatic belt has three primary deficiencies relative to triggering with navigator echoes 1)

it is less sensitive to motion, 2) tracking the motion of the diaphragm (using navigator echoes) gives better reproducibility for the positioning of the abdominal organs with normal breathing, 3) the pneumatic belt must be secured fairly snugly around the patient's abdomen, 4) with the pneumatic belt the patient must be coached to breathe in a very regular fashion throughout the exam. Consequently, there is a higher probability that the measurements performed for a given DW experiment will not all correspond to the same voxel when a pneumatic belt is used for respiratory triggering, navigator echo triggering is much less sensitive to all of these issues.

For the imaging sequence that we used, a navigator echo signal is obtained from a ROI placed perpendicular to the diaphragm. This signal is used to track the location of the diaphragm. The measured diaphragm positions are then passed to a respiratory triggering algorithm. Image acquisition is initiated when the diaphragm is at a prescribed location. The image acquisition is done during the end of the expiration phase, and there is one trigger event per breathing cycle. See Section 2.4 for further details.

Luciani et al. obtained the value of D by performing a linear fit to the high b -value part of the decay, assuming that this part of the decay follows a single exponential decay function. The estimation of f and D^* was done using a nonlinear regression algorithm based on the Nelder-Mead Simplex method with the value for D fixed to the previously determined value. This simplex method often encounters problems with local minima [81]. The analysis was performed on a pixel-by-pixel basis to generate parametric maps for f , D and D^* . ROIs were

then positioned on these parametric maps and the mean values for the ROIs were reported. Two ROIs were placed in the right lobe and one in the left lobe but, unfortunately, the authors do not specify where within the right and left lobes these ROIs were located. They observed no significant variation in the parameters between the right and left lobes. The average ROI size was 12 ± 3 pixels with a range of 10 to 16 pixels. They comment in their paper that it was difficult to determine where major vessels were on their parametric maps.

Luciani et al report a D value of $(1.16 \pm 0.9) \mu\text{m}^2/\text{ms}$ for a group of 25 patients. This is in good agreement with our values, averaged over 8 subjects, of $D = (1.10 \pm 0.16) \mu\text{m}^2/\text{ms}$ for the WRL-ROI and $D = (1.06 \pm 0.22) \mu\text{m}^2/\text{ms}$ for the PRL-ROI. Although the mean D values are in very good agreement, the precision is much higher in our study, thanks to the superior methodology employed. The CV value for their study is 0.78 whereas it is only 0.15 for the WRL-ROI and 0.21 for the PRL-ROI data in our study – a very significant improvement. Their D^* values are considerably different from ours but, given their large quoted errors, they are not inconsistent. Their f value is significantly lower than ours (see p -values for significant statistical differences in Table 3.6 for all three parameters investigated).

Although the approach used by Luciani et al is much better than that used by Yamada et al there are still some important deficiencies that make their reported IVIM parameter values questionable. The use of a pneumatic belt for respiratory triggering does not provide good reproducibility of abdominal organ positioning for the images, as described in more detail above. Navigator echo

triggered respiratory gating is a far better approach. However, a bigger concern is the method they used for their analysis. According to their paper they obtained their D values by fitting the data for the highest 2 b -values to a simple exponential decay. In the absence of noise this approach should be perfectly valid. However, since they did a pixel-by-pixel analysis for signals from relatively small voxels (20 mm^3), with a moderately large TE of 70 ms and only a small amount of signal averaging (NEX = 3), the diffusion decays were likely very noisy. Although they do not report the SNR for their DW images, they do show a typical decay for normal liver in their Fig. 1 and it is clear that the data are indeed quite noisy. This no doubt explains why they report such a large error for D . Thus, the values that they report for D must be considered questionable. By comparison, we generate our diffusion decay from the mean of at least 100 pixel values so that the SNR for our decay is much higher than theirs and we have 8 of these high SNR data points (for the FB-protocol) in the large b -value part of the decay. Moreover, the questionable D values that they report are used as input to the simplex algorithm used to get f and D^* so that the values reported for these parameters are also suspect.

It may appear contradictory to claim that our D -value is reliable but the value reported by Luciani et al. is suspect when the two values are very close ($(1.10 \pm 0.16) \mu\text{m}^2/\text{ms}$ and $(1.16 \pm 0.90) \mu\text{m}^2/\text{ms}$, respectively). However, we believe this agreement to be coincidental. Given their large error, their D -value is compatible with values between $0.26 \mu\text{m}^2/\text{ms}$ and $2.06 \mu\text{m}^2/\text{ms}$, a huge range of values. To investigate this further we transcribed the diffusion decay shown in

Fig 1 of their paper as best we could and performed a bi-exponential fit to the data. We obtained a very convincing fit with the parameters $f = 0.46$, $D = 0.73 \mu\text{m}^2/\text{ms}$ and $D^* = 38 \mu\text{m}^2/\text{ms}$. This value for D is very different from their quoted mean but compatible with our BH-value and the value reported by Yamada et al. The f and D^* values from this fit are also very different from the values reported by Luciani et al. but they are in good agreement with the values that we report for the FB-protocol. Although we only analysed one of their decays, and our approach was rather crude, the results can be taken as additional confirmation that the values reported by Luciani et al. are not reliable.

Our data analysis procedure employed a more consistent approach in which 1) 3 equivalent 100-pixel ROIs were drawn peripherally (anterior, lateromedial, posterior areas of the right lobe of the liver) on anatomical images taking care to avoid regions containing large vessels and 2) a large ROI was drawn to cover the whole liver. We report values averaged over all slices for both the PRL-ROI and for the WRL-ROI. Because the NRT-DW sequence used did not limit the imaging time or, as a consequence, the number of slices that could be acquired, it was possible for us to investigate the whole right lobe of the liver.

The results obtained with the WRL-ROI and the 100-pixel ROIs revealed that there are no large deviations in the IVIM parameters for the areas of the liver that were investigated. Even so, it should be recognized that, while part of the variance for the experiments reported here is related to experimental error, part of it will also be due to small changes in the tissue from one area of the liver to another, as can be seen in the parametric maps, and from one subject to another.

Patel et al [95] reported in 2010 a preliminary experience where IVIM and DCE are used alone and/or in combination to study its utility in diagnosing liver cirrhosis diagnosis. In their study, the IVIM parameters were investigated with a similar technique to ours. The data were acquired on a 1.5 T Siemens MR scanner and the diffusion protocol is similar to our imaging protocol as well. However, the image analysis is different, segmented b₁-exponential fitting being used in their approach. Even though the fitting procedures and statistical analysis tools used were different in the two studies, the values that we obtained for the IVIM parameters were similar to theirs, although our precision was at times better (see CV values in Table 3.7).

3.5 CONCLUSION

By using a better imaging technique and a superior approach to the data analysis we were able to perform more accurate and precise IVIM parameter quantification compared with other studies reported in the literature [9,12]. We also showed that a free breathing protocol using a navigator echo respiratory triggered protocol is far superior to a breath hold protocol for measuring the IVIM parameters in the liver. Moreover, this is the first study where a whole right lobe ROI was investigated and thus we can report, for the first time, average IVIM parameter values for the whole right hepatic lobe.

The IVIM parameters discussed in this chapter were studied in four different ways: 1) with an ROI that covered the whole right lobe of the liver (i.e. the WRL-ROI), 2) with 3 separate square 100-pixel ROIs located around the

periphery of the right lobe of the liver, 3) with an ROI that consisted of the union of the three 100-pixel ROIs (i.e. the PRL-ROI) and 4) with a pixel-by-pixel analysis from which parametric maps were generated. The parametric maps clearly showed changes in f and D^* between central and peripheral locations, consistent with blood flow patterns in the liver. It was, therefore, expected that differences in the WRL-ROI and PRL-ROI IVIM parameter values would also be found. While such a trend was suggested by the data, the effect was fairly subtle and could not be resolved beyond experimental error. It was, therefore, concluded that there is no advantage to carefully positioning several smaller ROIs to avoid major blood vessels and that the use of a WRL-ROI is a better approach.

IVIM parameters evaluated with a navigator echo free breathing protocol have significant potential as both sensitive and specific parameters for the detection and diagnosis of hepatic disease. The improved methodology and the accurate IVIM parameter values for normal liver tissue presented in this chapter both represent significant advancements and are an important first step toward the use of IVIM parameters in MRI studies of the liver. The IVIM parametric maps, which showed good anatomical detail, also have considerable promise as useful visual diagnostic tools for radiologists.

Chapter 4

Using an IVIM Model to Assess Blood Flow in the Placenta

4.1 Introduction

In this chapter, Diffusion Weighted (DW) MR measurements of human placenta *in vivo* are presented. The fetal-placental-uterine system has not been well investigated with MRI in the past due primarily to motion artifacts in images caused by fetal and/or maternal motion during the scans. These artifacts can now be largely avoided using advanced techniques on modern MR scanners with higher amplitude gradients, single shot echo planar imaging (EPI) sequences, respiratory triggering with navigator echoes (e.g. PACE, Siemens Medical Solutions, Erlangen, Germany and parallel imaging capabilities [44,45]). The resulting images have superior image quality with improved SNR and they are not degraded by motion artifacts. The introduction of parallel imaging techniques and navigator echoes to track the motion of the diaphragm for respiratory triggering are the most important recent advancements for abdominal MR imaging, in general, and for placental imaging in particular. The imaging protocols used to acquire the images reported in this thesis take advantage of these advances.

The work presented here demonstrates the ability of MRI to 1) make high quality non-invasive *in vivo* measurements of human placenta using the intravoxel incoherent motion (IVIM) method [76] and 2) accurately evaluate the diffusion and pseudo-diffusion coefficients and the perfusion fraction, collectively known as the IVIM parameters. A better understanding and increased accuracy of these parameters for the placenta, as presented in this chapter, are very important for the evaluation of patients with a suspected placental pathology where the IVIM parameters can be expected to be different from those in healthy subjects. An

example of such a pathology is fetal growth restriction (FGR) where the fetus is abnormally small because the placenta is not providing to the fetus the nutrition it needs for proper growth. It should be noted that none of the subjects studied in the work presented here had FGR.

4.2 Materials and Methods

4.2.1 Subject Population

This study was approved by The Ottawa Hospital Research Ethics Board. Written informed consent was obtained from all participants. Ten volunteers, ranging in age from 23 to 37 years old, were recruited. The Gestational ages of the fetuses ranged from 18 to 35 weeks. One of the volunteers was not scanned due to claustrophobia. The first volunteer was scanned prior to a major upgrade on the scanner using a different protocol (i.e. a breath hold protocol) and the results for this subject will not be included here. The analysis presented in this chapter is thus for 8 subjects. Enrolment in the study was done by Drs. Gruselin and Moretti, obstetricians working at The Ottawa Hospital. Everyone involved in the study, other than the obstetricians, was blinded to the health of the subjects. At the time of imaging, all volunteers were considered to have a normal placenta. Three patients had complications with their pregnancies which were confirmed by ultrasound or at birth. None of these complications were caused by placental pathology. Information about the health of the subjects was not available to the researchers until after the analysis presented in this thesis was completed.

4.2.2 MR technique

MR imaging was performed at the General Campus of The Ottawa Hospital using a 1.5 Tesla (T) MR system (5Magnetom Symphony® Quantum TIM, Siemens AG, Erlangen, Germany) with a maximum gradient strength of 30 mT/m. All MR images were obtained with a multi-channel phased array torso matrix coil positioned anteriorly and elements of the spine matrix coil posteriorly. The hospital's routine clinical pelvic MR protocol was used with all subjects as part of the experimental protocol. An example of an image of a typical healthy placenta can be seen in Fig. 4.1. The total imaging time for all sequences in the protocol was about 8 min per patient.



Fig. 4.1. MRI image showing the anatomy of a healthy placenta (slice 19, patient 2). This image was acquired with a diffusion weighted echo planar sequence with $b = 0$.

Diffusion Weighted Imaging (DWI) of the entire placenta was performed using a DW single shot (SS) echo planar imaging (EPI) sequence with 2D-PACE (see section 2.4), a navigator echo respiratory triggering (NRT) technique (i.e. a sequence called *ep2d_diff_p2_trigg* was used), with small variations in the protocol from subject to subject. TR ranged from 3079.58 to 5865.83 ms due to the patients' different breathing cycles, TE = 94 ms, eighteen 10 mm thick axial slices were acquired with a 2.5 mm inter-slice gap, the FOV was 400 mm, phase FOV = 75%, matrix size = 144x192, in-plane resolution = 2.1x2.1 mm² and the iPAT-GRAPPA reduction factor = 2. An acquisition time of 2 min 4 s was required for the DW sequences to acquire all slices and all *b*-values. When the training period for the 2D-PACE module is included the total acquisition time for the DW imaging was between 3 and 4 minutes, depending on the respiratory cycle of the patient. For the experiments reported here, the acceptance window on the diaphragm location was set to ± 2 mm for triggering the image acquisition part of the sequence. Fat suppression was used to suppress chemical shift artifacts. The fat suppression was done using the SPAIR technique which uses a combination of spectral fat saturation with a short time inversion recovery (STIR) sequence to suppress the signal from fat.

The diffusion weighting was performed using a dual echo pulsed gradient spin echo (PGSE) module with eddy current compensation [82] in front of the EPI echo train (see section 2.3.1.2). Diffusion gradients were applied in the slice selection direction (i.e. in the head-to-foot direction) with the gradient pulse duration, δ , and separation, Δ , set to 45 ms and 50 ms, respectively. Only one

direction was chosen due to time constraints on the scanner and in consideration for the comfort of the pregnant volunteers. For each slice, 13 DW images were obtained, one for each diffusion gradient amplitude applied. The b -values used in the protocol were 0, 50, 100, 150, 200, 250, 300, 350, 400, 450, 500, 650 and 800 s/mm^2 . The values for the signal to noise ratio (SNR) for $b = 0 \text{ s/mm}^2$ and $b = 800 \text{ s/mm}^2$ were approximately 29.1 and 5.1, respectively.

4.2.3 Image Analysis

The decay of the DW MR signal versus b is normally considered to be exponential in tissues, however, a bi-exponential signal decay versus b was assumed in the presented study due to the presence of incoherent pseudo-random motion other than diffusion in the tissue. Blood flowing in the microvasculature of a tissue causes the signal attenuation to be larger than that caused by diffusion alone and the effect is observed as a pseudo-diffusion process. This interpretation is known as intravoxel incoherent motion (IVIM) theory [76]. Accordingly, the signal attenuation curves reported in this thesis were analysed using IVIM theory and the decays were assumed to obey the equation (see also section 2.3.3)

$$SI/SI_0 = (1 - f) \exp(-bD) + f \exp(-bD^*) \quad (4.1)$$

where SI is the measured signal intensity, SI_0 is the measured signal intensity with no diffusion gradient applied, b is the gradient factor of the pulse sequence (i.e. the “ b -value”), D and D^* are the true diffusion coefficient and the pseudo-diffusion (or perfusion) coefficient, respectively, and f is the fractional volume of

the voxel occupied by spins in the microvasculature of the tissue (i.e. the perfusion fraction)

The diffusion decays were analysed using a region of interest (ROI) approach with the ROIs chosen in several different ways. Initially, three rectangular 100-pixel ROIs were sampled for each slice of the placenta (see Fig 4.2). These ROIs were carefully positioned to avoid areas of fast turbulent flow where the blood spurts into the placenta from the spiral arteries of the mother. In a separate analysis, a larger ROI was drawn to encompass as much of the placenta as possible for each slice (see Fig 4.2). This will be referred to as the whole placenta ROI or the WP-ROI. For all four of these ROIs, the mean and standard deviation (SD) of the pixel intensities were computed for each b -value and all slices. These mean values were then used to generate the diffusion decays. The decays for all ROIs were distinctly bi-exponential (see Fig 4.3) and were analyzed using a Levenberg-Marquardt nonlinear least-squares fit to Eq. 4.1 to obtain values for D , f , and D^* . The values plotted in the graphs and reported in the tables represent these parameter values for each ROI averaged over all slices for each volunteer.

D , f and D^* maps were also calculated for the WP-ROI on a pixel-by-pixel basis for each slice. The decays were again clearly bi-exponential and were analysed using the IVIM model. The IVIM parameter values obtained from this analysis were used to generate parametric maps (see Fig 4.4) which were overlaid in colour onto the corresponding anatomical images (i.e. the $b = 0$ s/mm² images).

In a further analysis, the placenta was subdivided, using the anatomical images, into two approximately equal ROIs (see Fig 4.2) termed ROI_{out}, corresponding to the outer part of the placenta, towards the uterine wall, and ROI_{in}, corresponding to the inner area closest to the fetus [57]. These two ROIs were drawn “by hand” for each slice, using IDL’s ROI drawing tool, such that they had approximately equal areas with their common side defining the bisector of the placental cross-sectional area. The mean value for each of these ROIs was calculated for each *b*-value and diffusion decays were generated from these mean values for each slice. The fit was performed as explained above for the 100-pixel ROIs and the IVIM parameter values were obtained for each ROI and each slice. The difference between the values obtained for ROI_{out} and ROI_{in} was then calculated for each of the IVIM parameters for every slice in each patient. The difference values reported below were averaged across all slices for each subject.

All image analysis was performed using software written in the MRI lab at The Ottawa Hospital using IDL (ITT Visual Information Solutions, Boulder, CO)

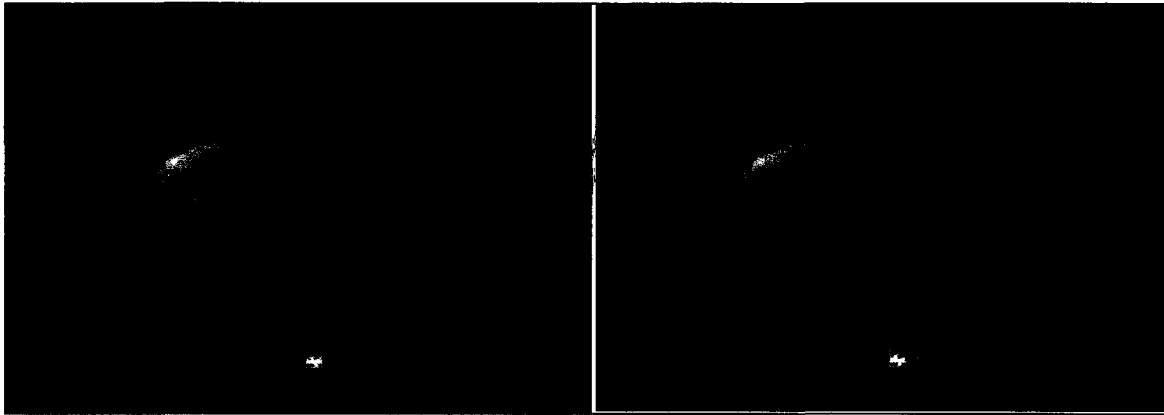


Fig. 4.2. The WP-ROI (red) and the three 100-pixel rectangular ROIs (blue) are shown on the image on the left and the ROIs drawn around the outer (red) and inner (blue) parts of the placenta are shown on the image on the right

4.3 Results

DW images were obtained for 8 volunteers. No motion artifacts were detected in the images and fetal motion did not preclude analysis for any of the women scanned. No significant change in the position of the fetus or the placenta, from the beginning to the end of the study, was noted for any of the subjects. The images did not require rectified noise bias correction since the SNR for the highest b -values used did not drop below 5. All diffusion decays, whether they were for individual pixels or ROIs, were clearly bi-exponential (see Fig. 4.3)

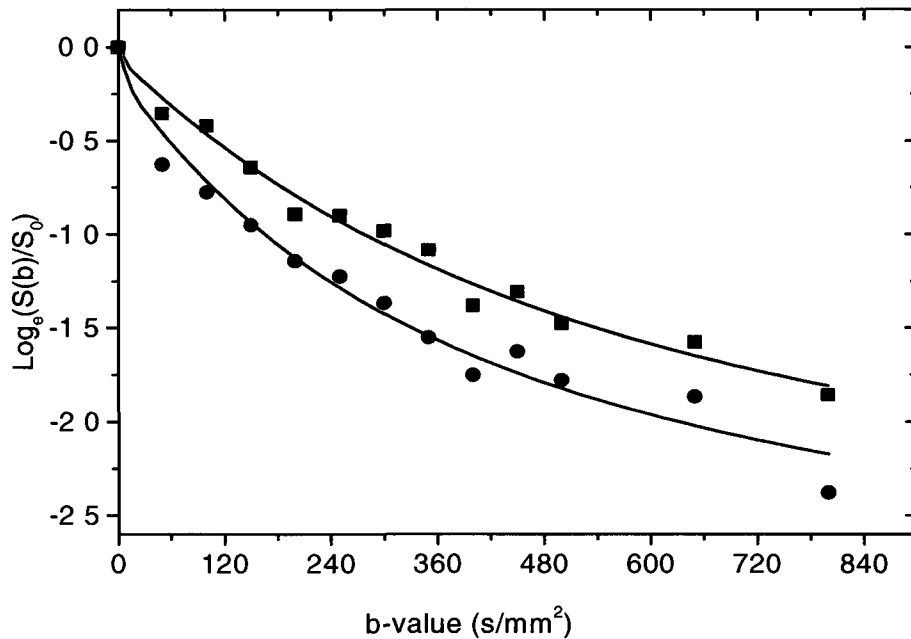


Fig. 4.3. Typical diffusion decays for the WP-ROI and a 100 pixel-ROI. The decays shown are for the WP-ROI (black) and for one of the 100 pixel ROIs (red) shown in (slice 19, patient 2)

4.3.1 IVIM Parametric Maps

In Fig 4.4 color parametric maps of f , D and D^* for a healthy pregnancy are shown overlaid onto the corresponding anatomical image. Inner and outer zones can be seen more clearly on the IVIM parameter maps than on the raw images. Variations of this trend were obtained for the three patients with abnormal conditions.

4.3.2 IVIM Parameters for Different ROIs

Values for D , f , and D^* were obtained for 1) three rectangular 100-pixel ROIs and 2) for the WP-ROI. The mean, computed as the average over all slices and all

pixels contained in the union of the three 100-pixel ROIs, is also shown in the figures and is labelled as U-ROI. This data sets are presented in Figs 4.5 to 4.10.

Figures 4.5, 4.7 and 4.9 show the variation of f , D and D^* , respectively, for the three 100-pixel ROIs averaged over all slices. The parameter values for each of these ROIs are all within one SD of each other for each subject showing that the intra-subject agreement is good for all three IVIM parameters. It also

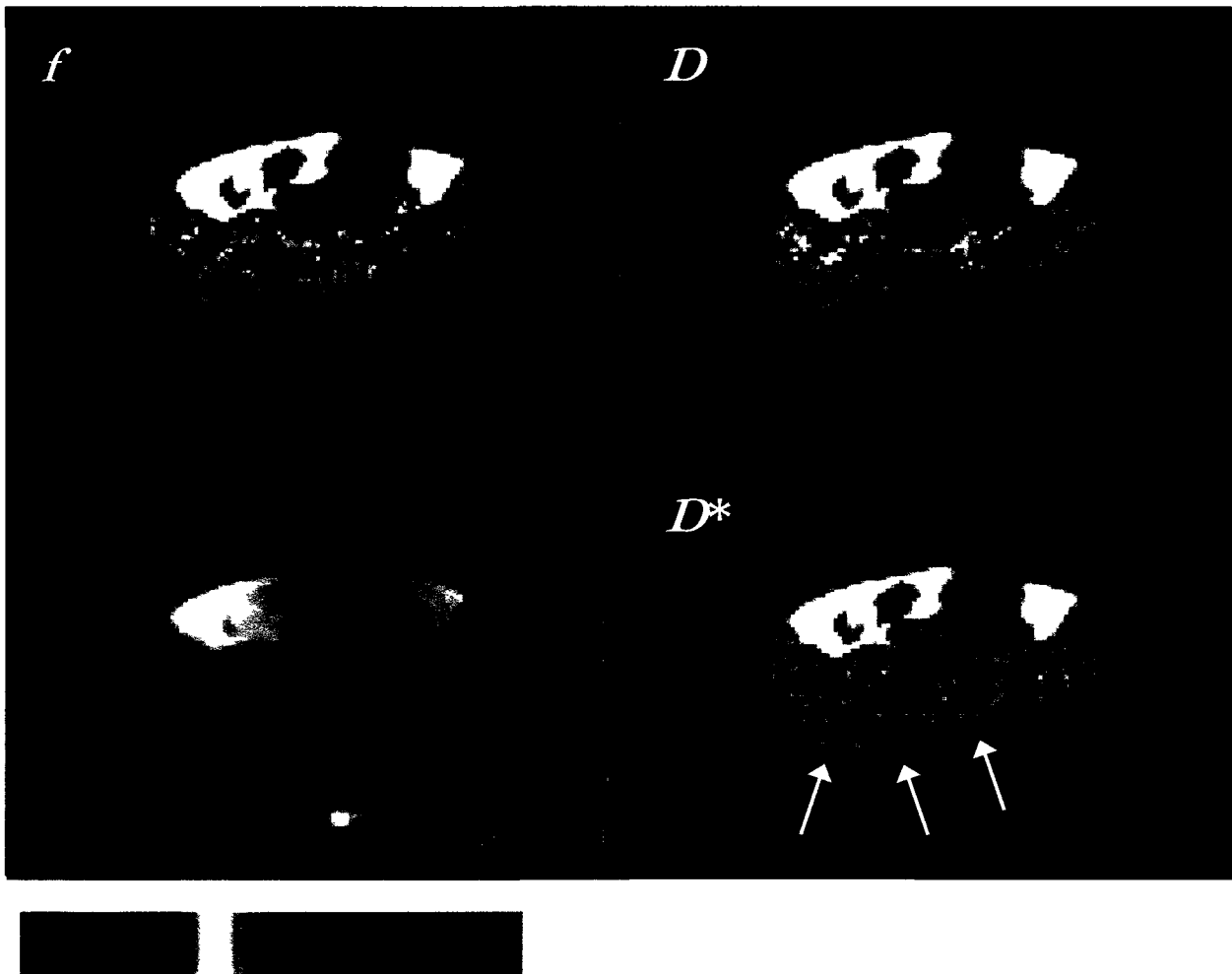


Fig. 4.4. An anatomical image as well as D , D^* and f -maps, color overlaid onto an anatomical image, are shown for a healthy pregnancy (slice 19, patient 2). Two areas of blood movement can clearly be seen on the D^* -map (shades of blue and green, respectively) and the f -map. Areas where maternal blood enters the placenta from the spiral arteries can be seen and are indicated by the arrows on the D^* map. The color table ranges for the maps are a) 0 – 100% for the f -map, b) (0 – 2) $\mu\text{m}^2/\text{ms}$ for the D -map and c) (0 – 200) $\mu\text{m}^2/\text{ms}$ for the D^* -map.

shows that intra-slice variations are small for these ROIs which contain approximately equal volumes of placenta from the fetal and maternal sides. Figures 4.6, 4.8 and 4.10 show the variation of f , D and D^* , respectively, for the WP-ROI and the U-ROI, averaged over all slices in both cases.

The variation of the IVIM parameters with slice position was also considered. No consistent systematic changes were observed with slice position for any of the subjects or ROIs considered. Figs. 4.11 to 4.13 show the variation of the IVIM parameters with slice position for a typical data set. For some of the subjects there was an indication of a small inter-slice variation for f and D^* but this trend could not be discerned beyond experimental error. Therefore, the values in all of the tables and figures (except Figs. 4.11 to 4.13) of this chapter are averaged over all slices.

No statistically significant difference was observed between the IVIM parameter values for the WP-ROI and the U-ROIs, however, a trend towards higher values for the WP-ROI data was noted. For D , the WP-ROI value was higher than the U-ROI value in all cases but this difference was not statistically significant since the D values for these two ROIs were within one SD of each other for all subjects (see Fig. 4.8). A similar observation was made for f except that, in this case, two of the WP-ROI values are slightly more than one SD higher than the corresponding U-ROI value (see subjects 7 and 8 in Fig. 4.6). This trend can also be seen in Fig. 4.10 where the WP-ROI value for D^* is higher than the U-ROI value for D^* for all subjects except for subject 9 where the values are

equal, in about half the cases the difference between the WP-ROI D^* value and the U-ROI D^* value is approximately equal to one SD

The results of the WP-ROI and U-ROI analyses suggest that the IVIM parameters do not vary across the placenta, either within the slice or across slices. For D , this observation is also supported by the D -map for the WP-ROI (see Fig 4.4). However, for the f and D^* parametric maps a variation from the maternal to the fetal side of the placenta is clearly seen. This will be addressed further in sections 4.3.4 and 4.4.4 where ROIs from the fetal and maternal sides of the placenta are considered.

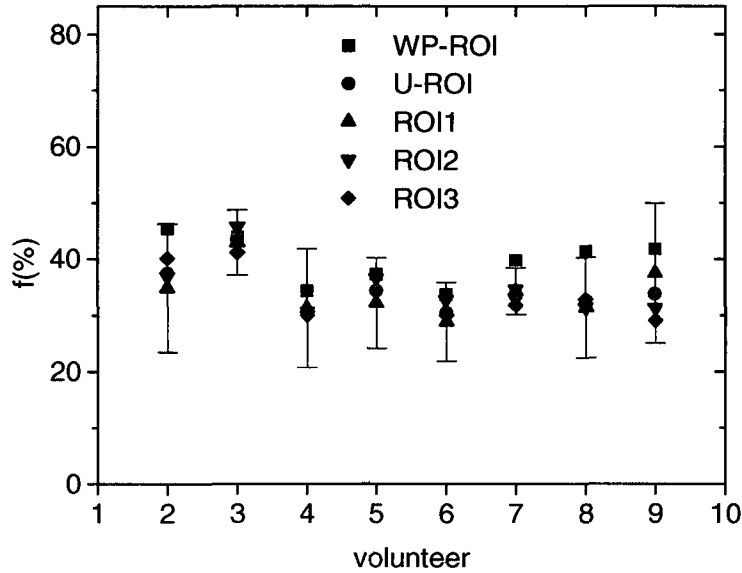


Fig. 4.5. Perfusion fraction, f (%), values plotted for each volunteer for 1) the 100-pixel ROIs, 2) the whole placenta ROI (WP-ROI) and 3) the combined 100-pixel ROIs (U-ROI), averaged over all slices in each case. For clarity, error bars are shown for ROI1 only. The error bars correspond to the mean \pm SD.

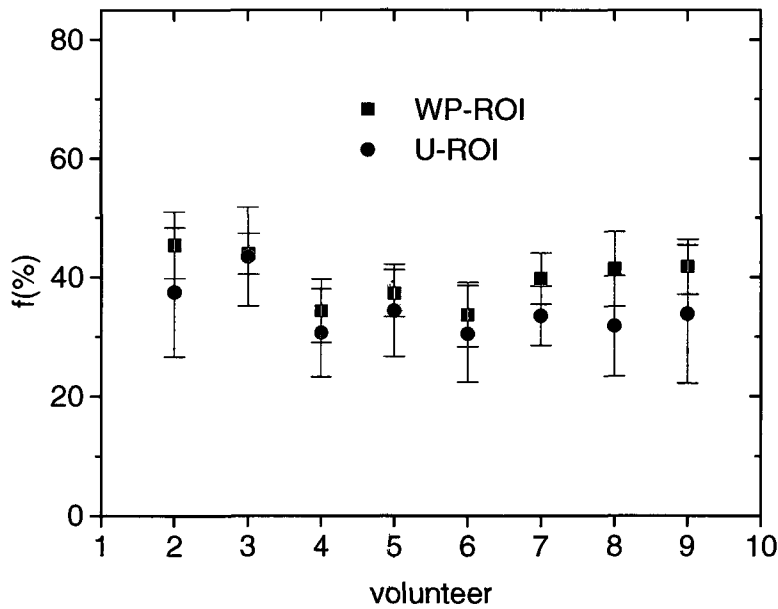


Fig. 4.6. f values for each volunteer for the WP-ROI and the U-ROI, averaged over all slices in each case. The error bars correspond to the mean \pm SD.

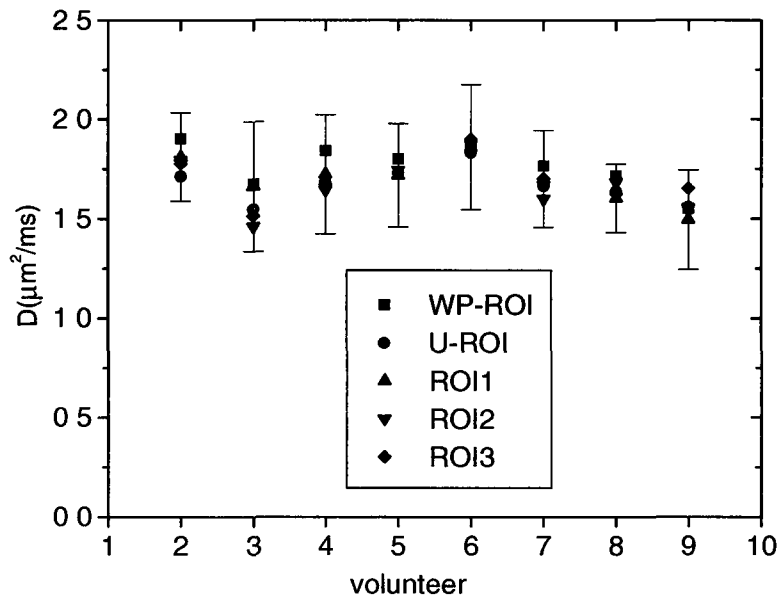


Fig. 4.7. Diffusion coefficient values plotted for each volunteer for 1) the 100-pixel ROIs, 2) the WP-ROI and 3) the U-ROI, averaged over all slices in each case. For clarity, error bars are shown for ROI1 only. The error bars correspond to the mean \pm SD.

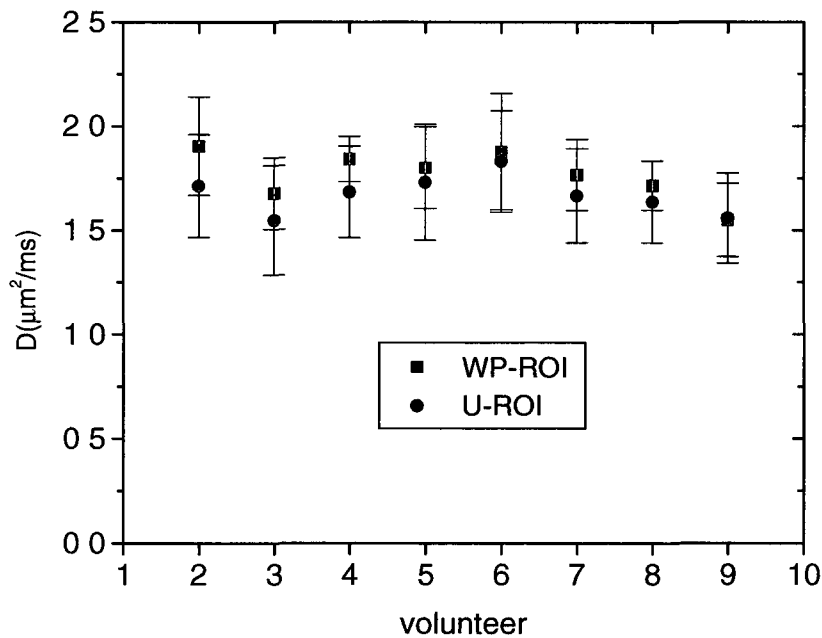


Fig. 4.8. D values plotted for each volunteer for the WP-ROI and the U-ROI, averaged over all slices in each case. The error bars correspond to the mean \pm SD.

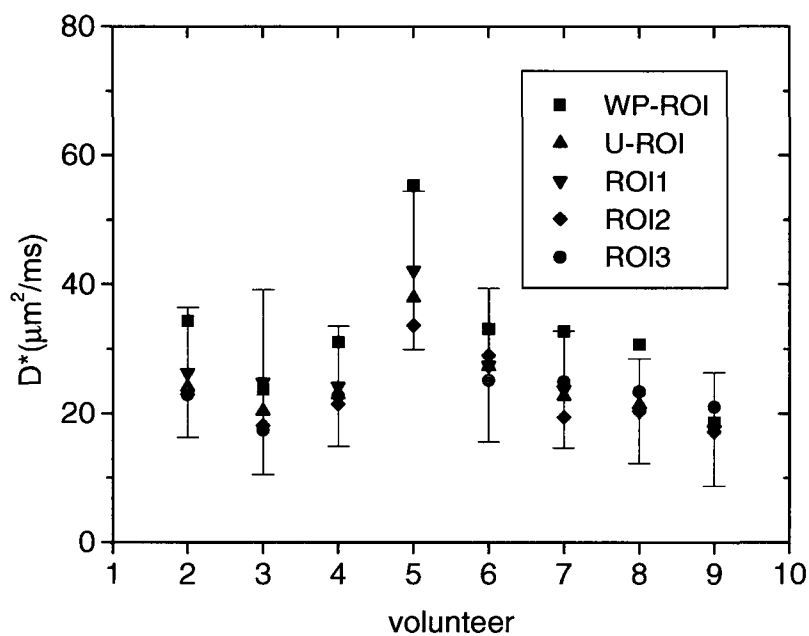


Fig. 4.9. Pseudo-diffusion coefficient values plotted for each volunteer for 1) the 100-pixel ROIs, 2) the WP-ROI and 3) the U-ROI, averaged over all slices in each case. For clarity, error bars are shown for ROI1 only. The error bars correspond to the mean \pm SD.

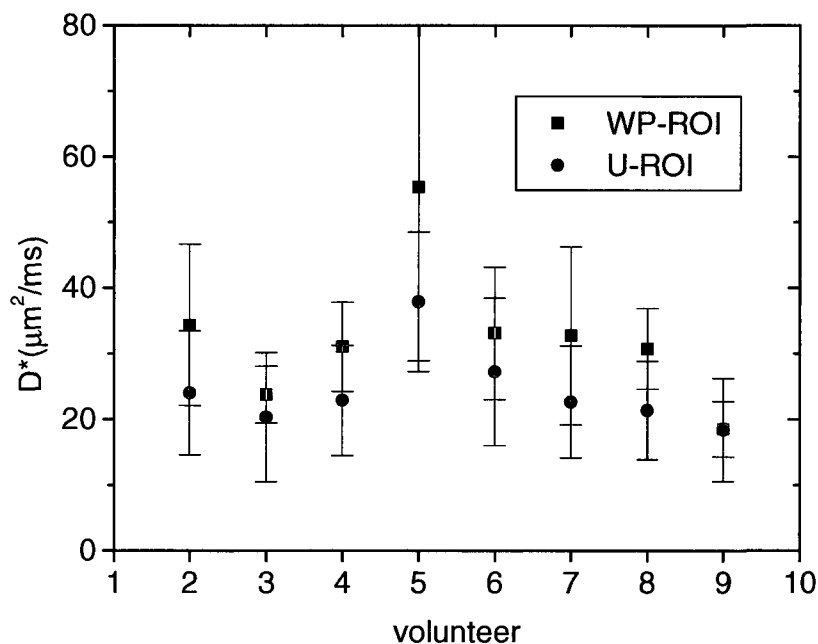


Fig. 4.10. D^* values plotted for each volunteer for the WP-ROI and the U-ROI, averaged over all slices in each case. The error bars correspond to the mean \pm SD.

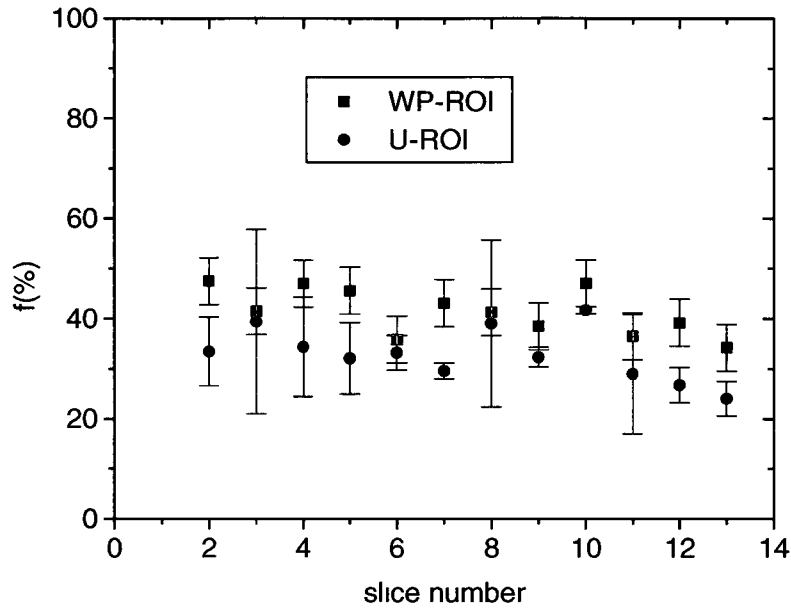


Fig. 4.11. Typical behaviour for f plotted as a function of slice number for the WP-ROI and the U-ROI. The data are from patient 9. The error bars correspond to the mean \pm SD.

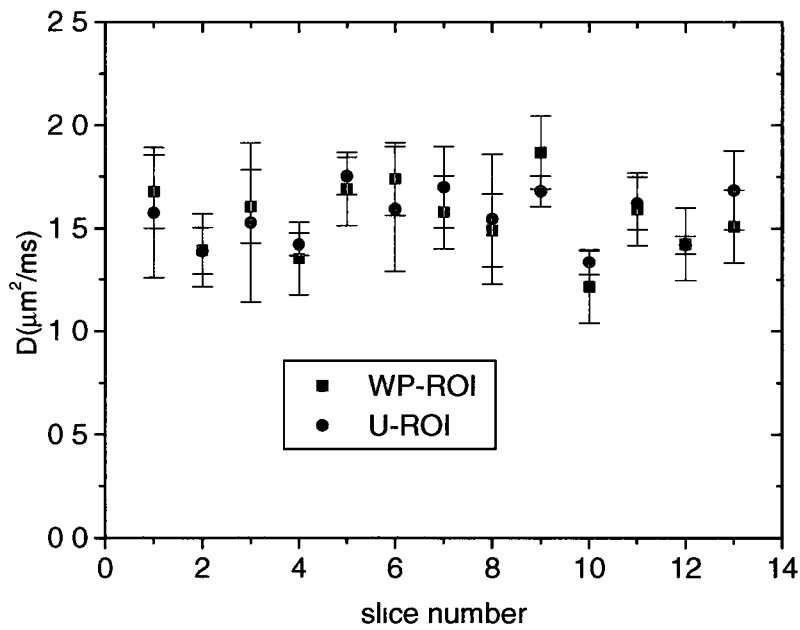


Fig. 4.12. Typical behaviour for D plotted as a function of slice number for the WP-ROI and the U-ROI. The data are from patient 9. The error bars correspond to the mean \pm SD.

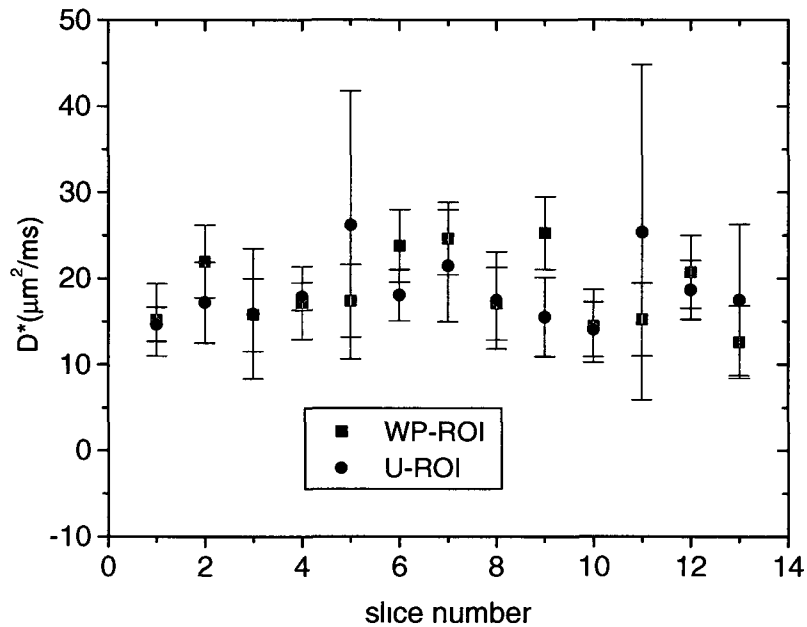


Fig. 4.13. Typical behaviour for D^* plotted as a function of slice number for the WP-ROI and the U-ROI. The data are from patient 9. The error bars correspond to the mean \pm SD.

4.3.3 IVIM Parameters Versus Gestational Age

To determine if the IVIM parameters change during the pregnancy, they were also plotted as a function of gestational age (GA) (Figs 4.14 to 4.16). A linear least squares fit was performed on these data for all three IVIM parameters for both the WP-ROI and the U-ROI. The resulting slope values are given in Table 4.1. From a visual inspection of the figures there appears to be a subtle change in some of the parameters with GA, however, these apparent variations are not statistically significant. Thus, to within experimental error, all of the IVIM parameters are constant for GA = 18 to 35 weeks and we report the IVIM parameter values in Table 4.2 as the mean over GA for this time period.

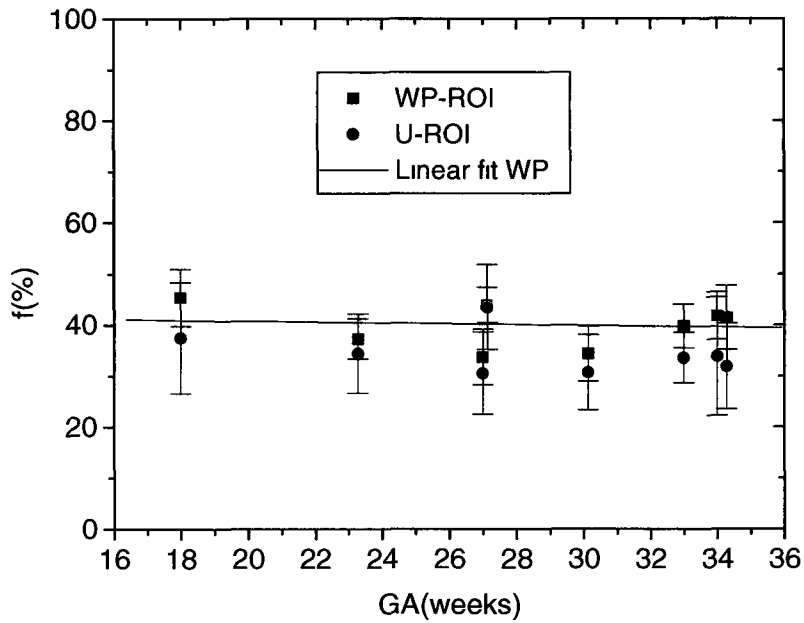


Fig. 4.14. f -values for the WP-ROI and the U-ROI plotted as a function of gestational age (GA) The error bars correspond to the mean \pm SD The black line shows the linear least squares fit to the WP-ROI data

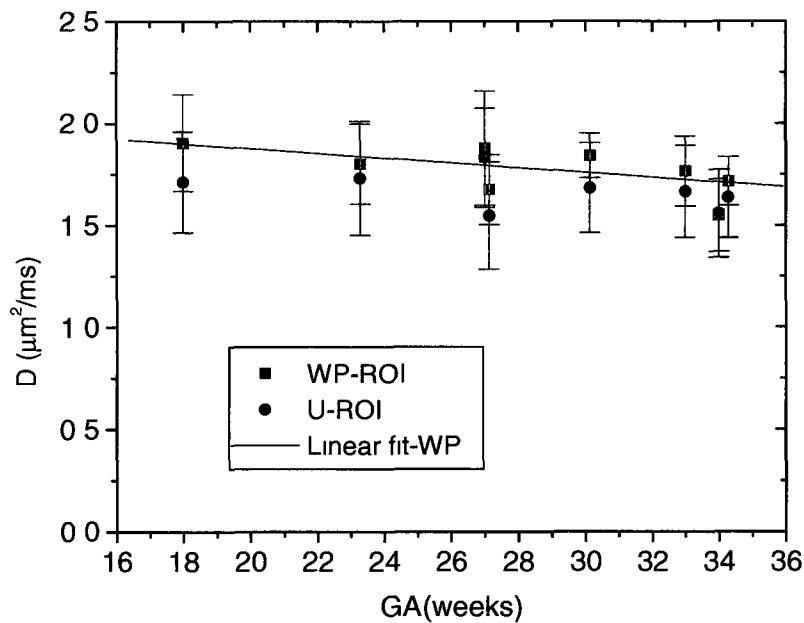


Fig. 4.15. D -values for the WP-ROI and the U-ROI plotted as a function of gestational age (GA) The error bars correspond to the mean \pm SD The black line shows the linear least squares fit to the WP-ROI data

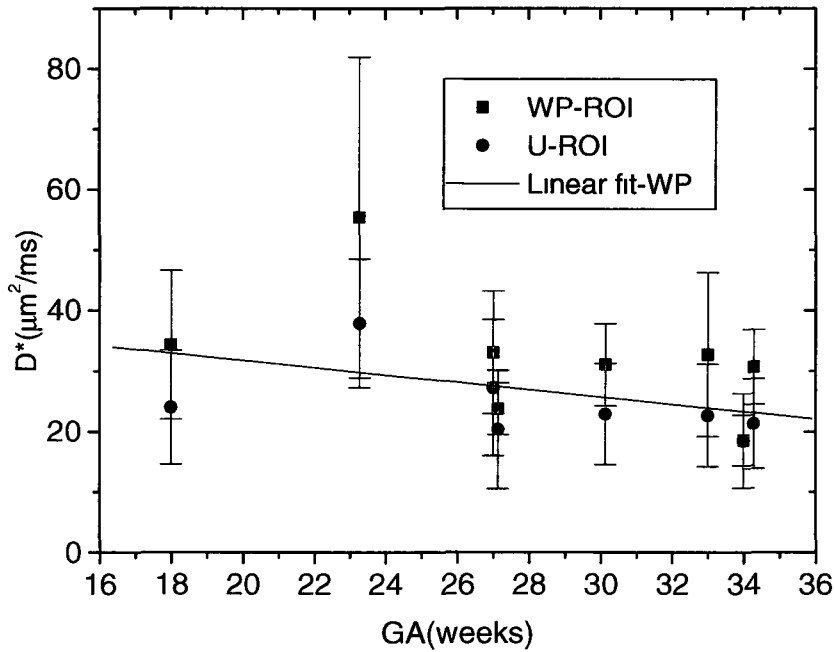


Fig. 4.16. D^* -values for the WP-ROI and the U-ROI plotted as a function of gestational age (GA). The error bars correspond to the mean \pm SD. The black line shows the linear least squares fit to the WP-ROI data.

Table 4.1. Slopes for the IVIM parameters vs GA

	f (%/wk)	D ($\mu\text{m}^2/\text{ms}/\text{wk}$)	D^* ($\mu\text{m}^2/\text{ms}/\text{wk}$)
WP-ROI	-0.1 ± 0.3	-0.01 ± 0.01	-0.6 ± 0.6
U-ROI	-0.3 ± 0.3	-0.01 ± 0.01	-0.2 ± 0.2

Table 4.2. Mean IVIM parameter values averaged over GA = 18 to 35 weeks

	f (%)	D ($\mu\text{m}^2/\text{ms}$)	D^* ($\mu\text{m}^2/\text{ms}$)
WP-ROI	40 ± 6	1.8 ± 0.2	30 ± 12
U-ROI	34 ± 6	1.7 ± 0.3	23 ± 10
p-value (t-test, two tailed)	0.065	0.446	0.225

Note: Data are reported as mean \pm SD. Mean parameters were obtained by averaging the fit parameters over all subjects for both the WP-ROI and the U-ROI (if p -value $<$ 0.05, then results are statistically different).

Table 4 3 Mean IVIM parameter values averaged over GA = 18 to 35 weeks (Ottawa) and the Nottingham data, when a *t*-test was performed, and a two tailed *p*-value is reported

IVIM Parameter	Nottingham (N = 11)	WP-ROI (N = 8)	<i>p</i> -value (Nottingham vs WP-ROI)	U-ROI (N = 3)	<i>p</i> -value (Nottingham vs U-ROI)
<i>D</i> (μm ² /ms)	1 7 ± 0 5	1 8 ± 0 2	0 6103	1 7 ± 0 3	0 999
<i>D</i> * (μm ² /ms)	57 ± 41	30 ± 12	0 0905	23 ± 10	0 0358
<i>f</i> (%)	26 ± 6	40 ± 6	0 0001	34 ± 6	0 0106

Note Data are reported as mean ± SD (if *p*-value < 0 05, then results are statistically different)

All statistical analyses were done using ROIs. SPSS software was used for statistical computations. All ROI distributions were assumed to be normal for these initial analyses and therefore the means and standard deviations of the data were reported. A *t*-test was used to compare the means between WP-ROI and U-ROI as well as with values reported in the literature. Not having the literature data in our possession, we could not be sure of the form of the distributions but we made the assumption that their data are also normally distributed. Mean comparison tests were performed and a two sided asymptotically significant *p*-value was reported in all cases. Statistical significance was defined as *p* < 0 05. However, the assumption of normality was re-examined in a secondary analysis by calculating the skewness and kurtosis for the data sets and by performing a Shapiro-Wilk test of normality. With this secondary analysis it was found that the *D** parameter distributions did not obey the condition of normality and a Mann-Whitney non-parametric test was therefore used in these cases. These results are found in Appendix B.

4.3.4 IVIM Parameters for ROI_{in} and ROI_{out}

The parametric maps shown in Fig 4 4 suggest that there may be a difference in the IVIM parameters between the fetal and maternal sides of the placenta (see section 2 5) ROIs were defined to contain these zones, as described earlier, and the IVIM parameters for these ROIs were determined Figure 4 17 shows typical bi-exponential signal decays for both the inner and outer areas of the placenta outlined in Fig 4 2 The values of the IVIM parameters for ROI_{in} and ROI_{out} averaged over all subjects are summarized in Table 4 3

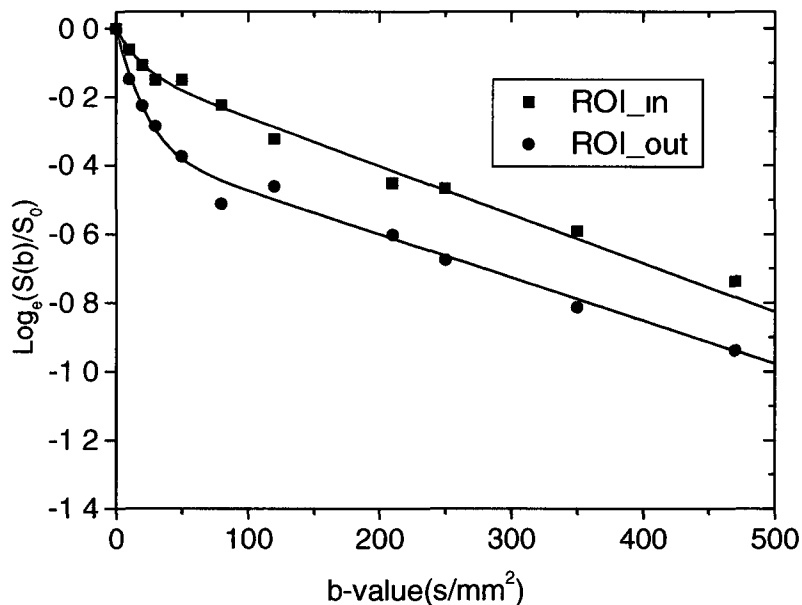


Fig. 4.17. Signal attenuation versus b -value for inner (i.e. fetal side) and outer (i.e. maternal side) placental regions for subject 1, acquired using a breath hold technique. The bi-exponential nature of the decays can clearly be seen.

Table 4.4. Mean IVIM parameter values averaged over all subjects

	f (%)	D ($\mu\text{m}^2/\text{ms}$)	D^* ($\mu\text{m}^2/\text{ms}$)
ROI_{in}	38 ± 8	17 ± 0.4	29 ± 20
ROI_{out}	43 ± 11	17 ± 0.3	34 ± 18

Note: Data are reported as mean \pm SD

While D shows similar values for the two areas, as expected, f and D^* do not. The value of $f_{\text{out}} - f_{\text{in}}$ was positive for 5 of the 8 subjects investigated (see Fig. 4.18) and $D_{\text{out}} - D_{\text{in}}$ and $D_{\text{out}}^* - D_{\text{in}}^*$ were both positive for 7 of the 8 patients in the study (see Figs. 4.19 and 4.20).

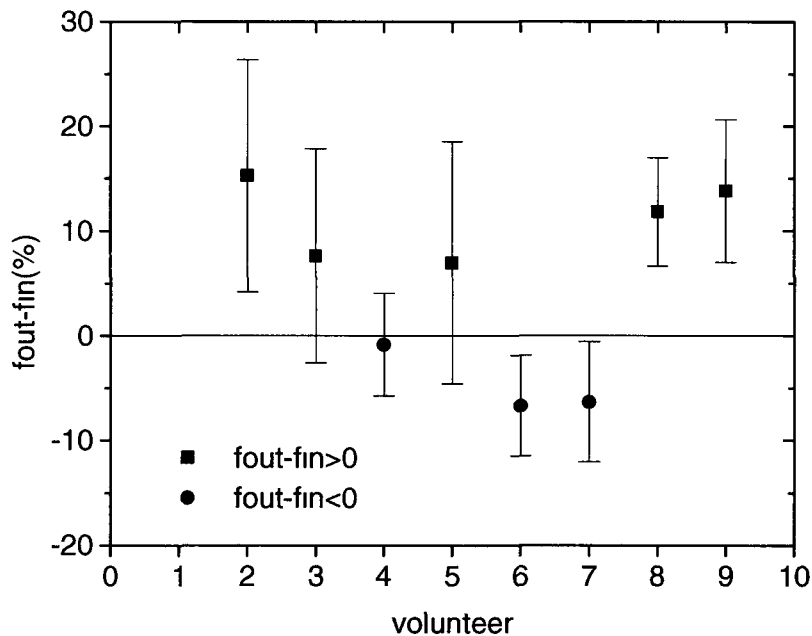


Fig. 4.18 $f_{\text{out}} - f_{\text{in}}$ values for each volunteer (mean \pm SD). $f_{\text{out}} = f_{\text{in}}$ is indicated by a solid black line and negative values are shown in red.

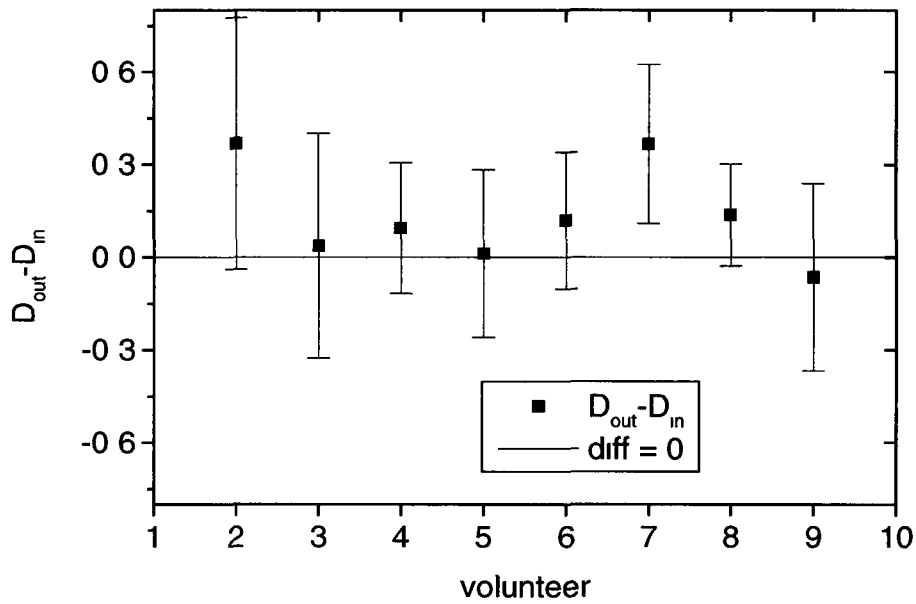


Fig. 4.19 $D_{out} - D_{in}$ values for each volunteer (mean \pm SD) $D_{out} = D_{in}$ is indicated by a solid red line

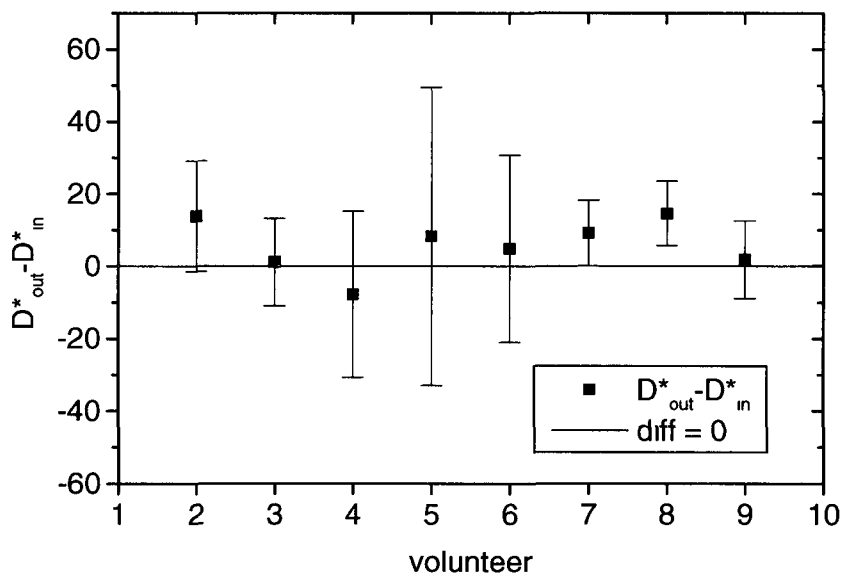


Fig. 4.20 $D_{out}^* - D_{in}^*$ values for each volunteer (mean \pm SD) $D_{out}^* = D_{in}^*$ is indicated by a solid red line

4.4 Discussion

In this chapter, an MRI study of blood flow in and around the placental villi is presented. Since it seemed reasonable to expect that the motion of the water molecules in the blood of the placenta can be explained in terms of a pseudo-random walk behaviour when viewed macroscopically, a DW MR sequence was used to track this motion. The measured bi-exponential signal decays were analysed using the IVIM model (see section 2.3.3 for a review of the IVIM model) and an assessment of the fitting parameters f , D and D^* was made. The faster decaying component was associated with the slowly flowing blood in the microvasculature and the intervillous spaces of the placenta while the other component was assigned to a standard diffusion process for soft tissue (see section 2.5 for a review of placental anatomy and physiology).

The voxel size for the study presented here was $2.1 \times 2.1 \times 10 \text{ mm}^3$, which is very large compared to the size of the fetal blood vessels of the placental villi. The villi are highly branched structures with many small segments pointing in all directions [79]. Thus, in a typical voxel of the placenta, a large anisotropic distribution of velocities for the fetal microcirculation can be expected. For this reason, it would have been useful to study the behaviour as a function of the diffusion sensitization direction but, due to time constraints (as noted above) this was not done. The maternal blood in the placenta enters the intervillous space from the spiral arteries in the uterine wall. The intervillous space is a chamber-like area where the villi are bathed in nutrient rich blood from the mother. The maternal blood in the placenta does not flow through small vessels in the placenta

like the fetal blood does. Instead, it forms a pool of blood that enters the intervillous space from the spiral arteries and leaves via the endometrial veins [79]. The maternal blood entering the intervillous spaces spurts from the spiral arteries and, at this entry point, the flow is both unidirectional and fast. Nevertheless, the flow of most of the maternal blood inside the intervillous space, which is deflected many times by the branches of the villi, is much slower and anisotropic. As with the fetal blood, the maternal blood circulation can, therefore, be viewed as a random walk process. On the scale of a voxel there is a large anisotropic distribution of velocities coming from both the maternal and fetal microcirculation. This results in a contribution to the IVIM parameters from both maternal placental circulation as well as the fetoplacental microcirculation.

In the last few years, new techniques proposed to improve the image quality and precision of diffusion measurements in abdominal imaging include parallel imaging, respiratory triggering using navigator echoes and improved fat suppression. All of these techniques were exploited for the measurements reported here. Parallel imaging is a relatively new technique for MR signal acquisition that takes advantage of the multiple coil elements in state-of-the-art phased array rf receiver coils. This technology can be used to reduce the acquisition time or to increase the number of measurements performed in the same time or a combination of the two. The use of parallel imaging in combination with modern phased array coils leads to a considerable improvement in image quality.

Navigator echo Respiratory Triggered (NRT) sequences allow measurements to be made while the subject is breathing freely as opposed to holding her breath. On a Siemens scanner the NRT procedure is known as 2D-PACE (see section 2.4 for an explanation of 2D-PACE). The navigator echo MR signal that is acquired as part of the NRT technique is used to track the motion of the diaphragm and image acquisition occurs only when the diaphragm is at the desired position. For the experiments reported here the acceptance window on the diaphragm location was set to ± 2 mm. This helps to ensure that the measurements are done with the abdominal organs in the same location each time. Other respiratory gating methods exist but they do not work as well and they require the use of an external device (e.g. a bellows or a pneumatic belt) placed on or around the patient's abdomen to track the motion of the abdominal wall throughout the respiratory cycle. With the NRT technique no additional hardware is required. This makes patient set up considerably easier and avoids patient discomfort related to the use of an external motion tracking device. Furthermore, with NRT technique, the acquisition time is not limited to a single breath hold (15 – 20 s) which would constrain the number of slices that can be imaged and affect the overall accuracy of the results obtained. The use of NRT for DW measurements in the abdomen is far superior to either using a breath hold protocol or using other forms of respiratory triggering. These considerations were discussed in some detail in Chapter 3 where similar measurements are reported for the liver.

Another factor that can have a significant negative effect on image quality with abdominal imaging is chemical shift artifacts. Because the resonant frequencies of fat and water molecules are not the same, the position of adipose (i.e. fatty) tissues is shifted in the images relative to other tissues. For most MR sequences, this shift is only a few pixels and is not a major problem. However, for EPI sequences, such as the ones used in this study, the shift can be a significant portion of the FOV. With abdominal imaging using an EPI sequence, this often causes a bright “ghost” image of the subcutaneous adipose tissue to appear in the middle of the image, possibly obscuring parts of the image that are of specific interest. An effective remedy for this is to suppress the signal from the subcutaneous fat. However, traditional fat suppression techniques do not always work perfectly, with the result that the artifact is not removed completely. The SPAIR technique used here is a combination of two quite different methods of fat suppression, spectral fat saturation and STIR, and does a much better job of completely suppressing the fat signal than previously available methods. Chemical shift artifacts were not a problem for any of the images in this study.

Motion artifacts caused by motion of the abdominal wall during the scan can also be a problem with abdominal imaging. Motion artifacts appear as displaced ghost images superimposed onto the image. The major contribution to these artifacts is often from the bright signal from subcutaneous fat so suppression of the fat signal with SPAIR not only removes chemical shift artifacts but also the primary component of motion artifacts. The use of 2D-PACE also minimizes the

effect of motion artifacts Motion artifacts were not a problem for any of the images in this study

The use of superior hardware with parallel imaging, superior fat suppression and NRT capabilities in our study made possible the acquisition of higher SNR images and more slices with faster data acquisition speeds and overall improved image quality compared with previously reported placental perfusion studies These studies will be reviewed and compared to our work in some detail in the next section The images in our study show good anatomical detail and were not affected by maternal or fetal movement Using a high speed imaging technique and a free breathing protocol also reduces patient discomfort, an important consideration for pregnant women The DW-SS-EPI sequence used for these measurements has eddy current compensation incorporated into the design of the DW part of the sequence [82] so artifacts caused by eddy currents are also negligible The free breathing technique used provides the flexibility of including multiple b -values in the protocol without limiting the number of slices investigated Thus, we were able to image the whole placenta and report IVIM parameter values averaged over the whole placental volume For each patient, 18 slices were acquired and between 8 and 14 of these slices contained placental areas

From the analysis point of view, great care was taken when positioning the square 100-pixel ROIs to avoid areas where maternal blood spurts into the placenta since at these locations the fast flow strongly de-phases the magnetization causing the MR signal for these voxels to be very low

Furthermore, the flow in these locations is not diffusion-like and it is not characteristic of the flow in the rest of the placenta. From a practical point of view, inclusion of these fast flow regions was undesirable because it sometimes caused difficulties with the convergence of the bi-exponential fitting routines, particularly for the pixel-by-pixel calculations required to generate the parametric maps.

4.4.1 Placental IVIM Studies in the Literature

To our knowledge there are only three other studies that have investigated the IVIM parameters for the placenta and all of them are from the same research group in Nottingham. The first two [56,57] were both reported in 2000 and were performed using the same hardware and experimental procedure. For both, the experiments were done using a breath hold protocol on a lab-built 0.5 T scanner. Although they did not mention which coil was used for signal detection it is likely that the built-in body transmit coil was also used as the receiver for both studies since this was a fairly common practice for abdominal imaging at the time these experiments were done and no other receiver coil was mentioned in either paper. The sequence they used had a PGSE module for diffusion weighting and an EPI module for image acquisition. For the PGSE module they used a single spin echo with $\delta = 18.4$ ms and $\Delta = 60$ ms with no inherent eddy current compensation built into the sequence. The other reported parameter values, which were the same for both studies, are TE = 115 ms, TR = 10 s, matrix = 128x128, in-plane resolution = 2.5×3.5 mm², slice thickness = 7 mm, SNR = 20.1 and the total DW imaging time

= 220 s They apparently measured only one axial slice They acquired 11 DW images with the following b -values 0, 0.2, 3, 15, 47, 80, 115, 206, 246, 346 and 468 s/mm² The DW gradient direction was not specified They did not use respiratory triggering or parallel imaging and there is no mention in their paper of using fat suppression

These papers differed in the subject population studied and in the ROI selection In the first paper [56], 11 healthy subjects were studied whereas in the second paper [57] 13 healthy subjects and 7 subjects with fetal growth restriction (FGR) were studied The analysis was done in the first paper using a single ROI of about 100 pixels positioned such that obvious artifacts and flowing blood were avoided whereas for the second study, ROIs were drawn around the inner and outer parts of the placenta, similar to the approach used here and illustrated in Fig 4.2 For both studies, a diffusion decay was constructed from the ROI means for each b -value and the IVIM parameters were determined by fitting this decay to a bi-exponential function In the second study they were able to show, for a small number of patients with FGR, that the difference in perfusion fractions for these two ROIs was correlated with the presence of disease

These studies are good pilot studies and, given the resources available at the time, were well done However, working at a lower field strength with less sensitive rf coils and a longer TE caused the SNR to be considerably lower for their study than ours Furthermore, since they did not use respiratory triggering, fat suppression or parallel imaging, their images would have been affected by chemical shift and motion artifacts – as noted in their papers By sampling

multiple areas of the placenta our IVIM parameter values are also more representative of the average value for the whole placenta and the variance due to experimental error is lower for our work. The hardware and methodology used in our study are clearly superior and our IVIM parameters can therefore be considered to be more precise. This is justified in more detail in the next section. Comparison with their IVIM parameters must be done with caution since the accuracy of their reported values is uncertain.

The Nottingham group's third report dealing with IVIM parameters for the placenta was a poster presented at the ISMRM conference in 2009 [58]. For this work a 1.5 T Philips Achieva scanner with a phased array body receive coil was used. This study was better than their initial work because they used superior hardware, improved MRI parameter settings and a pseudo-respiratory-triggering protocol where the patients were asked to synchronize their breathing to the sound of the scanner gradients. This pseudo-respiratory triggering protocol is superior to the breath hold technique used in their previous study but it is still quite subjective and requires a cooperative patient, there is no guarantee with this technique that the placenta will be in the same location for all measurements. Their basic protocol appears to be similar to ours, however, we have introduced important enhancements by using NRT and fat suppression.

Even though this more recent study appears to be superior to the earlier ones, it is of little use to us since they do not report values for any of the IVIM parameters. Instead they show histogram plots of the parameter distributions for the pixels in their ROI. From a visual inspection of these distributions it can be

deduced that the medians are consistent with the mean values reported in Table 4.2 but, since their distributions are very broad, and, in the case of D^* , quite skewed, any further quantitative comparison would be meaningless

In summary, there are only three reports in the literature of IVIM parameter measurements for the placenta. For all of them, significantly inferior hardware and/or methodology were used compared with the work presented in this chapter. None of these studies gives IVIM parameter values that are as reliable as those reported here. To the best of our knowledge, there are no reports in the literature of IVIM parameters for the placenta that were measured using an NRT protocol

4.4.2 Comparison of our IVIM Parameters with the Literature

The intra-slice and inter-slice agreement for our results was very good for each of the 100-pixel ROIs and for the WP-ROI, for all three IVIM parameters. The values obtained for the WP-ROI and the U-ROI were also in agreement to within experimental error, although there was a trend towards increased f and D^* values for the WP-ROI. The inter-subject variability was also small for all parameters. The data did not show a statistically significant variation for any of the IVIM parameters as a function of GA for the range of gestational ages investigated in this study (i.e. GA = 18-35 wks). Thus, the IVIM parameter values reported here were averaged over all slices and all subjects.

Eight pregnant volunteers were imaged and all were considered to have normal pregnancies at the time the MRI scanning was performed. However,

subsequently it was discovered that three of them had complications with their pregnancies patient 4 had low amniotic fluid volume, patient 6 had a dilated cervix and for patient 7 the placenta was twisted and stuck to the uterine wall Of the eight volunteers enrolled in the study, only one required a premature delivery, but neither the baby nor the mother had any health related problems Additionally, medical assessment of the ultrasound for patient 5 showed that the patient was going into preterm labour None of these conditions relate directly to the health of the placenta They may, however, have had an indirect effect on the placental processes No cases of FGR were reported in our group of volunteers

4.4.2.1 Diffusion Coefficient

Only two of the studies in the literature report placental D values The first one [56] gives $D = (1.7 \pm 0.5) \mu\text{m}^2/\text{ms}$ The other study [57] reported $D = (1.7 \pm 0.9) \mu\text{m}^2/\text{ms}$ and $D = (1.4 \pm 0.8) \mu\text{m}^2/\text{ms}$ for the inner and outer parts of the placenta, respectively These values are all in very good agreement with our values of $D = (1.8 \pm 0.2) \mu\text{m}^2/\text{ms}$ and $D = (1.7 \pm 0.3) \mu\text{m}^2/\text{ms}$ for the WP-ROI and the U-ROI, respectively, and $D_{in} = (1.7 \pm 0.4) \mu\text{m}^2/\text{ms}$ and $D_{out} = (1.7 \pm 0.3) \mu\text{m}^2/\text{ms}$ The results are not significantly different (see Table 4.3) The coefficients of variation (CV) for the three literature values given above are 0.29, 0.53 and 0.57, respectively, whereas our CVs are only 0.11, 0.18, 0.24 and 0.18 for the WP-ROI, U-ROI, ROI_{in} and ROI_{out} results, respectively Our largest CV value is for ROI_{in} This may partly be caused by the more turbulent behaviour of the maternal blood in this ROI It should be noted that, although the mean D values from the

literature are in very good agreement with our values, the precision is much higher for our study, thanks to the superior methodology employed

4.4.2.2 Pseudo-Diffusion Coefficient

The value of D^* , averaged over all subjects, was found to be $D^* = (30 \pm 12) \mu\text{m}^2/\text{ms}$ for the WP-ROI and $D^* = (23 \pm 10) \mu\text{m}^2/\text{ms}$ for the U-ROI. The values that we report for ROI_{in} and ROI_{out} are $D^*_{\text{in}} = (29 \pm 20) \mu\text{m}^2/\text{ms}$ and $D^*_{\text{out}} = (34 \pm 18) \mu\text{m}^2/\text{ms}$. These values are all considerably lower than the previously reported value of $D^* = (57 \pm 41) \mu\text{m}^2/\text{ms}$ [56] but, given the large quoted error for the literature value, they are not inconsistent. It should be noted that the precision for our values is much higher than for the literature value. The CV for the literature study was 0.72 (56) whereas for our study it is only 0.40, 0.43, 0.69 and 0.53 for the WP-ROI, the U-ROI, the ROI_{in} and the ROI_{out} , results, respectively. This shows that the precision of our WP-ROI and U-ROI values is significantly better than for the value reported in the literature (see Table 4.3), due primarily to the superior methodology employed. Values for D^*_{in} and D^*_{out} have not yet been reported in the literature so a proper comparison cannot be made. Our largest CV value is for ROI_{in} . This may partly be caused by turbulent behaviour of the maternal blood in this ROI.

4.4.2.3 Perfusion Fraction

Only two of the studies in the literature report perfusion fraction values. The first gives a value of $f = (26 \pm 6)\%$ with a reported trend towards a decrease of 0.6%

per week [56] The second gives values of $(25 \pm 8)\%$ and $(35 \pm 11)\%$ for the inner and outer sections of the placenta, respectively (see Fig 4.2) [57] Our f values are $(34 \pm 6)\%$, $(40 \pm 6)\%$, (38 ± 8) and $(43 \pm 11)\%$ for U-ROI, WP-ROI, ROI_{in} and ROI_{out} Although the ranges overlap in each case, the literature values are consistently lower than ours The precision of the f value reported here is higher than for the values reported in the literature The CVs are 0.23, 0.32 and 0.31, respectively, for the studies in the literature whereas they are only 0.18, 0.15, 0.21 and 0.26, respectively, for our study

Although our D -value is in good agreement with the literature, the values of f and D^* reported here are somewhat different However, if the stated error ranges are considered, they are not statistically different We believe that our values are more precise since 1) we used a superior MR scanner that gives higher SNR and better image quality, 2) a superior imaging protocol, that included parallel imaging, NRT and good fat suppression, was used, 3) the acquired images were essentially artifact free, 4) an improved approach to the data analysis was used and 5) we report values of the parameters averaged over all slices

4.4.3 WP-ROI versus U-ROI

It is anticipated that the blood dynamics will be different for different parts of the placenta In particular, for locations where maternal blood enters the placenta from the spiral arteries of the mother, the blood flow is expected to be relatively fast and somewhat turbulent with this behaviour diminishing with distance from the arterial input This was investigated by analysing ROIs that included and

excluded the blood as it enters from the spiral arteries (i.e. the WP-ROI and U-ROI, respectively). Furthermore, it is expected that the blood dynamics on the maternal and fetal sides of the placenta will differ. This was tested by comparing the IVIM parameters for ROI_{in} and ROI_{out} , ROIs drawn around the fetal and maternal parts of the placenta, respectively.

The essential difference, in terms of blood dynamics, between the WP-ROI and the U-ROI is the presence in the WP-ROI of the relatively fast flowing, somewhat turbulent, blood from the maternal spiral arteries. These regions were carefully excluded from the 100-pixel ROIs that constitute the U-ROI. Based on this consideration, it is to be expected that both f and D^* will be higher in the WP-ROI than they are in the U-ROI but D should be unaffected. A trend can be seen in Fig. 4.10 where the WP-ROI value for D^* is higher than the U-ROI D^* -value for all subjects except subject 9 where the values are about equal, in approximately half the cases, the WP-ROI D^* -value is about one SD higher than the U-ROI D^* -value. In contrast to this, the D -values obtained for the WP-ROI and the U-ROI are almost identical, as expected.

4.4.4 ROI_{in} versus ROI_{out}

The IVIM parameters were also obtained for ROIs drawn around the inner and outer parts of the placenta. These two areas can be distinguished in the anatomical images of the placenta and corresponding contrast was observed in the f and D^* parametric maps. As expected, the D -values for these two regions were

the same but the f and D^* -values differed considerably. This trend was also seen in the parametric maps (see Fig 4.4)

The parameters $f_{out} - f_{in}$, the difference in the perfusion fractions and $D_{out}^* - D_{in}^*$, the difference in the pseudo-diffusion coefficients attributed to the outer (maternal) and inner (fetal) areas of the placenta, respectively, were also considered. It has been reported that the $f_{out} - f_{in}$ parameter is positive for healthy placenta [57] whereas $D_{out}^* - D_{in}^*$ values have not been reported previously. For 5 of the 8 subjects in our study $f_{out} - f_{in}$ was positive and $D_{out}^* - D_{in}^*$ was positive for 7 of 8 subjects. A negative value for the $f_{out} - f_{in}$ parameter was obtained for all 3 volunteers that had complications with their pregnancies as confirmed for each patient by the obstetrician based on ultrasound results. One of these patients (volunteer 4) had negative values for both of these parameters. Although these patients' conditions were not directly related to placental abnormalities it is quite conceivable that they could have had secondary effects on the blood dynamics within the placenta. In our study, a positive value for $f_{out} - f_{in}$ was indicative of a healthy pregnancy in all cases and a negative value for either of these parameters was always associated with complications. The negative value obtained for these parameters suggests the existence of an abnormal condition in this small preliminary study.

The Nottingham group associates the reduced $f_{out} - f_{in}$ value with FGR mainly and with compromised pregnancy, in general [57] (although their unhealthy group did not contain any patients other than FGR patients). We cannot make this prediction since none of the patients in our study had FGR or

were considered to have had an abnormal placenta, they just presented with an abnormal condition in the pregnancy

4.4.5 Coefficients of Variation for the IVIM Parameters

In general, there will be two primary contributions to the observed variation in the measured parameters, one due to experimental error and the other due to changes in tissue composition across the ROI. The IVIM parameters given by the Nottingham group are averaged over a relatively small ROI from a single slice of the placenta whereas ours are averaged over larger intra-slice ROIs and over all slices of the placenta. The fact that the CV values that we report are smaller than the literature values indicates that we had a smaller amount of experimental error and/or we more effectively removed the effects of random error by averaging over more of the placenta. It also suggests that the inherent variation of the IVIM parameters across the placenta is small since, if this were not the case, our variances would have been as large as or larger than those of the Nottingham group, not smaller. That being said, it is clear that part of the observed variation for f and D^* is due to changes in the tissue properties across the placenta since there are clear differences in these parameters, particularly D^* , for different parts of the placenta (see Fig 4.4)

The variation in D^* was larger than for the other IVIM parameters and seems to be the parameter most affected by ROI location within the slice as well as slice position in the placenta. A distribution of D^* values is to be expected since D^* will be higher for locations near where the blood spurts into the placenta

from the spiral arteries and there will be a gradient of D^* values as the distance from this area increases. On the color D^* -maps (e.g. Fig 4.4), higher D^* values are seen on the maternal side of the placenta where turbulent flow is expected, and a more constant behaviour is found for the rest of the placenta where the density of villi is very high. Blood entering the placenta from the spiral arteries can also clearly be seen in these maps as increased D^* values.

The observed variation of D^* may also be partly related to experimental factors. The parameters D and f are determined by the fit to high b -value data whereas D^* is determined primarily by the behaviour at low b -values. Unfortunately, the Siemens sequence that was used had a fixed increment of 50 s/mm^2 for b . As a result, we were limited to only 3 or 4 points in the range of b -values that was most important for a good determination of D^* . This is discussed in more detail in the previous chapter in conjunction with similar experiments performed on the liver.

For most of the subjects the amount of variation is about the same for the WP-ROI as it is for the U-ROI, but for patient 5 the variation for the WP-ROI is much larger than it is for the U-ROI. Medical assessment with ultrasound for patient 5 determined that the subject was going into preterm labour at the time she had her MR scans and that might have affected the placental processes. This could conceivably lead to regional differences in D^* , explaining this observation. However, since this only occurred with one subject, there is not enough experimental evidence to be conclusive. The other IVIM parameters did not show a similar behaviour.

4.4.6 Discussion of IVIM Parameters

As expected, D does not vary much across the placenta, from subject to subject or with GA since, within the framework of the IVIM model, it is related to the random Brownian motion of the water molecules in the tissue of the placenta and not directly to the circulating blood. D is determined primarily by physical characteristics of the tissue such as membrane permeability, cell size and cell density. The behaviour of the signal decay for higher b -values is dominated by diffusion since the higher amplitude gradients for these b -values attenuate the signal from the spins of the placental microcirculation so much that the contribution from these spins is essentially zero.

On the other hand, the behaviour of the pseudo-diffusion coefficient, D^* , and the active capillary fractional volume, f , also known as the perfusion fraction, are determined by the combined geometry and dynamics of the fetal capillary network in the placental villi and the maternal blood flow around the villi. The perfusion fraction represents the ratio of the volume of MR visible water moving in the capillary compartment (e.g. water in blood cells, plasma, etc.) to the total volume of MR visible water present in the voxel and D^* is the rate constant for the diffusion-like displacement of these water molecules.

D^* is directly related to the speed of the circulating blood and the length of the randomly oriented capillary segments in the villi. In a typical voxel there will be many of these randomly oriented capillary segments. At the same time, maternal blood in the voxel follows a very tortuous, pseudo-random route as it

moves around the many branches of the villi. The measured value of D^* will, therefore, be influenced by the dynamics of both of these blood systems and, in principle, can give very important insight into both the fetal microvasculature of the placental villi and the flow of maternal blood in the intervillous spaces. The diffusion-like molecular displacements associated with D^* are very complex and it is difficult to predict the value of D^* based on known tissue structure and dynamics.

After week 12 of the pregnancy, the growth of the placenta parallels fetal growth, so a constant mean perfusion fraction for $GA > 12$ wks is to be expected. The fractional volume of the intervillous space relative to the total villous plus intervillous volume has been reported to be $(51 \pm 5)\%$ [83]. Bergmann et al [84] report that the villous vascular volume is $(20 \pm 6)\%$ of the total villous volume in healthy subjects. Thus, the blood in the placenta, including maternal blood in the intervillous spaces and fetal blood in the microvasculature of the villi, should be about $51\% + 20\% \times 49\% = 61\%$ of the total placental volume. This is somewhat higher than our value of $f = (34 \pm 6)\%$. However, this measured fractional volume should not be expected to be exactly equal to the actual active capillary fractional volume, although they are related, they are not quite the same. The measured value of f is the fraction of the diffusion decay that corresponds to the faster decaying component within the IVIM bi-exponential decay model. Implicit to this model are the assumptions that 1) there are two independent groups of spins whose diffusion can be characterized by distinct diffusion coefficients, D and D^* , 2) all of the spins in each compartment contribute to the signal for their group's

component of the decay curve and 3) the motion of the spins in each group is diffusive in nature and can be modelled as a random-walk process. These will be discussed individually in the following paragraphs.

The bi-exponential IVIM model assumes that there are two independent groups of spins and that the diffusion of all of the spins in a particular group can be characterized by the same diffusion coefficient which is different from the diffusion coefficient for the other group. This is clearly too simplistic for complex biological tissues, however, as long as the behaviour of the spins in the group can be reasonably represented by the mean behaviour for the group and the distribution of diffusive behaviour for the group is Gaussian-like and not too broad, it can be a useful approach. This appears to be a reasonable approximation for the diffusing spins in biological tissues, in general, and for the placenta, in particular, however, for the flowing blood group in the placenta it may be less reasonable. Certainly in areas near where the blood enters the placenta from the spiral arteries this model may break down but it may be questionable for other areas as well. A gradient of mobility exists across the placenta as the distance from the blood entry point increases. This distribution of mobilities can be expected to be fairly broad and may include regions where the diffusive displacements of the spins in the blood are small and are better characterised by D rather than D^* . In other words, some of the maternal blood may contribute to each of the diffusion components instead of contributing to only the D^* component as is implicitly assumed in the model.

The experimental evidence shows conclusively that the diffusion signal from the placenta can be characterized effectively as a bi-exponential process. It is very likely that the moving blood, in the microvasculature of the villi and the intervillous spaces, is the primary contribution to the faster decaying component and that diffusing water in the tissue contributes to the slower component only but it is possible that the moving blood may contribute to both components. Therefore, making quantitative comparisons between IVIM parameters and known anatomical and physiological values must be done with caution.

The second assumption of the IVIM model mentioned above is that all of the water spins in the tissue contribute equally to the measured signal decay. This may not be accurate when relaxation effects are considered. If the T_1 and T_2 relaxation times are the same for each component then these terms can be factored out of the signal equation to leave the assumed bi-exponential equation for the diffusion decay. However, when this is not the case, relaxation factors must be included for each term. Since these extra factors are not a function of b , they act as weighting factors for f and $1-f$. If, for example, the T_2^* value for the component that diffuses more quickly is much smaller than the T_2^* value for the other component, then the measured value of f will be smaller than would otherwise be expected.

Furthermore, there may be a subgroup of spins that relax so quickly that they do not contribute signal at all. An example of this would be spins that are in close proximity (possibly hydrogen bonded) to a macromolecular surface that can induce relaxation transitions or paramagnetic centers that can locally alter the

magnetic field experienced by the spins. If such a subgroup is distributed equally between the two components then it should not influence f but otherwise it could have an effect. For example, water molecules in the vicinity of deoxyhemoglobin molecules may be strongly affected by the paramagnetic heme group and may not contribute to the measured MR signal because of increased T_2 and/or T_2^* relaxation. If this effect is strongest among the spins contributing to the D^* component then the measured value for f will be smaller than expected based purely on anatomical considerations. Note that T_1 relaxation transitions will also be induced in this example for spins close to the paramagnetic centre but it is unlikely to have a strong effect on the signal when a single shot EPI sequence is used.

The maternal blood as it enters the intervillous space does not immediately undergo pseudo-random motion, as is assumed with the IVIM model. It is unidirectional until it has interacted with the villi enough to randomise the motion of the water molecules in the blood. Spins that move across a voxel in unison will accumulate a phase shift relative to their initial phase but this will have no effect on the measured magnitude of the signal since all of these spins will have the same phase shift. In order to induce decay of the signal magnitude, the spins within a voxel must de-phase relative to one another. In reality there will be a small amount of de-phasing since not all of the spins will have exactly the same speed and/or direction, however, the effect of such isotropic motion on the signal decay will be much smaller than if this motion within the voxel was completely anisotropic. This may be another mechanism whereby water from moving blood

may actually contribute to the more slowly decaying component even though the blood flow is relatively high

While caution must be used when interpreting the IVIM parameters in terms of absolute anatomical and/or physiological properties, it should be emphasized that a comparison of the IVIM parameters for healthy and unhealthy subject groups is still a very important and useful thing to do. While it may be a challenge to measure accurate absolute values for these parameters it is expected that differences in the measured values of these parameters for healthy and unhealthy subjects will be important diagnostic indicators of disease. However, an important prerequisite for such an application is a reliable knowledge of the IVIM parameter values for healthy subjects.

4.5. Conclusions

IVIM parameter values are presented for the placenta that are considerably more reliable than those reported previously. This improvement is partly a result of using superior hardware and a significantly better measurement protocol that included parallel imaging, navigator echo respiratory triggering and SPAIR fat suppression. A more systematic approach was also used for the analysis relative to the earlier studies. The values given here are, for the most part, consistent with the values reported in the literature but they have greatly reduced coefficients of variation (i.e. improved precision) compared with the previous studies. Where the values differ, we believe our values to be the more reliable ones. None of the IVIM parameters was a function of gestational age.

The IVIM parameters discussed in this chapter were studied in five different ways 1) with three square 100-pixel ROIs carefully placed in the placenta to avoid areas where the blood enters the placenta, 2) with an ROI constructed from the union of the three 100-pixel ROIs (i.e. the U-ROI), 3) with an ROI drawn around the whole placenta (i.e. the WP-ROI), 4) with ROIs drawn around the inside (i.e. the fetal side) and the outside (i.e. the maternal side) of the placenta and 5) with a pixel-by-pixel analysis of the whole placenta from which parametric maps were generated. No significant differences were observed for the IVIM parameter values obtained with the 100-pixel ROIs, the U-ROI or the WP-ROI, although there was a trend towards higher values of f and D^* for the WP-ROI (see also Table 4.3 and the tables given in Appendix A). However, the analysis using ROI_{out} and ROI_{in} showed that both f and D^* are larger on the maternal side of the placenta. This trend was also seen in the parametric maps for f and D^* maps. All of these analyses showed that D is the same for all locations within the placenta, to within experimental error. IVIM parametric maps can also be useful for identifying variations in tissue structure and dynamics across the placenta. Important insights into the hemodynamic systems of the placenta can be gained from these maps. The measurement techniques presented here could become instrumental in the assessment and treatment of abnormal pregnancy.

All of the patients studied were considered by the obstetricians to have a healthy placenta. Thus, the parameter values presented here should characterize placental blood dynamics for normal, healthy placentas. However, three of the patients had other complications with their pregnancies. All three of these

subjects had negative $f_{out} - f_{in}$ values and one of them also had a negative value for $D_{out}^* - D_{in}^*$ (the only negative value found for this parameter) None of the other patients had a negative value for either of these parameters Thus, for our small group of patients a negative $f_{out} - f_{in}$ and/or a negative $D_{out}^* - D_{in}^*$ value was associated with a patient with a complication with their pregnancy in every case This is consistent with the results presented by the Nottingham group on $f_{out} - f_{in}$ for patients with fetal growth restriction $D_{out}^* - D_{in}^*$ values have not been reported previously for either healthy or unhealthy human subjects

When comparing the IVIM values with tissue structural information the comparison must be done cautiously Based on information available in the literature it was argued that the blood in the placenta should occupy about 61% of the total placental volume This appears to be in contradiction with our f -value of $(34 \pm 6)\%$ However, various reasons are given for why the measured f -value, the normalized y-intercept on the semi-logarithmic signal decay plots, can be expected to differ from the fractional blood volume of the placenta This parameter is likely related to the blood volume but it is not a direct measure of it

In this chapter significant improvements to the experimental and analysis procedures are presented for studying the IVIM parameters for the placenta As a consequence, the values of the IVIM parameters given here are considerably more reliable than the values previously reported in the literature With these improvements, this approach has significant potential as an important procedure for the diagnosis of placental abnormalities

Chapter 5

Rectified Noise Bias Correction

5.1 Introduction

The extraction of the true MR signal intensity (i.e. the signal intensity that would be obtained in the absence of noise) from noisy MR magnitude images is confounded by a bias caused by noise rectification in the magnitude calculation for pixels with a low signal-to-noise ratio (SNR). This will be referred to in this chapter as rectified noise bias (RNB), in general, and the rectified noise floor (RNF), or simply the noise floor, for the special case where the MR signal is zero. The aim of this chapter is to present a useful technique for removing this bias from the pixel intensities of magnitude MR images. The method presented here is an extension of the analytical solution given by Koay and Basser [86] and the RNB correction (RNBC) algorithm presented previously for a 1-element coil [87] to an N -element phased array coil.

The majority of rf receiver coils on modern clinical MR scanners are phased array coils. The use of phased arrays increases the SNR of the measurement without introducing artifacts and is applicable to all pulse sequences without affecting image contrast. Scanners with this technology can also use the information from the separate coil elements in the phased array to either acquire the image more quickly or acquire more information (e.g. higher resolution images) in the same time. This is known to as Parallel Imaging (PI). For some applications in MR, PI is very important, however, the use of this method is not always advantageous since the SNR of the resulting image is reduced.

Quantitative Magnetic Resonance (QMR) [88] is gaining in popularity because it provides an important additional tool for diagnosis, monitoring of

disease progression and response to treatment. With the conventional approach to MRI, certain tissue properties are used to weight the contrast in the images to help distinguish diseased tissue from healthy tissue. With QMR, the values of MR parameters that characterize these properties are quantified and clinical decisions are made based on these parameter values. The studies presented in chapters 3 and 4 of this thesis are examples of QMR. One thing that people must be aware of with many QMR studies is that RNB can distort diffusion decays, relaxation decays and other quantitative measurements when the signal strength is low. For diffusion and relaxation decays, the signal attenuation is normally followed from a relatively high SNR value to lower intensity values. For complicated multi-component systems it is necessary to measure the attenuation with numerous points along the decay to be able to properly characterize the curve. RNB can sometimes introduce errors into the fit parameters computed from the decay [89] or it can be misinterpreted as an extra component on the decay. If not dealt with properly, RNB can lead to inaccurate results whether signal detection is performed with a 1-element coil or an N -element phased array coil. Note that, although signal averaging can be used to increase the effective SNR, it does not remove the RNB.

For studies such as the IVIM assessment of placenta and liver presented in this thesis, RNB imposes a constraint on the study design since, for example, it restricts the b -value range and the voxel size (i.e. the resolution) that can be used.

In this chapter, a new Rectified Noise Bias Correction (RNBC) method for phased array coils is presented. Section 5.2 is dedicated to a general introduction

of the relevant theory. The extension of the existing algorithm to phased array coils is presented in Section 5.2.2. The usefulness of this RNBC technique is demonstrated with simulations. The methods used to perform these simulations are described in Section 5.3, the results are presented in Section 5.4 and the significance of the algorithm is discussed in Section 5.5.

5.2 Theory of Rectified Noise Bias Correction

5.2.1 Background Theory

For an N -element phased array receiver coil, the noise on the real and imaginary channels for each element in k -space will be statistically independent and well described by a Gaussian Probability Density Function (PDF) with a mean of zero as long as the coil is properly designed and well built. The PDFs for the noise of the Fourier transformed real and imaginary signals are also zero mean Gaussians and these PDFs have a standard deviation of σ_g [90]. There have been a few reports in the literature of noise correlations [91,92] but this effect is not common and will not be considered in the present study.

When the signal detection is performed with an N -element phased array, the magnitude image pixel intensities, M_N , are often computed using a sum of squares algorithm which gives [86]

$$M_N = \sqrt{\sum_{l=1}^N (M_{IR}^2 + M_{II}^2)} \quad \text{with} \quad \begin{aligned} M_{IR} &= A_{IR} + n_{IR} \\ M_{II} &= A_{II} + n_{II} \end{aligned} \quad (5.1)$$

where A_{IR} and A_{II} are the real and imaginary components, respectively, of the true (i.e. noiseless) MR induction signal A , for the l^{th} coil element and n_{IR} and n_{II} are

the statistically independent noise contributions to the real and imaginary channels for the l^{th} coil element, respectively. From Eq (5.1) it can be seen that the image pixel intensity in the absence of noise, A_N , is given by

$$A_N = \sqrt{\sum_{l=1}^N (A_{lR}^2 + A_{lI}^2)} \quad (5.2)$$

The calculation of the pixel magnitudes using a sum-of-squares equation (i.e. Eq (5.1)) rectifies the noise and transforms the distribution of the data from several sets of Gaussian distributed data to a single non-central chi distribution (NCD) of pixel intensities given by [86]

$$P_M(M_N | A_N, \sigma_g) = \frac{A_N}{\sigma_g^2} \left(\frac{M_N}{A_N} \right)^N \exp \left[-\frac{M_N^2 + A_N^2}{2\sigma_g^2} \right] I_{N-1} \left(\frac{M_N A_N}{\sigma_g^2} \right), \quad (5.3)$$

where I_{N-1} is the $(N-1)^{\text{th}}$ order modified Bessel function and the vertical bar in the argument of P_M denotes a conditional probability. The mean of this PDF is shifted away from A_N by an amount equal to the RNB. This PDF can be thought of as the normalized distribution of pixel intensities for an infinitely large image acquired using a phased array coil where the true, noiseless signal is the same for each pixel and the width of the distribution is due to the presence of noise on the MR signal. Equivalently, it can be viewed as the normalized distribution of pixel intensities that would be obtained if the signal from the same voxel was acquired an infinite number of times using a phased array coil.

The first moment of the NCD, μ_x , is given by [86]

$$\mu_x = \beta_N {}_1F_1 \left(-\frac{1}{2}, N, \frac{-\theta_N^2}{2} \right) \sigma_g, \quad (5.4)$$

where ${}_1F_1$ is the confluent hypergeometric function and $\theta_N \equiv A_N / \sigma_g$ β_N is given by the equation

$$\beta_N \equiv \sqrt{\frac{\pi}{2}} \frac{(2N-1)!}{2^{N-1}(N-1)!}, \quad (5.5)$$

where the double factorial is defined by $n!! = n(n-2)(n-4) \dots$ The second moment and the variance of the NCD are given by [86]

$$E_{\chi} \left[M_N^2 \right] = A_N^2 + 2N\sigma_g^2 \quad (5.6)$$

and

$$\sigma_{\chi}^2 \equiv E_{\chi} \left[M_N^2 \right] - \mu_{\chi}^2 = \xi(\theta_N, N) \sigma_g^2, \quad (5.7)$$

respectively, where $E_{\chi} [\]$ signifies the expectation operator calculated over the NCD and the ‘‘correction factor’’, $\xi(\theta_N, N) \equiv \sigma_{\chi}^2 / \sigma_g^2$, has been introduced [86] By substituting Eqs (5.4) and (5.6) into Eq (5.7) and solving for $\xi(\theta_N, N)$, it can easily be shown that

$$\xi(\theta_N, N) = 2N + \theta_N^2 - \left[\beta_N {}_1F_1 \left(-\frac{1}{2}, N, -\frac{\theta_N^2}{2} \right) \right]^2 \quad (5.8)$$

For the special case where $A_N = 0$ this reduces to

$$\xi(0, N) = 2N - \beta_N^2, \quad (5.9)$$

since ${}_1F_1[a, 0, b] = 1$ for all values of a and b [86]

An expression for A_N can be derived by inserting Eq (5.6) into Eq (5.7) and rearranging to get

$$A_N^2 = \mu_{\chi}^2 - [2N - \xi(\theta_N, N)] \sigma_g^2 = \mu_{\chi}^2 - q_N^2 \sigma_g^2 \quad (5.10a)$$

or

$$A_N = \sqrt{\mu_\chi^2 - q_N^2 \sigma_g^2}, \quad (5.10b)$$

where

$$q_N^2 \equiv 2N - \xi(\theta_N, N) \quad (5.11)$$

Koay and Bassler [86] have shown that when the correct values of μ_χ and σ_g are known, exact values of $\xi(\theta_N, N)$ and A_N can be evaluated using Eq (5.10) for any θ_N . In practice, reliable values for σ_g can often be calculated from the image background but accurate values for μ_χ are normally unavailable. Thus, in order for Eq (5.10) to be useful for the removal of RNB in real situations, approximations must be used for μ_χ . For example, for images with areas of uniform pixel intensity (i.e. constant A_N values), μ_χ can be approximated by the mean of these pixel intensities. The reliability of this approximation will depend on the number of pixels in the region of interest (ROI) used to compute this mean.

5.2.2 Extension of the Rectified Noise Bias Correction Algorithm

By applying a binomial expansion to Eq (5.9), the equation for A_N can be transformed from a complex expression involving a square root to a simple *linear* correction with the correction term $\Delta\mu_\chi$ separated from the term to be corrected [87]

$$A_N = \mu_\chi - \mu_\chi \left[\frac{1}{2} \left(\frac{q_N \sigma_g}{\mu_\chi} \right)^2 + \frac{1}{8} \left(\frac{q_N \sigma_g}{\mu_\chi} \right)^4 + \dots \right] = \mu_\chi - \Delta\mu_\chi \quad \text{for } \frac{\mu_\chi}{q_N \sigma_g} > 1 \quad (5.12)$$

The correction term in Eq (5 12) is exactly equal to the RNB. Note that the validity condition for the binomial expansion is always satisfied since, using Eqs (5 10) and (5 11) with $A_N = 0$, it can be shown that $\mu_x(A_N) \geq \mu_x(0) = q_N(0)\sigma_g \geq q_N(A_N)\sigma_g$ where μ_x and $\xi(\theta_N, N)$ are both known to be monotonically increasing functions of A_N [86] and $0.429 \leq \xi(\theta_N, N) \leq 1.0$ [86]. An expression similar to Eq (5 12) has been presented previously for the special case where $N = 1$ but it has not yet been studied for $N > 1$.

Equations (5 10) and (5 12) are mathematically equivalent and they give exactly the same result when an accurate μ_x value is used to calculate A_N . However, when approximate μ_x values are used, as is always required in practice, it is sometimes advantageous to use the binomial expansion form of the equation. The significance of this will be discussed further in Section 5 4.

When μ_x is replaced in Eq (5 12) with an average over n points from a NCD corresponding to the same value of A_N , which we will write as $\langle M_N \rangle_{\chi^n}$, Eq (5 12) can be re-written as

$$\tilde{A}_{N,n',n} = \langle M_N \rangle_{\chi^{n'}} - \langle M_N \rangle_{\chi^n} \left[\frac{1}{2} \left(\frac{q_N \sigma_g}{\langle M_N \rangle_{\chi^n}} \right)^2 + \frac{1}{8} \left(\frac{q_N \sigma_g}{\langle M_N \rangle_{\chi^n}} \right)^4 + \dots \right]$$

for $\frac{\langle M_N \rangle_{\chi^n}}{q_N \sigma_g} > 1$ (5 13a)

or

$$\tilde{A}_{N,n',n} = \langle M_N \rangle_{\chi^{n'}} - \Delta M_{N,n} \quad \text{for } \frac{\langle M_N \rangle_{\chi^n}}{q_N \sigma_g} > 1, \quad (5 13b)$$

where the tilde over the A_N is used to signify that this is an approximate value of A_N and the subscripts indicate that the averaging is performed over n' points for the first term and n points for the correction term where n and n' are not necessarily equal. Note that the binomial validity condition for Eq (5 13) will not always be satisfied since an approximation to the true PDF mean is used

Equation (5 13) can also be expressed as a recurrence relation

$$\tilde{A}_{N n' n} = \langle M_N \rangle_{\chi^{n'}} + \langle M_N \rangle_{\chi^n} \sum_{k=1}^{\infty} a_{k-1} \frac{k - \frac{3}{2}}{k} \left(\frac{q_N \sigma_g}{\langle M_N \rangle_{\chi^n}} \right)^2 \quad \text{for } \frac{\langle M_N \rangle_{\chi^n}}{q_N \sigma_g} > 1, \quad (5 14)$$

where $a_0 = 1$ and a_{k-1} is the previous term in the series. All of the terms in the series are negative which means that the correction term, $\Delta M_{N,n}$, is always positive. This expression is much more convenient for computer simulations

5.3 Methods

The results reported in this chapter were generated using simulation software written in IDL (ITT Visual Information Solutions, Boulder, CO). The magnitude of each simulated MR signal was calculated using Eq (5 1) where the n_{IR} and n_{II} were generated as Gaussian distributed random numbers chosen independently of each other using IDL's RANDOMN procedure. For convenience, σ_g was set equal to one. Note that since the results presented in this chapter are a function of the SNR and not the signal or the noise directly, it does not matter what value is used for σ_g in the simulations. A_{IR} and A_{II} were computed from

$$A_{IR} = A \cos \phi \quad (5 15a)$$

and

$$A_{il} = A \sin \phi, \quad (5.15b)$$

respectively, where ϕ is the phase of the MR receiver, which was assumed to be the same for all coil elements and was arbitrarily set to $\phi = 0$. For simplicity, the same value of A was used for each coil element. Note there is no loss of generality with these assumptions since the simulation results obtained for any A_N value calculated in this way will be equally valid for the same A_N value calculated using different values of A for the different coil elements.

The NCDs used for these simulations were generated, for given values of N , A and σ_g , as histograms from $N_s = 1 \times 10^6$ simulated noisy MR signal magnitudes using the IDL histogram procedure with 400 bins spanning a range of θ_N values from -10 to 10. The histograms were normalized such that the area under the curve is 1.0 so that they correspond to PDFs. In all cases, the mean of these simulated PDFs was in good agreement with the true mean calculated from Eq. (5.4). The RNBC algorithm, for the binomial expansion form of the correction, as given by Eq. (5.14), was initially validated by using the correct values for μ_x which were calculated using Eq. (5.4).

To test the RNBC algorithm for the more realistic situation where an approximation of the PDF mean is used, simulations were performed using Eq. (5.14) with $n = 9$ and $n' = 1$ for $N = 1, 2, 4, 8$ and 16. This corresponds to a situation where the RNBC is applied to individual image pixel intensities with the RNB correction term calculated using $\langle M_N \rangle_{z^9}$, which can be thought of as the average of the intensities of the pixel being considered and the 8 surrounding

pixels It is assumed that these nine points all correspond to the same value of A_N For the purposes of the simulation, this “9-point nearest neighbour average” was computed as the mean over 9 consecutive M_N values for the same value of A_N

Once a value for $\langle M_N \rangle_{\chi^n}$ has been determined, the RNBC algorithm uses the iterative procedure presented by Koay and Bassler [86], which is valid for $\langle M_N \rangle_{\chi^n} \geq \sqrt{2N - \xi(0, N)}\sigma_g = q_N(0)\sigma_g = \beta_N\sigma_g$, to evaluate $\xi(\theta_N, N)$, whenever the validity condition is satisfied This computation is terminated when either the absolute value of the difference between two consecutive iterations is less than or equal to 1×10^{-8} or the number of iterations exceeds 100 When this validity condition is violated the algorithm arbitrarily sets

$$q_N^2(\theta_N) \rightarrow q_N^2(0) = 2N - \xi(0, N) = \beta_N^2 \quad (5.16)$$

The next step in the procedure is to check the validity condition for the binomial expansion in Eq (5.14) If this condition is satisfied, the correction term is computed and $\tilde{A}_{N'n'n}$ is evaluated The series expansion is considered to have converged when either the magnitude of the next term in the expansion is less than 1×10^{-9} or the number of terms considered exceeds 2.5×10^5 It is necessary to consider a large number of terms in the series expansions since these series converge extremely slowly when $\mu_\chi \approx q_N\sigma_g$ or $\langle M_N \rangle_{\chi^n} \approx q_N\sigma_g$

For a given NCD it is to be expected that the binomial expansion condition will be satisfied for some points but violated for others, particularly when N , θ_N and n are small When this condition is violated, neither of the approaches introduced above is strictly valid since they either involve the square root of a

negative number or, equivalently, a diverging series. When the binomial expansion condition is violated in the linear RNBC method proposed here, the algorithm sets $\Delta M_{N,n} = \beta_N \sigma_g$ (i.e. the exact correction for μ_x when $A = 0$) and calculates $\tilde{A}_{N,n}$ directly from Eq. (5.13b). Note that this is not the same as setting $\tilde{A}_{N,n} = 0$ since the approximation $\Delta M_{N,n} = \beta_N \sigma_g$ is only used for determining the correction term, $\tilde{A}_{N,n}$ is the difference between $\langle M_N \rangle_{\text{RN}}$ and $\Delta M_{N,n}$ and there are many possible values for $\langle M_N \rangle_{\text{RN}}$.

The simulations are repeated for $N_s = 1 \times 10^6$ simulated pixel intensities. The values given in the tables and figures of this chapter are the average over these N_s trials, which closely approximates the average calculated over the NCD.

5.4 Results

To test the effectiveness of the RNBC algorithm, simulations were performed with noisy MR magnitude signals generated from real and imaginary vectors using Eq. (5.1). For all of these simulations, a sum-of-squares equation was used to compute the pixel intensities for an N -element array and σ_g was assumed to be the same for all coil elements. These assumptions are not required for the simulations but without them the resulting distributions will not strictly follow the NCD given in Eq. (5.1) and, since the RNB correction algorithm developed in Section 5.2.2 is only theoretically valid for this distribution, it would be more difficult to evaluate the performance of the RNBC algorithm without these

assumptions. In addition, it was assumed that A was the same for all coil elements. In this case, it can be seen from Eq (5.2) that the expression for A_N simplifies to $A_N = \sqrt{N}A$.

Typical uncorrected, simulated distributions are shown in Fig. 5.1 for several values of A for $N = 4$ and in Fig. 5.2 for $\theta = 0.5$ for $N = 1, 2$ and 4 (see the triangular data points). For small θ values, the PDF deviates noticeably from a Gaussian distribution and the RNB cannot be ignored in cases such as these. The distributions shown in these figures are in good agreement with NCD curves published in the literature [91].

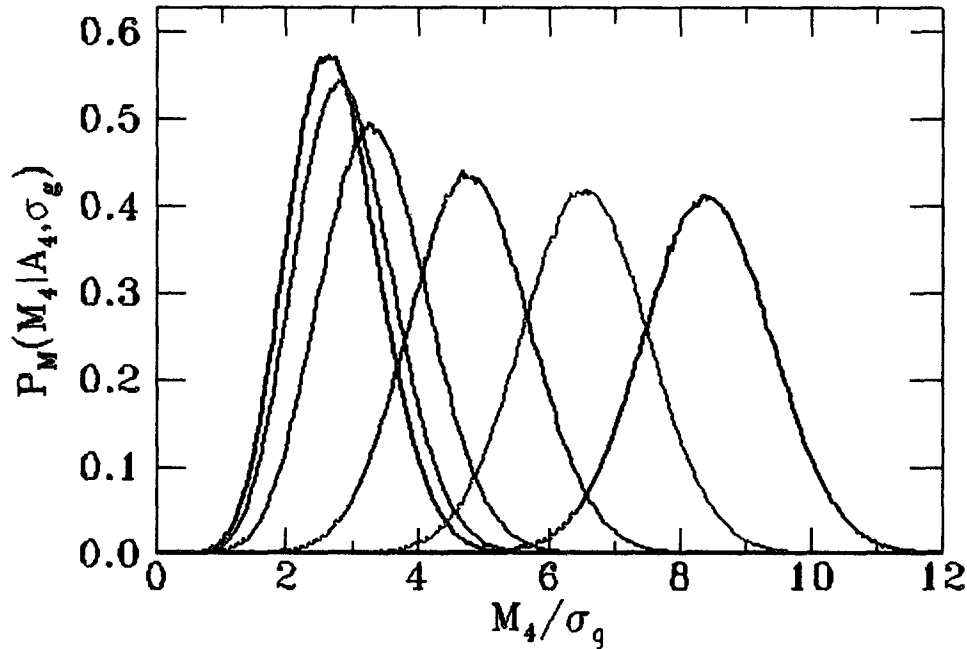


Fig. 5.1 Uncorrected simulated NCDs for several values of $\theta_N = A_N/\sigma_g$ for a 4-element phased array and $\sigma_g = 1$. The black, red, blue, green, purple and dark blue curves correspond to $A = 0.0, 0.5, 1.0, 2.0, 3.0, 4.0$, respectively.

Initially, the RNBC algorithm was tested using Eq (5.12) with the true NCD mean calculated from Eq (5.4). The results of these tests are summarized in Table 5.1 and typical RNB corrected NCDs are shown in Fig. 5.2. For each SNR considered, the computed estimate, $\tilde{\theta}_N$, given in Table 5.1, is very close to the true θ_N value. More complete tables are given in Appendix A for this chapter. Note that computed estimates of a parameter are indicated by placing a tilde over the parameter. For example, the true SNR is written as $\theta_N \equiv A_N / \sigma_g$ while the corresponding computed estimate is denoted by $\tilde{\theta}_N$.

It can also be seen from Fig. 5.2 that, although the RNBC algorithm “corrects” the mean value of the distribution, the shape and variance of each distribution both remain unchanged. Analogous behaviour is seen for all values of A and N investigated.

Table 5.1 Computed estimates of θ_N as a function A and N for the case where the exact values of μ_x and σ_g are used

A	θ_1	$\tilde{\theta}_1$	θ_2	$\tilde{\theta}_2$	θ_4	$\tilde{\theta}_4$	θ_8	$\tilde{\theta}_8$	θ_{16}	$\tilde{\theta}_{16}$
0.000	0.000	0.001	0.000	-0.046	0.000	-0.058	0.000	-0.0528	0.000	-0.042
0.500	0.500	0.500	0.707	0.672	1.000	0.954	1.414	1.371	2.000	1.965
1.000	1.000	1.001	1.414	1.397	2.000	1.974	2.828	2.802	4.000	3.978
2.000	2.000	2.000	2.282	2.828	4.000	3.994	5.657	5.649	8.000	7.991
2.500	2.500	2.500	3.536	3.537	5.000	4.996	7.071	7.066	10.000	9.995
3.000	3.000	3.000	4.243	4.244	6.000	5.998	8.485	8.483	12.000	11.998
4.000	4.000	4.000	5.657	5.678	8.000	7.999	11.314	11.375	16.000	

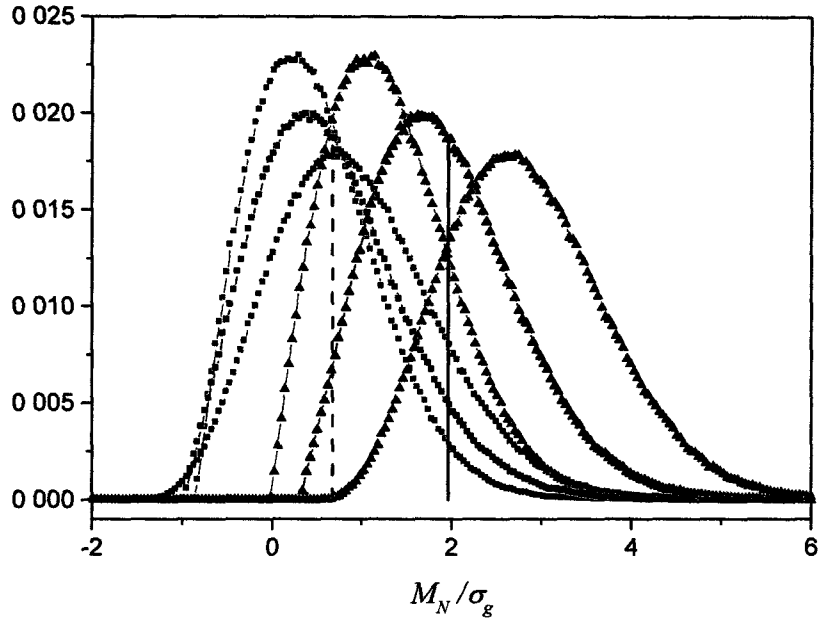


Fig. 5.2. Simulated PDFs before (\blacktriangle) and after (\blacksquare) the RNB correction computed using exact values for μ_x and $\sigma_g = 1$, for $N = 1$ (red), $N = 2$ (black) and $N = 4$ (olive) elements and $\theta = 0.5$. The vertical lines show the corresponding PDF means for the corrected (dashed) and uncorrected (solid) PDFs for $N = 2$. Note that, for this case, the mean of the corrected PDF is very close to the expected value of 0.707.

In the next section, the performance of the proposed RNBC algorithm is evaluated as a function of n , the number of nearest neighbour pixels averaged together. The introduction of nearest neighbour averaging allows for the calculation of the correction term without averaging the term to be corrected. This method provides very good RNBC with minimal PDF distortion. The results are found in Appendices B and C.

5.5 Discussion

Extraction of accurate MR signal intensities from low SNR magnitude MR images has been a challenge for a long time. Recently, there has been growing interest in obtaining accurate values for tissue parameters such as diffusion coefficients and relaxation times. To get reliable information from measured decay curves, a good understanding of the noise and a robust algorithm for dealing with the RNB are important. For decays that are non-exponential or a sum of exponentials, the rectified noise often perturbs part of the decay and affects the quantitative interpretation of the decay as a result. For example, if a decay is assumed to be mono-exponential and only a few low b -values are considered (as is very often done in practice to avoid RNB) when the decay is actually bi-exponential, the decay constant evaluated using only these high SNR points will be incorrect. Conversely, if a decay is actually mono-exponential but it is treated as a bi-exponential decay curve because the RNB effects have not been properly identified, this can also lead to an incorrect interpretation of the decay.

Early attempts at removing the RNB from magnitude MR images were only partially successful and have not been widely adopted, with people frequently opting instead to restrict their measurements to low b -values only, to avoid data points affected by the RNB. Recently, a significant advance was made by Koay and Basser [86] who presented an analytically exact solution for N -element phased array coils for the case where both μ_χ and σ_g are known

Unfortunately, for most situations of interest *in vivo*, reliable μ_x values are not available and approximations must be used

In this chapter it is shown that the solution given by Koay and Bassler for N -element phased array coils can be transformed into a very useful RNB correction technique that can be applied to individual magnitude image pixels by using a binomial expansion to linearize their equation. This removes the square root operation and separates the correction term from the term to be corrected. It also allows the introduction of nearest neighbour averaging to calculate the correction term without averaging the term to be corrected (although this could also be done)

The simulation results presented in this chapter verify that the method works well. For the case where $N = 1$, the results reported here are in very good agreement with previously reported values. For $\theta \geq 1.0$ and $n = 9$ the corrected values are accurate to within 10% error. The new RNB correction algorithm presented here significantly outperforms all previously reported RNB correction techniques for images acquired with phased array coils. This RNBC algorithm provides very good RNB correction with minimal PDF distortion, even when n is small.

In the ideal case, the linear correction term is the same for all pixel intensities, the original NCD is shifted to lower θ_N values with its shape completely undistorted and the mean of the corrected PDF is exactly equal to A_N . When a nearest neighbour average is used, a distribution of corrections occurs which leads to small inaccuracies in the estimates of A_N and minor distortions of

the PDF shape. The main limitation of the technique is that, when $\langle M_N \rangle_{\chi^2} < \beta_N \sigma_g$, $\xi(\theta_N, N)$ cannot be calculated directly. In this case, the algorithm uses the approximation $\xi(\theta_N, N) = \xi(0, N)$. Even so, for $n = 9$ the method works very well and PDF distortion is minimal.

It should be noted that the RNB correction technique presented here corrects for the rectified noise bias but it does not remove the spread in data points caused by noise. The corrected data set will have approximately the same distribution about the corrected PDF mean as the original data set had about the uncorrected PDF mean. Consequently, when $A < \sigma_g$, the corrected data may contain “negative magnitude” data. This should not be of concern since it actually corresponds to the sum of a small positive magnitude signal and a larger negative noise contribution.

The RNBC results presented here consider only the correction of *individual* magnitude image pixels from MR images acquired with N -element phased array coils and no signal averaging. From Eq (5.13) it is clear that the RNB correction can also be used with averaged signals where the signal to be corrected and the correction term need not be calculated using the same type of averaging (e.g. signal averaging, nearest neighbour averaging) or the same amount (e.g. $n' \neq n$) of averaging.

5.6 Conclusion

This chapter presents a method to estimate the RNB from magnitude MRI images when an N -element phased array coil is used. The recently published work of Koay and Basser [86] gives an analytically exact correction scheme for this case and is an important advancement. However, since their method requires accurate values for both the mean and standard deviation of the non-central Chi PDF, it is not practical for *in vivo* situations. By using a binomial expansion of their expression, with the use of a convergence criterion and introducing nearest neighbour averaging, the new correction scheme described here provides very good RNB correction with minimal PDF distortion for all cases when an N -element phased array coil is used.

Chapter 6

General Conclusions

Diffusion-weighted imaging (DWI) is the most important and interesting technique for non-invasively investigating water transport in biological tissues *in vivo*. Using this technique water molecules are tagged and tracked without perturbing their environment or their motion. DWI can also be used to track the motion of water in the microvasculature of tissues when the orientation of these tiny blood vessel segments are short and randomly distributed within the voxel being considered. Under these conditions the water motion in the microvasculature, viewed macroscopically, closely approximates a diffusion process. A DWI measurement of highly vascularised organs such as the liver and the placenta yields a bi-exponential decay where one component corresponds to the water diffusion and the other is associated with slowly flowing blood in the tissue microvasculature (i.e. pseudo-diffusion). This approach is known as the Intravoxel Incoherent Motion model and the three fit parameters obtained from fitting the measured diffusion decay to a bi-exponential function are called the IVIM parameters.

The IVIM model has not often been used in the past for studying abdominal or pelvic organs, mainly because of the difficulty of obtaining artefact free DW images, due to the presence of respiratory motion. In this thesis, a superior approach to DWI is used to obtain high quality DW images and reliable diffusion decay curves. This procedure was used for the IVIM studies of the liver and the placenta reported in Chapters 3 and 4 of this thesis, respectively.

By using the better imaging technique, state-of-the-art scanner hardware and a superior approach to the data analysis we were able to perform more

accurate and precise IVIM parameter quantification compared with other studies previously reported in the literature for both the placenta and the liver. We also showed that a free breathing protocol using a navigator echo respiratory triggered protocol is far superior to a breath hold protocol for measuring the IVIM parameters in the liver.

This is the first study where a whole right liver ROI was investigated and thus we can report, for the first time, average IVIM parameter values for the whole right side of the liver. This is also the first IVIM study where the entire volume of placenta was investigated and the corresponding IVIM parameter values reported. Furthermore, the parametric maps for the IVIM parameters for both the liver and the placenta clearly show changes in f and D^* that were consistent with blood flow patterns in these organs.

IVIM parameters evaluated with a navigator echo free breathing protocol have significant potential as both sensitive and specific parameters for the detection and diagnosis of hepatic and/or placental disease. However, obtaining reliable DW images from which these parameters can accurately be obtained has been a significant problem in the past. With the approach presented in this thesis we were able to overcome this problem and report accurate IVIM parameter values for both normal liver and healthy placenta tissue. Both of these studies represent significant advancements and are an important first step toward the use of IVIM parameters in MRI studies of the abdomen, particularly for the investigated organs. The parametric maps, which showed good anatomical detail, also have considerable promise as useful visual diagnostic tools for radiologists to

help them identify differences in tissues and obtain important insights about the hemodynamic systems present in the tissue. This technique could become instrumental in the assessment and management of abdominal pathologies.

One limitation of this approach is that low signal to noise ratio (SNR) points on the diffusion decay are perturbed by Rectified Noise Bias (RNB). To avoid getting biased data, experiments are designed to ensure that the SNR remains high enough that the RNB has a negligible effect. This means that large b -values and small voxels cannot be used. A method is presented in Chapter 5 of this thesis for overcoming this restriction by correcting the data for the effect of the RNB for image acquisition performed with phased array coils such as were used for the experimental work reported in this thesis. Although it was not necessary to use this RNB correction algorithm for the experimental data reported here, the use of RNB correction would have allowed us to extend our measurements to obtain, for example, higher resolution parametric maps.

As a final thought, this thesis has focused on the water diffusion present in the tissue microvasculature of highly vascular tissues such as the liver and the placenta where the IVIM model is best suited. Diffusion has proven to be a promising source of contrast in MRI and DWI is now an important tool for diagnosis, monitoring of disease progression and response to treatment. The extension of DWI to the study of blood flow in the microvasculature of abdominal organs, as reported in this thesis, also shows significant promise.

APPENDIX A: LIVER Statistics

The tables in this appendix contain descriptive statistics, normality tests for the sample distributions investigated and mean comparison tests. Whenever one parameter distribution has not met the normality condition, the non-parametric tests for the appropriate mean comparison have been determined as well. p -values for both parametric and non-parametric tests are reported.

Table A.1 Descriptive Statistics of the ROI Signal Intensity for an arbitrarily chosen slice10 for Patient 5, in the case of a 100 pixel-ROI and the Whole Right Liver (WRL)-ROI for all 13 protocol b -values

b - value s	Mean_ WR L	SD_ WR L	sk_ WR L	k_ WR L	Mean_ 100pix ROI	SD_ 100pix x ROI	sk_ 100pix x ROI	k_ 100pix x ROI
0	31.9	14.9	2.07	6.69	51.7	21.6	0.67	31.9
1	17.1	5.0	-0.01	0.39	20.5	3.3	0.08	17.1
2	15.6	5.2	0.50	0.93	18.6	3.3	-0.08	15.6
3	14.5	4.5	0.10	0.14	19.1	3.6	-0.13	14.5
4	13.1	5.0	0.01	0.15	17.4	3.1	0.05	13.1
5	13.1	4.5	0.10	0.09	16.0	3.0	-0.07	13.1
6	12.0	4.0	0.09	0.10	14.4	3.5	-0.25	12.0
7	9.7	4.3	0.13	-0.01	12.6	2.2	-0.15	9.7
8	10.5	4.3	-0.02	-0.37	15.2	3.0	-0.25	10.5
9	10.1	4.2	0.01	-0.21	12.4	3.3	0.31	10.1
10	10.0	4.1	0.20	-0.16	11.9	2.6	0.15	10.0
11	8.6	3.8	0.18	-0.21	12.0	3.1	-0.32	8.6
12	7.4	3.4	0.35	-0.05	7.6	2.7	0.06	7.4

Note: Data are reported as mean, SD, skewness (sk) and kurtosis (k) for each investigated ROI.

Table A.2 Descriptive Statistics of the ROI Signal Intensity for 5 consecutive slices for Patient 3 in case of one of the 100 pixel-ROIs and the Whole Right Liver (WRL)-ROI for $b = 50 \text{ s/mm}^2$

Slice number	Mean_ WRL	SD_ WRL	sk_ WRL	k_ WRL	Mean_ 100pix ROI	SD_ 100pix ROI	sk_ 100pix ROI	k_ 100pix ROI
8	17.5	7.1	0.62	1.44	21.0	4.4	-0.13	0.09
9	19.1	6.6	0.54	1.84	26.8	5.3	0.20	-0.59
10	20.3	7.2	0.60	1.06	27.8	7.5	0.74	0.90
11	18.9	7.8	1.18	3.49	26.4	7.4	0.52	0.80
12	18.4	6.5	0.25	0.64	28.3	4.4	-0.08	-0.58

Note: Data are reported as mean, SD, skewness (sk) and kurtosis (k) for each investigated ROI.

Table A.3 Descriptive Statistics of the ROI Signal Intensity for the Central Slice (CS) of each subject(Vol) in the distribution, in case of one of the 100 pixel-ROIs and the Whole Right Liver (WRL)-ROI for $b = 50\text{s/mm}^2$

Vo I #	C S	Mean_W L	SD_W L	sk_W L	k_W L	Mean_ 100pix ROI	SD_ 100pi x ROI	sk_ 100pi x ROI	k_ 100pi x ROI
1	11	9.41	4.58	1.219	6.052	7.98	2.86	0.630	1.182
2	10	31.26	28.86	3.582	6	19.31	6.28	0.238	0.540
3	10	20.28	7.16	0.605	1.062	27.78	7.47	0.740	0.901
4	10	26.92	9.06	2.204	2	35.75	5.36	0.120	0.175
5	10	17.12	5.02	-0.014	0.394	20.47	3.33	0.080	0.437
6	9	19.19	6.12	0.203	0.185	19.86	3.75	0.387	0.683
7	10	13.48	5.66	1.623	0	14.61	3.20	0.048	0.428
8	10	10.51	6.67	1.497	4	10.60	3.47	0.046	0.306

Note: Data are reported as mean, SD, skewness (sk) and kurtosis (k) for each investigated ROI

Table A.4 Mean D , D^* , and f values for liver FB-protocol for parametric and non-parametric mean comparison tests. A two-tailed asymptotically significant p -value is reported. Mean distributions for WP-ROI and U-ROI are compared

IVIM Parameter	t -test p -value	Mann-Whitney p -value
	Parametric	Non-Parametric
D	0.250	0.238
D^*	1	0.973
f	0.294	0.439

Note: Data are reported as mean \pm SD (if p -value $<$ 0.05, then results are statistically different)

Table A.5 A normality test was performed on the population containing the WRL-ROI and PRL-ROI from all the slices for Patient 3 - liver FB-protocol. A two-tailed asymptotic significance p -value is reported

	Shapiro-Wilk		
	Statistic	df	Sig
WRL_D	864	10	086
WRL_F	952	10	692
WRL_Dstar	806	10	017
PRL_D	893	10	183
PRL_F	932	10	470
PRL_Dstar	944	10	603
ROI1_D	893	10	183
ROI1_F	932	10	470
ROI1_Dstar	944	10	603

* This is a lower bound of the true significance

a Lilliefors Significance Correction
Normality assumption can be rejected if $p\text{-value} < 0.05$

Table A.6 Descriptive Statistics for Patient 3, in case of WRL-ROI, PRL-ROI and a 100 pixel-ROI=ROI1 and for $b = 50\text{s/mm}^2$

		WRL_D	WRL_F	WRL_Dst	PRL_D	PRL_F	PRL_Dst	ROI1_D	ROI1_F	ROI1_Dstar
N	Valid	10	10	10	30	30	29	10	10	10
	Missing	20	20	20	0	0	1	20	20	20
Mean		9915	51 1480	45 3990	9420	57 9490	39 7903	1 1611	58 6190	43 0270
Std Error of Mean		04672	2 07583	8 87038	05376	1 70187	3 95218	10937	2 76596	6 56747
Median		1 0420	50 6600	37 2000	9075	56 5550	37 7400	1 1365	56 1350	41 2150
Mode		76(a)	42 20(a)	17 68(a)	80	43 91(a)	12 56(a)	72(a)	46 00(a)	14 53(a)
Std Deviation		14775	6 56434	28 05061	29447	9 32155	21 28314	34585	8 74672	20 76818
Variance		022	43 091	786 837	087	86 891	452 972	120	76 505	431 317
Skewness		- 594	730	1 935	697	429	1 005	- 006	308	555
Std Error of Skewness		687	687	687	427	427	434	687	687	687
Kurtosis		-1 452	530	4 383	230	- 818	1 009	-1 880	-1 167	453
Std Error of Kurtosis		1 334	1 334	1 334	833	833	845	1 334	1 334	1 334
Range		38	22 30	97 52	1 16	31 69	87 15	88	25 80	69 29
Minimum		76	42 20	17 68	44	43 91	12 56	72	46 00	14 53
Maximum		1 15	64 50	115 20	1 60	75 60	99 71	1 60	71 80	83 82
Sum		9 92	511 48	453 99	28 26	1738 47	1153 92	11 61	586 19	430 27
Percentiles	25	8140	45 8725	26 6700	7563	50 8125	22 8450	7925	51 3750	28 7875
	50	1 0420	50 6600	37 2000	9075	56 5550	37 7400	1 1365	56 1350	41 2150
	75	1 1215	55 1450	58 0400	1 0445	64 9575	55 1550	1 5010	66 0800	59 0075

Table A.7 A normality test was performed on the IVIM parameters for WRL-ROI and PRL-ROI from all subjects investigated with the FB-protocol. A two-tailed asymptotic significance p -value is reported.

	Shapiro-Wilk		
	Statistic	df	Sig
WRL_D	970	11	889
PRL_D	986	11	991
ROI1_D	892	11	149
WRL_Dst	912	11	256
PRL_Dst	676	11	000
ROI1_Dst	706	11	001
WRL_f	835	11	027
PRL_f	878	11	097
ROI1_f	846	11	038

* This is a lower bound of the true significance
 a Lilliefors Significance Correction
 Normality assumption can be rejected if p -value < 0.05

Table A.8 Descriptive Statistics of the parameter distributions, when all liver subjects are investigated, for WRL-ROI, PRL-ROI and a 100 pixel-ROI = ROI1 for $b = 50s/mm^2$

Descriptive Statistics

	N	Minimum	Maximum	Mean	Std	Skewness		Kurtosis	
	Statistic	Statistic	Statistic	Statistic	Statistic	Statistic	Std Error	Statistic	Std Error
WRL_D	11	93	1 29	1 1134	11224	011	661	- 591	1 279
PRL_D	11	89	1 25	1 0580	10103	177	661	328	1 279
ROI1_D	11	96	1 18	1 0820	07931	- 287	661	-1 719	1 279
WRL_Dst	11	36 00	75 13	52 3776	12 51460	725	661	- 624	1 279
PRL_Dst	11	35 75	103 32	52 6028	17 95566	2 607	661	7 693	1 279
ROI1_Dst	11	39 97	107 77	55 7300	21 23509	1 917	661	3 105	1 279
WRL_f	11	23 39	48 53	41 3029	7 95204	-1 384	661	1 384	1 279
PRL_f	11	21 94	47 55	38 5544	8 29255	-1 100	661	498	1 279
ROI1_f	11	25 41	49 44	39 4945	7 34350	-1 147	661	853	1 279
Valid N (listwise)	11								

APPENDIX B: PLACENTA Statistics

The tables in this appendix contain descriptive statistics, normality tests for the sample distributions investigated and mean comparison tests. Whenever one parameter distribution has not met the normality condition, the non-parametric tests for the appropriate mean comparison have been effectuated as well. Both parametric and non parametric p-values are reported.

Table B.1 Descriptive Statistics of the ROI Signal Intensity for slice 19, Patient 2, in case of one of the 100 pixel-ROIs and the Whole Placenta (WP)-ROI for all 13 protocol *b*-values

<i>b</i> -values	Mean_WP	SD_WP	sk_WP	k_WP	Mean_100pix ROI	SD_100pix ROI	sk_100pix ROI	k_100pix ROI
0	113.3	28.6	0.57	3.29	122.9	13.0	-1.18	2.66
1	60.0	32.9	0.07	-0.96	84.9	23.7	-1.03	-0.16
2	51.9	28.5	0.22	-0.82	81.6	19.2	-1.21	0.82
3	43.0	23.7	0.04	-1.18	64.1	15.5	-0.95	-0.17
4	35.2	18.5	0.02	-1.17	50.2	13.2	-0.92	-0.37
5	32.4	16.9	0.13	-1.03	52.5	10.9	-1.22	0.97
6	27.9	14.8	0.26	-0.86	49.1	10.1	-0.94	1.20
7	23.6	16.5	0.70	-0.50	42.4	15.1	-0.71	-0.76
8	18.6	12.0	0.43	-0.95	32.3	7.7	-1.22	0.87
9	21.3	11.4	0.27	-0.83	36.2	8.4	-1.03	1.12
10	18.2	10.2	0.25	-0.88	30.8	6.7	-0.86	0.00
11	16.5	10.0	0.29	-1.07	28.8	7.3	-0.42	0.95
12	9.9	6.9	0.90	0.18	20.6	6.1	-0.29	0.08

Note: Data are reported as mean, SD, skewness (sk) and kurtosis (k) for each investigated ROI.

Table B.2 Descriptive Statistics of the ROI Signal Intensity for 5 consecutive slices for Patient 9, in case of one of the 100 pixel-ROIs and the Whole Placenta (WP)-ROI for $b = 50\text{s/mm}^2$

Slice number	Mean_WP	SD_WP	sk_WP	k_WP	Mean_100pix ROI	SD_100pix ROI	sk_100pix ROI	k_100pix ROI
7	69.9	37.7	1.13	2.61	121.8	17.2	0.40	-0.60
8	58.5	27.9	0.00	0.19	86.5	12.8	0.21	0.82
9	49.4	20.4	-0.08	-0.62	72.3	7.4	0.00	0.22
10	45.2	20.0	-0.20	-0.98	61.8	9.8	-0.59	-0.60
11	42.2	18.0	-0.08	-0.30	48.1	23.3	-0.39	-1.08

Note Data are reported as mean, SD, skewness (sk) and kurtosis (k) for each investigated ROI

Table B.3 Descriptive Statistics of the ROI Signal Intensity for the Central Slice (CS) of each subject in the distribution, in case of one of the 100 pixel-ROIs and the Whole Placenta (WP)-ROI for $b = 50\text{s/mm}^2$

Vol #	CS	Mean_WP	SD_WP	sk_WP	k_WP	Mean_100pix ROI	SD_100pix ROI	sk_100pix ROI	k_100pix ROI
2	17	65.8	33.7	0.23	0.18	84.1	35.7	0.86	2.19
3	10	74.8	28.6	-0.02	-0.46	94.6	36.9	-0.77	-0.38
4	11	69.3	15.2	-1.08	1.57	68.2	7.7	-0.48	0.94
5	12	68.0	21.8	-0.44	-0.16	67.6	13.3	-0.81	-0.03
6	9	69.6	22.8	-0.33	-0.14	80.8	14.0	-0.05	-0.50
7	10	66.0	24.4	-0.47	-0.20	67.0	14.7	-0.81	-0.15
8	11	50.2	22.6	0.06	-0.30	79.7	8.4	0.44	0.03
9	9	74.4	23.8	-0.07	-0.30	90.3	9.0	-0.33	-1.09

Note Data are reported as mean, SD, skewness (sk) and kurtosis (k) for each investigated ROI

Table B.4 Mean D , D^* , and f values for placenta FB-protocol for parametric and non-parametric mean comparison tests. A two-tailed asymptotically significant p -value is reported. Mean distributions for WP-ROI and U-ROI are compared.

IVIM Parameter	t -test p -value	Mann-Whitney p -value
	Parametric	Non-Parametric
D	0.074	0.095
D^*	0.074	0.090
f	0.056	0.059

Note Data are reported as mean \pm SD (if p -value $<$ 0.05, then results are significantly different)

Table B.5 A normality test was performed on the population containing the WP-ROI and U-ROI from all the slices for Patient 9. A two-tailed asymptotic significance p -value is reported.

	Shapiro-Wilk		
	Statistic	df	P-value=Sig
WP_D	986	12	997
WP_F	912	12	229
WP_Dstar	876	12	078
UROI_D	938	12	470
UROI_F	928	12	356
UROI_Dstar	771	12	004
ROI1_D	929	12	370
ROI1_F	938	12	471
ROI1_Dstar	765	12	004

* This is a lower bound of the true significance
 a Lilliefors Significance Correction
 Normality assumption is rejected if p -value $<$ 0.05

Table B.6 Descriptive Statistics for Patient 9, in case of WP-ROI, U-ROI and a 100 pixel-ROI=ROI1 and for $b = 50\text{s/mm}^2$

		WP_D	WP_F	WP_Dstar	All_D	All_F	All_Dstar	ROI1_D	ROI1_F	ROI1_Dstar
N	Valid	13	13	13	38	38	38	13	13	13
	Missing	69	69	69	44	44	44	69	69	69
Mean		1 5488	58 2500	18 5377	1 5511	66 0900	18 5695	1 4954	62 5323	17 5323
Std Error of Mean		04907	1 28614	1 16806	03478	1 90687	1 28109	06944	3 43669	2 44687
Median		1 5790	58 5600	17 1300	1 5230	69 9850	17 1950	1 4600	64 1900	16 1700
Mode		1 22(a)	52 52(a)	12 59(a)	1 11(a)	20 54(a)	16 94	1 11(a)	39 35(a)	7 86(a)
Std Deviation		17691	4 63726	4 21149	21440	11 75473	7 89718	25035	12 39116	8 82232
Variance		031	21 504	17 737	046	138 174	62 366	063	153 541	77 833
Skewness		- 106	229	439	- 079	-2 087	2 168	078	- 615	2 380
Std Error of Skewness		616	616	616	383	383	383	616	616	616
Kurtosis		- 139	-1 403	-1 250	- 891	5 603	6 108	-1 413	- 423	7 129
Std Error of Kurtosis		1 191	1 191	1 191	750	750	750	1 191	1 191	1 191
Range		65	13 26	12 66	82	60 80	39 53	75	38 25	35 89
Minimum		1 22	52 52	12 59	1 11	20 54	7 86	1 11	39 35	7 86
Maximum		1 87	65 78	25 25	1 93	81 34	47 39	1 86	77 60	43 75
Sum		20 13	757 25	240 99	58 94	2511 42	705 64	19 44	812 92	227 92
Percentiles	25	1 4080	53 6100	15 2000	1 3730	60 6125	14 4400	1 3140	55 9100	12 5150
	50	1 5790	58 5600	17 1300	1 5230	69 9850	17 1950	1 4600	64 1900	16 1700
	75	1 6845	62 5300	22 8450	1 7158	72 5700	20 7550	1 7325	73 6550	19 2300

a Multiple modes exist The smallest value is shown

Table B.7 A normality test was performed on the IVIM parameters for WP-ROI and U-ROI from all subjects investigated
 A two tailed asymptotic significance *p*-value is reported

	Shapiro-Wilk		
	Statistic	df	Sig
WP_D	954	8	750
UROI_D	959	8	796
ROI1_D	972	8	913
WP_Dst	850	8	096
UROI_Dst	811	8	038
ROI1_Dst	827	8	055
WP_f	943	8	639
UROI_f	853	8	102
ROI1_f	920	8	431

* This is a lower bound of the true significance
 a Lilliefors Significance Correction
 Normality assumption is rejected if $p\text{-value} < 0.05$

Table B.8 Descriptive Statistics of the parameter distributions, when all placenta subjects are investigated, for WP-ROI, U-ROI and a 100 pixel-ROI=ROI1 for $b = 50\text{s/mm}^2$

Descriptive Statistics

	N	Minimum	Maximum	Mean	Std	Skewness		Kurtosis	
	Statistic	Statistic	Statistic	Statistic	Statistic	Statistic	Std Error	Statistic	Std Error
WP_D	8	1 55	1 91	1 7662	11746	- 780	752	266	1 481
UROI_D	8	1 55	1 83	1 6713	09317	257	752	043	1 481
ROI1_D	8	1 50	1 86	1 6964	11391	- 412	752	338	1 481
WP_Dst	8	18 54	55 40	32 4518	10 72428	1 349	752	3 412	1 481
UROI_Dst	8	18 46	37 89	24 3741	6 04954	1 883	752	4 073	1 481
ROI1_Dst	8	17 53	42 14	25 8166	7 32536	1 748	752	4 218	1 481
WP_f	8	33 71	45 39	39 6958	4 26693	- 264	752	-1 257	1 481
UROI_f	8	30 51	43 48	34 4825	4 28205	1 501	752	2 371	1 481
ROI1_f	8	28 87	42 93	34 1548	4 42000	1 127	752	1 380	1 481
Valid N (listwise)	8								

APPENDIX C $\tilde{\theta}$ as a Function of θ and N Calculated Using μ_x and σ_g

The tables in this Appendix contain computed estimates of θ_N as a function of A for the case where the exact values for the NCD mean and σ_g are used to calculate the RNB correction. Since in all cases $\sigma_g = 1$, it can be seen that $\theta = A$, $\tilde{\theta} = \tilde{A}$ and $\tilde{\theta}_N = \tilde{A}_N$ in the following tables

Table C.1. $\tilde{\theta}$ as a Function of θ Calculated Using μ_x and σ_g for $N = 1$

θ	μ_x/σ_g	θ_1	$\tilde{\theta}_1$	$\tilde{\theta}$
0 0000	1 2533	0 0000	0 0014	0 0014
0 1000	1 2564	0 1000	0 1007	0 1007
0 2000	1 2658	0 2000	0 2005	0 2005
0 3000	1 2814	0 3000	0 3004	0 3004
0 4000	1 3030	0 4000	0 4003	0 4003
0 5000	1 3304	0 5000	0 5001	0 5001
0 6000	1 3636	0 6000	0 6010	0 6010
0 7000	1 4023	0 7000	0 7009	0 7009
0 8000	1 4462	0 8000	0 8008	0 8008
0 9000	1 4951	0 9000	0 9007	0 9007
1 0000	1 5486	1 0000	1 0006	1 0006
1 2000	1 6683	1 2000	1 2004	1 2004
1 4000	1 8028	1 4000	1 4002	1 4002
1 5000	1 8749	1 5000	1 5002	1 5002
1 7500	2 0669	1 7500	1 7501	1 7501
2 0000	2 2724	2 0000	2 0000	2 0000
2 5000	2 7112	2 5000	2 4999	2 4999
3 0000	3 1726	3 0000	2 9998	3 9998
4 0000	4 1272	4 0000	4 0012	4 0012

Table C.2 $\tilde{\theta}$ as a Function of θ Calculated Using μ_x and σ_g for $N = 2$

θ	μ_x/σ_g	θ_2	$\tilde{\theta}_2$	$\tilde{\theta}$
0 0000	1 8800	0 0000	0 0463	0 0327
0 5000	1 9381	0 7071	0 6722	0 4753
1 0000	2 1058	1 4142	1 3983	0 9887
1 5000	2 3652	2 1213	2 1178	1 4965
2 0000	2 6945	2 8284	2 8289	2 0003
2 5000	3 0731	3 5355	3 5367	2 5012
3 0000	3 4851	4 2426	4 2442	3 0011
4 0000	4 3689	5 6569	5 6578	4 0001

Table C.3 $\tilde{\theta}$ as a Function of θ Calculated Using μ_x and σ_g for $N = 4$

θ	μ_x/σ_g	θ_4	$\tilde{\theta}_4$	$\tilde{\theta}$
0 0000	2 7416	0 0000	0 0582	0 0291
0 5000	2 7842	1 0000	0 9541	0 4771
1 0000	2 9089	2 0000	1 9743	0 9872
1 5000	3 1073	3 0000	2 9856	1 4856
2 0000	3 3682	4 0000	3 9942	1 9971
2 5000	3 6793	5 0000	4 9958	2 4958
3 0000	4 0295	6 0000	5 9984	2 9992
4 0000	4 8128	8 0000	7 9995	3 9998

Table C.4 $\tilde{\theta}$ as a Function of θ Calculated Using μ_x and σ_g for $N = 8$

θ	μ_x/σ_g	θ_8	$\tilde{\theta}_8$	$\tilde{\theta}$
0 0000	3 9380	0 0000	-0 0528	-0 0187
0 5000	3 9687	1 4142	1 3712	0 4848
1 0000	4 0594	2 8284	2 8022	0 9907
1 5000	4 2067	4 2426	4 2284	1 4858
2 0000	4 4054	5 6569	5 6490	1 9972
2 5000	4 6493	7 0711	7 0665	2 4984
3 0000	4 9320	8 4853	8 4827	2 9991
4 0000	5 5909	11 3137	11 3751	4 0614

Table C.5 $\tilde{\theta}$ as a Function of θ Calculated Using μ_x and σ_g for $N = 16$

θ	μ_x/σ_g	θ_{16}	$\tilde{\theta}_{16}$	$\tilde{\theta}$
0 0000	5 6128	0 0000	-0 0423	-0 0106
0 5000	5 6347	2 0000	1 9654	0 4914
1 0000	5 6999	4 0000	3 9780	0 9945
1 5000	5 8070	6 0000	5 9872	1 4968
2 0000	5 9539	8 0000	7 9914	1 9979
2 5000	6 1378	10 000	9 9951	2 4988
3 0000	6 3556	12 000	11 9988	2 9988

APPENDIX D $\tilde{\theta}$ as a Function of θ and N Calculated Using $\langle M_N \rangle_{x^9}$ and σ_g

The tables in this Appendix contain computed estimates of θ_N as a function of A for the case where μ_x was approximated by a “nearest neighbour average” of NCD distributed pixel intensities in the calculation of the RNB correction μ_x/σ_g represents the theoretical value. Since in all cases $\sigma_g = 1$, it can be seen that $\theta = A$, $\tilde{\theta} = \tilde{A}$ and $\tilde{\theta}_N = \tilde{A}_N$ in the following tables. The number of near neighbours used was 9 for all of these simulations.

Table D.1. $\tilde{\theta}$ as a Function of θ Calculated Using $\langle M_N \rangle_{x^9}$ and σ_g for $N=1$

θ	μ_x/σ_g	θ_1	$\tilde{\theta}_1$	$\tilde{\theta}$
0 0000	1 2533	0 0000	0 256	0 256
0 1000	1 2564	0 1000	0 265	0 265
0 2000	1 2658	0 2000	0 285	0 285
0 3000	1 2814	0 3000	0 320	0 320
0 4000	1 3030	0 4000	0 369	0 369
0 5000	1 3304	0 5000	0 433	0 433
0 6000	1 3636	0 6000	0 507	0 507
0 7000	1 4023	0 7000	0 594	0 594
0 8000	1 4462	0 8000	0 691	0 691
0 9000	1 4951	0 9000	0 794	0 794
1 0000	1 5486	1 0000	0 902	0 902
1 2000	1 6683	1 2000	1 127	1 127
1 4000	1 8028	1 4000	1 349	1 349
1 5000	1 8749	1 5000	1 459	1 459
1 7500	2 0669	1 7500	1 725	1 725
2 0000	2 2724	2 0000	1 985	1 985
2 5000	2 7112	2 5000	2 493	2 493
3 0000	3 1726	3 0000	2 996	2 996
4 0000	4 1272	4 0000	4 005	4 005

Table D.2. $\tilde{\theta}$ as a Function of θ Calculated Using $\langle M_N \rangle_{x^9}$ and σ_g for $N=2$

θ	μ_x/σ_g	θ_2	$\tilde{\theta}_2$	$\tilde{\theta}$
0 0000	1 8800	0 0000	0 3198	0 2261
0 5000	1 9951	0 7071	0 6050	0 4278
1 0000	2 3151	1 4142	1 3388	0 9467
1 5000	2 7826	2 1213	2 0992	1 4844
2 0000	3 3407	2 8284	2 8200	1 9940
2 5000	3 9509	3 5355	3 5307	2 4966
3 0000	4 5911	4 2426	4 2403	2 9983

3 5000	5 2496	4 9497	4 9487	3 4993
4 0000	5 9199	5 6569	5 6555	3 4993

Table D.3 $\tilde{\theta}$ as a Function of θ Calculated Using $\langle M_N \rangle_{x^9}$ and σ_g for $N = 4$

θ	μ_x/σ_g	θ_4	$\tilde{\theta}_4$	$\tilde{\theta}$
0 0000	2 7416	0 0000	0 3934	0 1967
0 5000	2 9089	1 0000	0 8666	0 4333
1 0000	3 3682	2 0000	1 9514	0 9757
1 5000	4 0295	3 0000	2 9868	1 4934
2 0000	4 8128	4 0000	3 9944	1 9972
2 5000	5 6671	5 0000	4 9970	2 4985
3 0000	6 5639	6 0000	5 9984	2 9992
3 5000	7 4876	7 0000	6 9985	3 4993
4 0000	8 4292	8 0000	7 9990	3 9995

Table D.4 $\tilde{\theta}$ as a Function of θ Calculated Using $\langle M_N \rangle_{x^9}$ and σ_g for $N = 8$

θ	μ_x/σ_g	θ_8	$\tilde{\theta}_8$	$\tilde{\theta}$
0 0000	3 9380	0 0000	0 4760	0 1683
0 5000	4 1776	1 4142	1 2579	0 4447
1 0000	4 8310	2 8284	2 7974	0 9890
1 5000	5 7651	4 2426	4 2328	1 4965
2 0000	6 8677	5 6569	5 6520	1 9983
2 5000	8 0696	7 0711	7 0681	2 4990
3 0000	9 3321	8 4853	8 4835	2 9994
3 5000	10 633	9 8995		
4 0000	12 137	11 314	11 294	3 9931

Table D.5 $\tilde{\theta}$ as a Function of θ Calculated Using $\langle M_N \rangle_{x^9}$ and σ_g for $N = 16$

θ	μ_x/σ_g	θ_{16}	$\tilde{\theta}_{16}$	$\tilde{\theta}$
0 0000	5 6128	0 0000	0 5813	0 1453
0 5000	5 9539	2 0000	1 8458	0 4615
1 0000	6 8801	4 0000	3 9794	0 9949
1 5000	8 1997	6 0000	5 9923	1 4981
2 0000	9 7553	8 0000	7 9980	1 9995
2 5000	11 451	10 000	9 9972	2 4993
3 0000	13 232	12 000	11 986	2 9965
3 5000	15 070	14 000	13 985	3 4963
4 0000	16 942	16 000	15 984	3 9961

APPENDIX E Simulated PDFs Before and After the RNBC Calculated Using

$$\langle M_N \rangle_{x^9} \text{ and } \sigma_g \text{ for Different } N \text{ Element Coils}$$

The figures in this Appendix contain simulated PDFs before (solid) and after (dashed) the RNB correction in the 9-nearest neighbour approximation for $N = 1$ (Fig E 1), $N = 2$ (Fig E 2), $N = 4$ (Fig E 3), $N = 8$ (Fig E 4) and $N = 16$ (Fig E 5) elements with $\theta = 0.5$. The vertical lines show the corresponding PDF means for the corrected (dashed) and uncorrected (solid) PDFs for the respective number of coils.

Figure E.1 Simulated PDFs Before and After the RNBC Calculated Using $\langle M_N \rangle_{x^9}$ and σ_g for $N = 1$

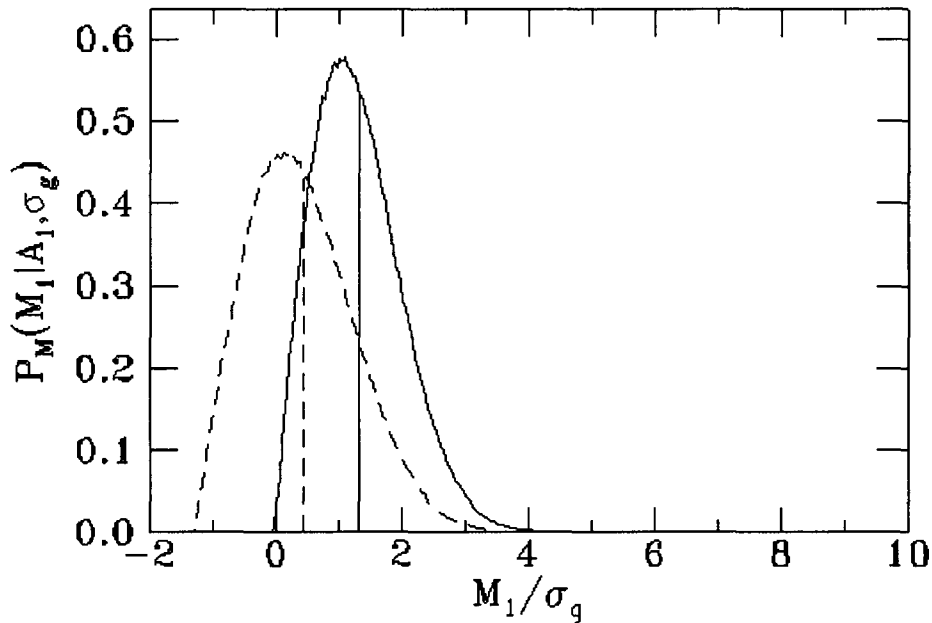


Figure E.2 Simulated PDFs Before and After the RNBC Calculated

Using $\langle M_N \rangle_{\chi^2}$ and σ_g for $N=2$

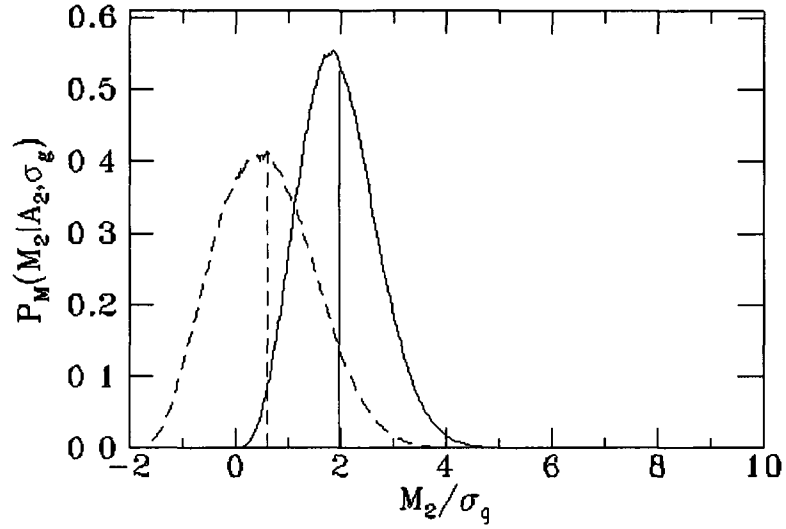


Figure E.3 Simulated PDFs Before and After the RNBC Calculated

Using $\langle M_N \rangle_{\chi^2}$ and σ_g for $N=4$

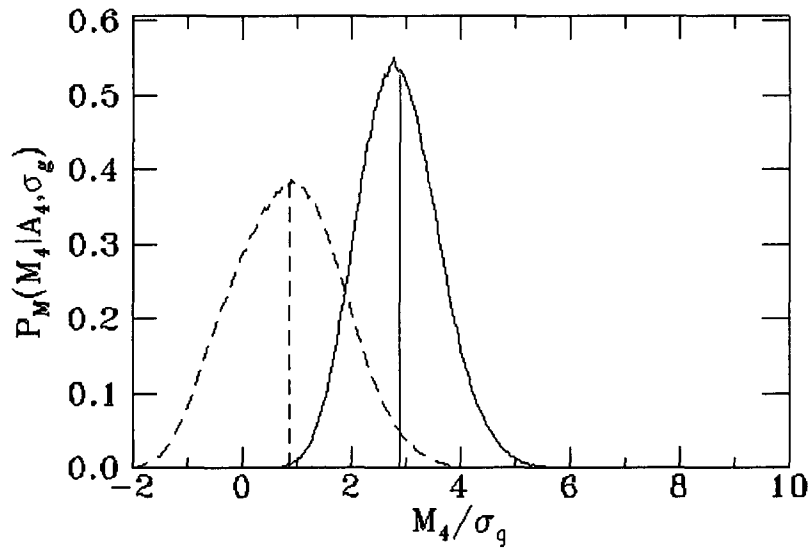


Figure E.4 Simulated PDFs Before and After the RNBC Calculated

Using $\langle M_N \rangle_{x^9}$ and σ_g for $N=8$

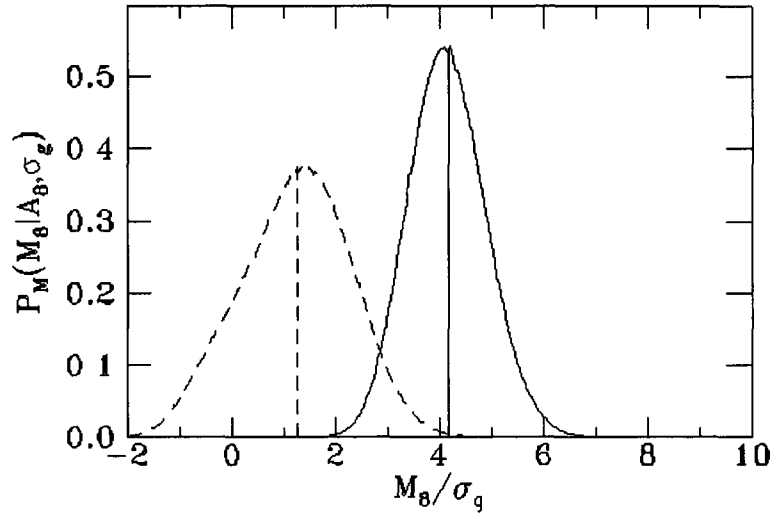
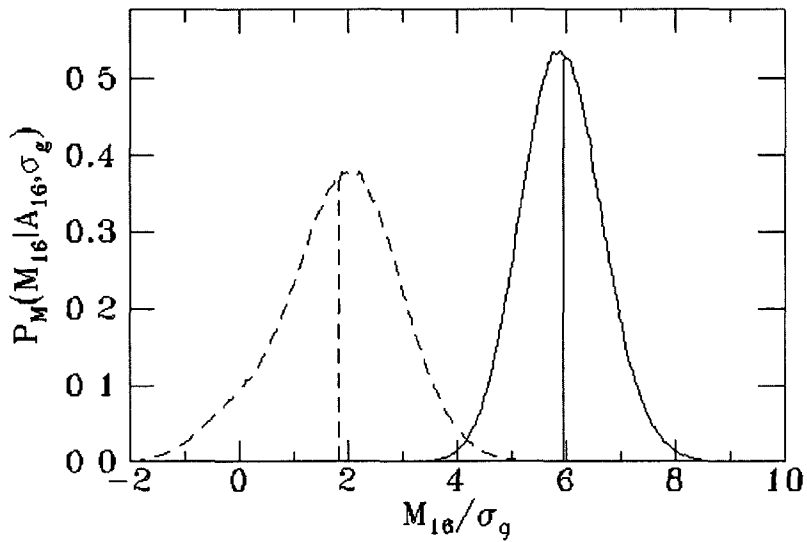


Figure E.5 Simulated PDFs Before and After the RNBC Calculated

Using $\langle M_N \rangle_{x^9}$ and σ_g for $N=16$



References

- [1] Mansfield P and Grannell P K NMR 'diffraction' in solids? J Phys C Solid State Phys 1973,6 L442
- [2] Lauterbur P Image formation by induced local interactions Examples employing NMR Nature 1973, 242 190–191
- [3] Kumar A, Welti D, Ernst R NMR Fourier zeugmatography J Magn Reson 1975, 18 69–83
- [4] E O Stejskal and J E Tanner, Spin diffusion measurements Spin echoes in the presence of a time-dependent field gradient J Chem Phys , 42(1) 288-292,1965
- [5] Le Bihan D, Breton E, Syrota A Imagerie de diffusion par resonance magnetique nucleaire C R Acad Sci [III] 1985, 301 1109-1112
- [6] A Einstein, Investigations on the Theory of the Brownian Movement, Courier Dover Publications, (1956)
- [7] Le Bihan D, Intravoxel Incoherent Motion Perfusion MR Imaging A Wake-Up Call, Radiology 2008, 249 748-752
- [8] Le Bihan D, Moonen CT, Van Zijl PC, Pekar J, Des Pres D Measuring random microscopic motion of water in tissues with MR imaging a cat brain study J Comput Assist Tomogr 1991,15 19–25
- [9] Luciani A et al Liver cirrhosis intravoxel incoherent motion MR imaging— pilot study Radiology 2008,249(3) 891–899

- [10] Namimoto T, Yamashita Y, Sumi S, Tang Y, Takahashi M Focal liver masses characterization with diffusion-weighted echo-planar MR imaging *Radiology* 1997,204 739–744
- [11] Ichikawa T, Haradome H, Hachiya J, Nitatori T, Araki T Diffusion weighted MR imaging with a single-shot echoplanar sequence detection and characterization of focal hepatic lesions *Am J Roentgenol* 1998,170 397–402
- [12] Yamada I, Aung W, Himeno Y, Nakagawa T, Shibuya H Diffusion coefficients in abdominal organs and hepatic lesions evaluation with intravoxel incoherent motion echo-planar MR imaging *Radiology* 1999,210 617–623
- [13] Kim T, Murakami T, Takahashi S, Hori M, Tsuda K, Nakamura H Diffusion-weighted single-shot echoplanar MR imaging for liver disease *Am J Roentgenol* 1999,173 393–398
- [14] Taouli B, Vilgrain V, Dumont E, Daire JL, Fan B, Menu Y Evaluation of liver diffusion isotropy and characterization of focal hepatic lesions with two single-shot echoplanar MR imaging sequences prospective study in 66 patients *Radiology* 2003,226 71–78
- [15] Hussain SM, De Becker J, Hop WC, Dwarkasing S, Wielopolski PA Can a single-shot black-blood T2-weighted spin-echo echo-planar imaging sequence with sensitivity encoding replace the respiratory triggered turbo spin-echo sequence for the liver? An optimization and feasibility study *J Magn Reson Imaging* 2005,21 219–229
- [16] Coenegrachts K et al Improved focal liver lesion detection comparison of single-shot diffusion-weighted echoplanar and single-shot T2 weighted turbo spin echo techniques *Br J Radiol* 2007,80 524–531

- [17] Bruegel M, Gaa J, Waldt S, et al Diagnosis of hepatic metastasis comparison of respiration-triggered diffusion-weighted echo-planar MRI and five t2-weighted turbo spin-echo sequences Am J Roentgenol 2008,191 1421–1429
- [18] Bruegel M, Holzapfel K, Gaa J, et al Characterization of focal liver lesions by ADC measurements using a respiratory triggered diffusion-weighted single-shot echo-planar MR imaging technique Eur Radiol 2008,18 477–485
- [19] Parikh T et al Focal liver lesion detection and characterization with diffusion-weighted MR imaging comparison with standard breath-hold T2 weighted imaging Radiology 2008,246 812–822
- [20] Muller MF, Prasad P, Siewert B, Nissenbaum MA, Raptopoulos V, Edelman RR Abdominal diffusion mapping with use of a wholebody echo-planar system Radiology 1994,190 475–478
- [21] Moteki T, Ishizaka H, Horikoshi H, Matsumoto M Differentiation between hemangiomas and hepatocellular carcinomas with the apparent diffusion coefficient calculated from turboFLASH MR images J Magn Reson Imaging 1995,5 187–191
- [22] Okada Y, Ohtomo K, Kiryu S, Sasaki Y Breath-hold T2-weighted MRI of hepatic tumors value of echo planar imaging with diffusion sensitizing gradient J Comput Assist Tomogr 1998,22 364–371
- [23] Ichikawa T, Haradome H, Hachiya J, Nitatori T, Araki T Diffusion weighted MR imaging with single-shot echo-planar imaging in the upper abdomen preliminary clinical experience in 61 patients Abdom Imaging 1999,24 456–461
- [24] Ichikawa T, Araki T Fast magnetic resonance imaging of liver Eur J Radiol 1999,29 186–210

- [25] Moteki T, Sekine T Echo planar MR imaging of the liver comparison of images with and without motion probing gradients *J Magn Reson Imaging* 2004,19 82–90
- [26] Koinuma M, Ohashi I, Hanafusa K, Shibuya H Apparent diffusion coefficient measurements with diffusion-weighted magnetic resonance imaging for evaluation of hepatic fibrosis *J Magn Reson Imaging* 2005,22 80–85
- [27] Nasu K et al Hepatic metastases diffusion weighted sensitivity-encoding versus SPIO-enhanced MR imaging *Radiology* 2006,239 122–130
- [28] Koh DM et al Detection of colorectal hepatic metastases using MnDPDP MR imaging and diffusion-weighted imaging (DWI) alone and in combination *Eur Radiol* 2008,18 903–910
- [29] Girometti R, Furlan A, Bazzocchi M, et al Diffusion-weighted MRI in evaluating liver fibrosis a feasibility study in cirrhotic patients *Radiol Med (Torino)* 2007,112 394–408
- [30] Taouli B et al Diffusion-weighted MRI for quantification of liver fibrosis preliminary experience *Am J Roentgenol* 2007,189 799–806
- [31] Taouli B, Chouli M, Martin AJ, Qayyum A, Coakley FV, Vilgrain V Chronic hepatitis role of diffusion-weighted imaging and diffusion tensor imaging for the diagnosis of liver fibrosis and inflammation *J Magn Reson Imaging* 2008,28 89–95
- [32] Koinuma M, Ohashi I, Hanafusa K, Shibuya H Apparent diffusion coefficient measurements with diffusion-weighted magnetic resonance imaging for evaluation of hepatic fibrosis *J Magn Reson Imaging* 2005,22 80–85
- [33] Lewin M et al Diffusion-weighted magnetic resonance imaging for the assessment of fibrosis in chronic hepatitis C *Hepatology* 2007,46 658–665

- [34] Kamel IR et al Role of diffusion-weighted imaging in estimating tumor necrosis after chemoembolization of hepatocellular carcinoma Am J Roentgenol 2003,181 708–710
- [35] Kamel IR et al The role of functional MR imaging in the assessment of tumor response after chemoembolization in patients with hepatocellular carcinoma J Vasc Interv Radiol 2006,17 505–512
- [36] Koh DM et al Predicting response of colorectal hepatic metastasis value of pretreatment apparent diffusion coefficients Am J Roentgenol 2007,188 1001–1008
- [37] Cui Y, Zhang XP, Sun YS, Tang L, Shen L Apparent diffusion coefficient potential imaging biomarker for prediction and early detection of response to chemotherapy in hepatic metastases Radiology 2008,248 894–900
- [38] Kamel IR, Reyes DK, Liapi E, Bluemke DA, Geschwind JF Functional MR imaging assessment of tumor response after ⁹⁰Y microsphere treatment in patients with unresectable hepatocellular carcinoma J Vasc Interv Radiol 2007,18 49–56
- [39] Chen CY et al Early response of hepatocellular carcinoma to transcatheter arterial chemoembolization choline levels and MR diffusion constants—initial experience Radiology 2006,239 448–456
- [40] Liapi E et al Functional MRI evaluation of tumor response in patients with neuroendocrine hepatic metastasis treated with transcatheter arterial chemoembolization Am J Roentgenol 2008,190 67–73
- [41] Kamel IR, Liapi E, Reyes DK, Zahurak M, Bluemke DA, Geschwind JF Unresectable hepatocellular carcinoma serial early vascular and cellular changes after

transarterial chemoembolization as detected with MR imaging *Radiology* 2009,250 466 - 473

[42] Koh DM et al Colorectal hepatic metastases quantitative measurements using single-shot echo-planar diffusion-weighted MR imaging *Eur Radiol* 2006, 16 1898–1905

[43] Koh DM, Collins DJ Diffusion-Weighted MRI in the Body Applications and Challenges in Oncology, *Am J Roentgenol* 2007, 188 1622-1635

[44] Bammer R, Keeling SL, Augustin M, et al Improved diffusion weighted single-shot echo-planar imaging (EPI) in stroke using sensitivity encoding (SENSE) *Magn Reson Med* 2001,46 548–554

[45] Taouli B, Martin AJ, Qayyum A, et al Parallel imaging and diffusion tensor imaging for diffusion-weighted MRI of the liver preliminary experience in healthy volunteers *AJR Am J Roentgenol* 2004,183 677–680

[46] Murtz P, Flacke S, Traber F, van den Brink JS, Gieseke J, Schild HH Abdomen diffusion-weighted MR imaging with pulse-triggered single-shot sequences *Radiology* 2002,224 258–264

[47] Nasu K, Kuroki Y, Sekiguchi R, Nawano S The effect of simultaneous use of respiratory triggering in diffusion-weighted imaging of the liver *Magn Reson Med Sci* 2006,5 129–136

[48] Gourtsoyianni S, Papanikolaou N, Yarmenitis S, Maris T, Karantanas A, Gourtsoyiannis N Respiratory gated diffusion-weighted imaging of the liver value of apparent diffusion coefficient measurements in the differentiation between most

commonly encountered benign and malignant focal liver lesions *Eur Radiol* 2008,18 486–492

[49] Kwee TC, Takahara T, Koh DM, Nieuvelstein RA, Lujten PR Comparison and reproducibility of ADC measurements in breath hold, respiratory triggered, and free-breathing diffusion-weighted MR imaging of the liver *J Magn Reson Imaging* 2008,28 1141–1148

[50] Asbach P et al Magnetic resonance cholangiopancreatography using a free-breathing T2-weighted turbo spin-echo sequence with navigator-triggered prospective acquisition correction *Magn Reson Imaging* 2005,23 939–945

[51] Wang Y, Rossman PJ, Grimm RC, Riederer SJ, Ehman RL Navigator-echo-based real-time respiratory gating and triggering for reduction of respiration effects in three-dimensional coronary MR angiography *Radiology* 1996,198 55–60

[52] Spritzer CE, Keogan MT, DeLong DM, Dahlke J, MacFall JR Optimizing fast spin echo acquisitions for hepatic imaging in normal subjects *J Magn Reson Imaging* 1996,6 128–135

[53] Low RN, Alzate GD, Shimakawa A Motion suppression in MR imaging of the liver comparison of respiratory-triggered and nontriggered fast spin-echo sequences *Am J Roentgenol* 1997,168 225–231

[54] Klessen C, et al Magnetic resonance imaging of the upper abdomen using a free-breathing T2-weighted turbo spin echo sequence with navigator triggered prospective acquisition correction *J Magn Reson Imaging* 2005,21 576–582

[55] Choi JY, Lee JM, Lee JY, et al Navigator-triggered isotropic three dimensional magnetic resonance cholangiopancreatography in the diagnosis of malignant biliary

obstructions comparison with direct cholangiography J Magn Reson Imaging 2008,27 94–101

[56] Moore RJ, Issa B, Tokarczuk P, et al In vivo intravoxel incoherent motion measurements in the human placenta using echo-planar imaging at 0.5 T Magn Reson Med 2000,43 295–302

[57] Moore RJ, Strachan BK, Tyler DJ, et al In utero perfusing fraction maps in normal and growth restricted pregnancy measured using IVIM echo-planar MRI Placenta 2000,21 726–732

[58] A M Al-Radaideh et al, Proc Intl Soc Mag Reson Med 2009, p 17

[59] Henkelman RM Does IVIM measure classical perfusion? Magn Reson Med 1990,16 470–475

[60] S Truica, G Cron, I Cameron, Improved Diffusion Weighted MR Imaging of Liver in Normal Subjects, Med Phys 36, 4322 (2009), doi 10.1118/1.3244191

[61] Truica L S , Cameron I , Gruslin A , Avruch L , Assessment of Placental Blood Flow Using a Navigator Echo Respiratory Gated Parallel Imaging Technique at 1.5 T, ISMRM 2010, p 4564

[62] Slichter C P , *Principles of Magnetic Resonance* (Springer-Verlag, New York 1990)

[63] Cowan B , *Nuclear Magnetic Resonance and Relaxation* (Cambridge University Press, Cambridge 1997)

[64] Callaghan P T , *Principles of Nuclear Magnetic Resonance Microscopy* (Clarendon Press, Oxford 1991)

[65] Carr H Y and Purcell E M , The effect of diffusion on free precession in nuclear magnetic resonance, Phys Rev 1954, 94 630-8

- [66] Meiboom S and Gill D , Modified spin-echo method for measuring nuclear relaxation times, Rev Sci Instr 1958, 29 688-91
- [67] Crank J , *The mathematics of diffusion* Oxford, England Oxford University Press, 1975
- [68] Jost W , *Diffusion in solids, liquids and gases* New York Academic Press, 1960
- [69] Pathria R K , *Statistical Mechanics* Pergamon Press, 1972
- [70] Hahn E L Spin echoes, Phys Rev, 1950, 80(4) 580-594
- [71] Carr H Y and Purcell E M , Effects of diffusion on free precession in Nuclear Magnetic Resonance Experiments Phys Rev, 1954, 94(3) 630
- [72] Tanner J E ,The use of stimulated echo in NMR diffusion studies J Chem Phys , 1965,190,52 2523-2526
- [73] Torrey H C , Bloch equations with diffusion terms Phys Rev ,1956, 104 563
- [74] D Le Bihan, E Breton, D Lallemand, P Grenier, E Cabanis, and M Laval-Jeantet MR imaging of intravoxel incoherent motions application to diffusion and perfusion in neurologic disorders Radiology, 1986, 161(2) 401-7
- [75] Y Cohen and Y Assaf, High b-value q-space analyzed diffusion-weighted MRS and MRI in neuronal tissues - a technical review, NMR Biomed, 2002, 15(7-8) 516-542
- [76] Le Bihan D, Breton E, Lallemand D, Aubin ML, Vignaud J, Laval Jeantet M Separation of diffusion and perfusion in intravoxel incoherent motion (IVIM) MR imaging Radiology 1988,168 497-505
- [77] Ehman RL, Felmlee JP, Adaptive technique for high-definition MR imaging of moving structures, Radiology 1989 Oct, 173(1) 255-63

- [78] Thesen S, Heid O, Mueller E, Schad LR, Prospective acquisition correction for head motion with image-based tracking for real-time fMRI, *Magn Reson Med* 2000, 44(3) 457-65
- [79] Gray H, *Anatomy of the Human Body*, 15th Edition, Chancellor Press, Finland, 1994
- [80] Mills R, Self-Diffusion in Normal and Heavy Water in the Range 1-45 J *Phys Chem*, 1973,77 685-688
- [81] Press W H, Teukolsky S A, Vetterling W T, Flannery B P, *Numerical Recipes*, Second Edition, Cambridge University Press, 1992
- [82] Reese T G, Heid O, Weissko R M, Wedeen V J, Reduction of eddy current induced distortion in diffusion MRI using a twice-refocused spin echo *Magn Reson Med*, 2003, 49(1) 177-182
- [83] Mayhew et al, Placental Morphogenesis and the star volumes of villous trees and intervillous pores, *Placenta* 1994, 15 209-217
- [84] Bergmann A, Zygmunt M, Clapp JF, Running throughout pregnancy effect on placental villous vascular volume and cell proliferation, *Placenta*, September 2004, 25 8, 694-698
- [85] Le Bihan D editor, *Diffusion and Perfusion Magnetic Resonance Imaging – Applications to Functional MRI*, Raven Press, New York, 1995
- [86] C G Koay, P J Basser, *J Magn Reson* 179 (2006), 317-322
- [87] A Cardenas-Blanco et al, Accurate noise bias correction applied to individual pixels, p 3445, *ISMRM Berlin* (2007), 952-962
- [88] P Tofts, *Quantitative MRI of the Brain*, Wiley (2003)

- [89] D K Jones, P J Basser, "Squashing peanuts and smashing pumpkins" how noise distorts diffusion-weighted MR data *Magn Reson Med* 52 (2004), 979-993
- [90] A Cárdenas-Blanco, C Tejos, P Irarrazaval, I G Cameron, Noise in Magnitude Magnetic Resonance Images, *Concepts in Magn Reson* (2008), 32A(6), 409-416
- [91] C D Constantinides et al, Signal to Noise Measurements in Magnitude Images from NMR Phased Arrays *Magn Reson Med* 38 (1997), 851-857
- [92] P B Roemer et al, *Magn Reson Med* 16 (1990), 192-225
- [93] M H Ross, *Histology A Text and Atlas With Correlated Cell and Molecular Biology*, Lippincott Williams & Wilkins, published 2010-10-15
- [94] D W Fawcett, *A textbook of Histology*, 12th Edition, Chapman & Hall Press, New York, 1994
- [95] J Patel, E Sigmund, H Rusinek, M Oei, J S Babb and B Taouli, Diagnosis of cirrhosis with intravoxel incoherent motion diffusion MRI and dynamic contrast-enhanced MRI alone and in combination Preliminary experience, *J Magn Reson Imaging* 31(3) 589-600 (2010)
- [96] S D Flamm, Redistribution of Regional and Organ Blood Volume and Effect on Cardiac Function in Relation to Upright Exercise Intensity in Healthy Human Subjects, *Circulation* 1990,81,1550-1559
- [97] Lutt WW, Greenway CV, Conceptual review of the hepatic vascular bed, *Hepatology* 1987,7 952-963
- [98] M A Bernstein, K F King, X J Zhou, *Handbook of MRI Pulse Sequences*, Elsevier Academic Press, USA, 2004